Predicting Transitions in Fischer-Tropsch Reactors

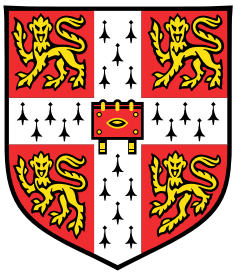

Kevin Kelsey Brian Duff

Supervisors: Dr. N. D. M. Hine
Prof. M. C. Payne

Advisors: Dr. L. Spanu
Dr. R. Agrawal
Dr. P. M. Shenai

Cavendish Laboratory
University of Cambridge

This dissertation is submitted for the degree of
Doctor of Philosophy

Robinson College

May 2019

Declaration

This thesis is the result of my own work and includes nothing which is the outcome of work done in collaboration except as declared in the Preface and specified in the text. It is not substantially the same as any that I have submitted, or, is being concurrently submitted for a degree or diploma or other qualification at the University of Cambridge or any other University or similar institution except as declared in the Preface and specified in the text. I further state that no substantial part of my thesis has already been submitted, or, is being concurrently submitted for any such degree, diploma or other qualification at the University of Cambridge or any other University or similar institution except as declared in the Preface and specified in the text. It does not exceed the prescribed word limit for the relevant Degree Committee. This dissertation contains fewer than 60,000 words.

The contents of Chapter 5 as well as Appendices A and B have also been published in *J. Phys. Chem. C*, vol. 121, pp. 15880–15887, 7 2017.

Kevin Kelsey Brian Duff
May 2019

Abstract

Predicting Transitions in Fischer-Tropsch Reactors

Kevin Kelsey Brian Duff

The Fischer-Tropsch process has the potential to be fundamental to a future without dependence on fossil fuels. It converts syngas, a readily available resource, into high quality hydrocarbons, with water being the primary byproduct. Like many gas-to-liquid processes, it is catalysed on a transition metal surface, and the lifetime of the catalyst bed largely dictates the process's economic viability. Predictive computational models can shed light on the mechanisms driving catalyst deactivation.

This work focuses particularly on reactors with a titania-supported cobalt catalyst. One part of this project is an investigation using VASP studying the adsorption and mobility of several cobalt species that might form on the TiO_2 support surface. It is found that reactor species generally have a strong effect on the binding properties of cobalt, and that this effect could either strengthen or weaken its bond to the surface depending on how reactive the functional group is with the support surface. In particular, the carbon monoxide feedstock was found to favourably bind to surface-adsorbed cobalt and create highly mobile species. In practice the support surface is rarely dry, and this effect is also found on a model hydrated surface. This painted a clear picture that the carbon monoxide feed may have an effect on the sintering process by inducing surface and gas-phase transport of highly dispersed cobalt.

Plane-wave DFT suffers from unfavourable cubic scaling and its extended basis makes vacuum space costly, limiting its applicability to large clusters and surface structures. The linear-scaling DFT code ONETEP is a good candidate for investigating these classes of system. While its metals treatment for systems smaller than the thousands of atoms scale using ensemble DFT (EDFT) is also cubic-scaling, it is able to offload a lot of the cost of the calculation onto linear-scaling parts and also maintains a linear-scaling memory cost. Another part of this project was to develop ONETEP to be able to perform studies of chemistry on adsorbed and free catalyst nanoparticles. Two

main pieces of crucial functionality have been added to ONETEP - free-spin EDFT and nudged elastic band transition-state searching. The former allows ensemble DFT to be performed at non-integer net spin and non-integer charge, and also adds the ability to relax the spin state during a calculation - previously ONETEP was constrained to fixed integer net spin. This is crucial in cases where the net spin of a magnetic system is not necessarily known or may be altered by, for example, surface adsorbates. The latter is a popular and robust transition state searching method that reliably minimizes a path connecting a product and reactant. The dimer method is also being developed for ONETEP primarily as a transition state refinement tool.

Early applications of the new functionality in ONETEP is demonstrated in an investigation of carbon monoxide binding on cobalt HCP and FCC nanoparticles of around 50 atoms. These adsorption energies are compared, where available, to surface adsorption energies from literature. Generally, the abundance of edges on these small particles make surface adsorption energies site dependent and different to clean surface values, and adsorption sites near edges are generally stronger than the surface values. Additionally, two CO dissociation pathways on the FCC cluster are examined, starting from the surface making up the majority on the FCC Wulff particle. A modest decrease in activation energy is identified, and the presence of new pathways involving particle edges is highlighted for future study.

Dr. Alan Grant: I hate computers.
Dr. Ellie Sattler: The feeling's mutual.

- Jurassic Park (1993)

I dedicate this thesis to my mom, Sandy. I love you, universes, forever.

Acknowledgements

I would like to primarily acknowledge my supervisor Nicholas Hine for incredible support and guidance throughout both this Ph. D. and the preceding Master's degree.

I would also like to acknowledge the following people and groups: Mike Payne for resources, funding, and guidance; the computational chemistry group at Shell Technology Center Bangalore for providing funding, guidance, and context for my research; my colleagues on the CDTCMMS for support and camaraderie; Edward Linscott for the use of a figure; and my family and friends.

Funding

This work was carried out with funding and advisor support from Shell Technology Center Bangalore. Funding was provided through the EPSRC CDT in Computational Methods for Materials Science.

This work was performed in part using resources provided by the Cambridge Service for Data Driven Discovery (CSD3) operated by the University of Cambridge Research Computing Service (www.csd3.cam.ac.uk), provided by Dell EMC and Intel using Tier-2 funding from the Engineering and Physical Sciences Research Council (capital grant EP/P020259/1), and DiRAC funding from the Science and Technology Facilities Council (www.dirac.ac.uk).

I am grateful to the UK Materials and Molecular Modelling Hub for computational resources, which is partially funded by EPSRC (EP/P020194/1).

Table of contents

List of figures

List of tables

Chapter 1

Introduction

Many of the greatest challenges of this century fall under the umbrella of sustainable energy, with oil reserves diminishing while both the human population and its impact on the environment grow. One of these challenges is the identification and development of methods accepting renewable feeds for the production of fuels and hydrocarbon-based chemicals; demand on energy in the short-term must be met with lower dependence on fossil fuel, while in the long-term hydrocarbons may continue to offer an efficient solution to energy storage. Part of the solution may lie in the renewable generation of feed for the Fischer-Tropsch process [1], which converts gas-phase carbon monoxide and hydrogen into clean, high-purity liquid hydrocarbon fuels and waxes. Work is being done on the generation of the feed by gasification of biomass [2, 3], or even extraction from the atmosphere [4]. Current limitations include low yields and high contaminant levels.

The activities of the reactions making up the Fischer-Tropsch reactor are dependent on many complex factors including the structure of the catalyst, interactions with the support, and emergence of new materials and nanostructures in the reactor over the course of the catalyst bed's lifetime. The viability of the Fischer-Tropsch process is also limited by the deactivation of the catalyst over time. This motivates studies of the causes of catalyst activity and deactivation in these reactors, though these effects are very difficult to probe experimentally. Advances in computational modelling in the past few decades have made simulations of reactor environments with quantum mechanical accuracy feasible.

1.1 Fischer-Tropsch Synthesis

The Fischer-Tropsch process is a gas-to-liquid (GTL) conversion process that produces high-quality hydrocarbon waxes and diesels from syngas (carbon monoxide and hydrogen). This process evolved over the first half of the 20th century, with initial synthesis of methane from syngas being performed by 1902 by Sabatier and Senderens [5]. The process saw mixed industrial interest until strategic and environmental concerns drove a renewed research interest in the 1980's. Today, this process accounts for approximately 2% of the world's fuel production [6]. The primary reactions are the hydrogenation of CO and the growth and termination of the hydrocarbon chain, described in Equations 1.1-1.3 [7]. Equations 1.4 and 1.5 are examples of unfavourable side-reactions that occur in the reactor. Reactor conditions are tuned to maximize the length of chain produced, which can be used directly or hydrocracked into smaller products.

$$\text{Fischer} - \text{Tropsch Reactions :}$$

$$\mathrm{CO} + 2\,\mathrm{H_2} \longrightarrow \mathrm{CH_2} + \mathrm{H_2O} \tag{1.1}$$

$$(\mathrm{CH_2})_n + \mathrm{CO} + 2\,\mathrm{H_2} \longrightarrow (\mathrm{CH_2})_{n+1} + \mathrm{H_2O} \tag{1.2}$$

$$(\mathrm{CH_2})_n + \mathrm{H_2} \longrightarrow \mathrm{C}_n\mathrm{H}_{2n+2} \tag{1.3}$$

$$\text{Some Side Reactions :}$$

$$\mathrm{CO} + \mathrm{H_2O} \longrightarrow \mathrm{CO_2} + \mathrm{H_2} \tag{1.4}$$

$$2\,\mathrm{CO} \longrightarrow \mathrm{C} + \mathrm{CO_2} \tag{1.5}$$

The Fischer-Tropsch process makes up part of industrial liquefaction [8]. It is preceded by the generation of syngas from some carbon source such as coal, natural gas, biomass, organic waste, or the atmosphere. While the last two are particularly exciting and have drawn significant research effort, the production and treatment of tar and particulate contaminants pose a challenge to the design of their gassification processes [8, 3]. Specific reactor designs have been proposed to address these issues. The product of a Fischer-Tropsch reactor is 'syncrude', a mixture of hydrocarbon types as well as other by-products and water, which is then refined into traditional crude oil products. These steps together provide a potentially non-fossil route to generating fuels and petrochemicals that consumers and other industries depend on.

The Anderson–Schulz–Flory model [9] is a simple description of the distribution of weights of products in Fischer-Tropsch reactors. It is based on the assumption that all surface chains are equally reactive regardless of their length, and is also used to

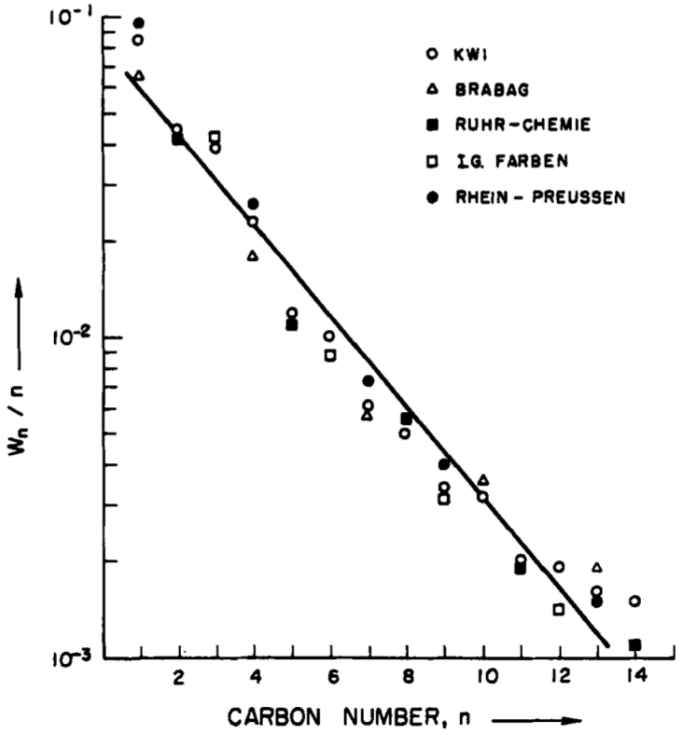

Fig. 1.1 Fit of industrial FT reactor data to the Anderson–Schulz–Flory model. In this fit both the (negative) slope and intercept provide the value of p_G. Image source: [9], reproduced with permission from Taylor & Francis.

describe chain growth in polymerization reactions. It is given in Equation 1.6 where W_n is the fraction of product containing n carbon atoms, with chain growth probability p_G depending on several factors including catalyst and support selection, reactor design, and reaction conditions [7].

$$\frac{W_n}{n} = (1 - p_G)^2 p_G^{n-1} \tag{1.6}$$

Figure 1.1, reproduced from Reference [9], demonstrates that the model holds for a selection of industrial data. Under this model there is a decreasing theoretical maximum selectivity for each product weight, with only methane having a 100% maximum yield. These selectivity limits provide a good model of the economic limitations of the FT process and highlight the importance of maximizing p_G.

1.2 Catalyst Selection

Like many gas-to-liquid reactions, the Fischer-Tropsch process is catalysed on transition metal surfaces. Surfaces of all group VIII elements are active catalysts [1]. Ruthenium

has the most favourable qualities as a catalyst with the highest activity and average product weight [1, 10]. However, its cost and global scarcity make it impractical for large-scale use [1]. The remaining group VIII elements excepting osmium in decreasing order of average product weight are Fe, Co, Rh, Ni, Ir, Pt, and Pd [10]. Of these, nickel, iron, and cobalt are sufficiently active to be considered for industrial use. The activity and product selectivity of osmium have been reported to be poor, with a high selectivity for methane and relatively low activity [11]. Nickel is also known to select for methane under realistic conditions [12], leaving iron and cobalt as catalyst candidates. Referring back to the Anderson–Schulz–Flory model in Equation 1.6, chain growth probabilities of up to about 0.95 and 0.94 have been achieved with iron and cobalt catalysts respectively under ideal conditions [13].

Both iron and cobalt catalysts are suitable for low-temperature FT reactors, which run at about 220 °C-240 °C [13, 14]. Both catalysts are sensitive to sulphur poisoning (described in Section 1.4), though cobalt much more so than iron [15, 13]. Iron catalysts produce more alkene products and are more active in the carbon dioxide producing water-gas shift side reaction compared to cobalt [15]. Both catalysts operate under different pressure ranges and feed ratios; for example iron is more appropriate for feeds with low H_2:CO ratios such as those derived from biomass [15, 1]. At higher feed ratios such as those derived from natural gas cobalt is preferred due to its low activity in the water-gas shift reaction [16]. Overall cobalt can be considered a superior, but more expensive, choice for low-temperature reactors producing high quality long-chain hydrocarbons due to its longer lifetime and favourable alkane selectivity compared to iron [1].

At higher temperatures the selectivity for methane of cobalt catalysts increases dramatically, making them unsuitable for the FT process outside of a relatively narrow band of pressures and temperatures [1]. The high-temperature Fischer-Tropsch mode (573 K-623 K) is therefore run with an iron catalyst [1]. However the low-temperature mode is the focus of most research and development in recent decades [1].

1.3 Support Selection for Cobalt Catalysts

It has been established that the selection of support has an impact on the activity of Fischer-Tropsch catalysts. In the context of cobalt catalysts, supports with a higher surface area generally promote higher dispersion (smaller catalyst particle size) which increases active surface area [16]. Some supports can form irreversible surface species,

preventing full reduction of the catalyst [16]. A study by Bartholomew and Reuel [17] found that titania (TiO_2) as a support promotes a higher activity for CO hydrogenation on cobalt compared to Al_2O_3, SiO_2, MgO, and C.

Support selection is also known to have an impact on the nature of FT products [16]. Acidic supports such as zeolite or ZSM-5 promote branched products while less acidic supports promote traditional straight-chained alkanes and alkenes [16].

Strong metal-support interactions (often termed SMSI) are known to exist in titania supports [18, 19]. SMSI affects the activity and selectivity of the FT catalyst beyond what can be explained by their surface area effect on particle dispersion. They involve the partial reduction of the support surface and subsequent interactions with the catalyst particle. They are known to relate to the reducibility of the catalyst, possibly in conjunction with dopants [20]. Additionally the partial pressure of water vapour is known to have a strong effect on SMSI [21, 20].

Strong interactions between the TiO_2 support and the catalyst were first postulated for nickel catalysts [22, 23] to describe an increase in both activity and selectivity for non-methane products. Subsequent studies revealed similar results in cobalt [24, 21]. TiO_2 has multiple forms; the anatase form is most commonly used for industrial applications as a catalyst support [25]. Other common polymorphs include rutile and brookite, with the former being the most stable naturally occurring form [26]. Anatase is known to produce stronger SMSI effects than rutile for a range of catalysts [21, 27, 20].

The SMSI observed on anatase-form titania supports as well as its favorable thermal stability under reaction conditions [7] make it a common choice of FT catalyst. The Wulff construction [28] of anatase is a truncated bipyramid depicted in Figure 1.2 with the (111) surface being a strong majority surface and the (001) surface being the minority [26].

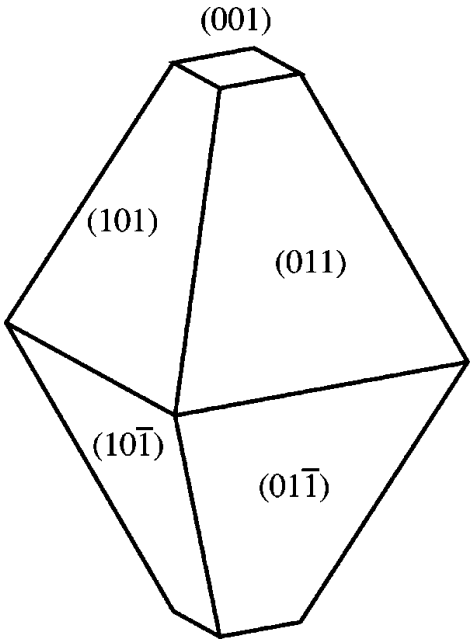

Fig. 1.2 Wulff construction of anatase TiO_2. Image source: [26], reproduced with permission from APS Physics.

1.4 Overview of Deactivation of Cobalt Catalysts

Figure 1.3 shows the activity and methane selectivity of an aluminia-supported cobalt catalyst in a slurry reactor over the course of several days [29]. Deactivation of the Fischer-Tropsch catalyst has been found to occur in two different regimes [29]. There is an initial period of reversible deactivation which typically occurs for a number of days, up to weeks, followed by an ongoing regime of irreversible deactivation. There are a number of proposed mechanisms for deactivation and it is clear that several of them are active at a given time. While this thesis will focus on sintering in particular, a brief introduction to a few others is relevant for context.

1.4.1 Poisoning

Poisoning is the deactivation of the active surface of the catalyst by a species not present in the main reaction. This typically occurs when a poisoning species adsorbs to the catalyst surface, blocking active sites and potentially altering the local geometric and electronic structure [30]. Poisoning can be reversible or irreversible depending on the adsorption strength of the poisoning species. In the case of cobalt as a Fischer-Tropsch catalyst, the primary poison is sulphur, which is often present in the reactor feed

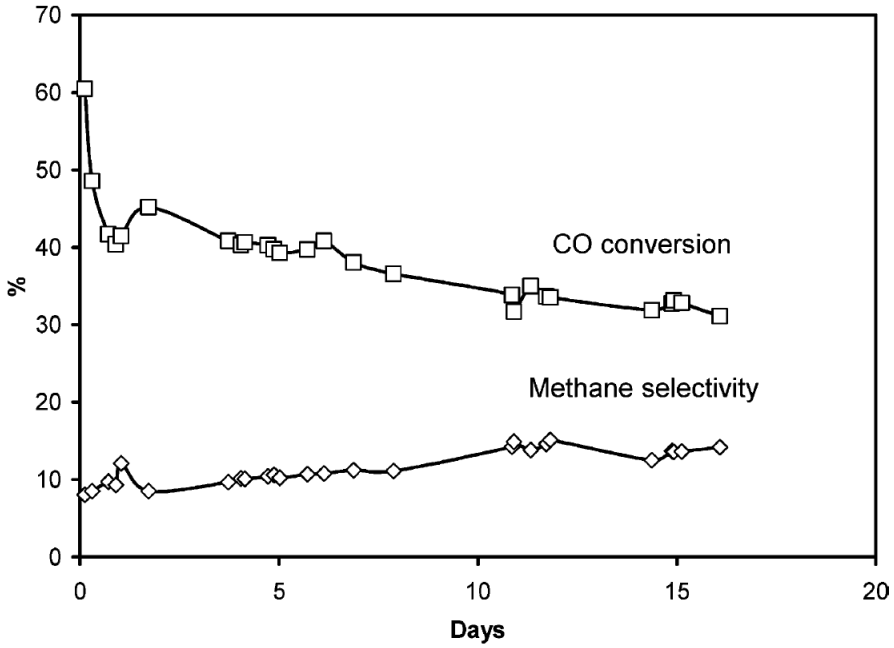

Fig. 1.3 Activity and methane selectivity of a cobalt-catalyzed Fischer-Tropsch reaction. Image source: [1], reproduced with permission from ACS Publications.

or otherwise can appear in the reactor in trace amounts. Sulphur binds strongly to the catalyst surface and the deactivation mechanism appears to be primarily through blocking sites. Studies have linked sulphur poisoning to lower activity and to higher selectivity for lighter hydrocarbon products and CO_2 production [31, 32]. Nitrogen has also been found to be a cobalt catalyst poison even in small amounts, though this appears to be completely reversible [30].

1.4.2 Carbon effects

A number of carbon species can be formed on the surface of the catalyst in addition to the hydrocarbon product. Coke formation on the surface is largely considered a reaction intermediate rather than a fouling species [33], though it has been found through DFT studies [34, 35] that adsorbed carbon on the fcc-Co(111) surface is highly mobile and able to form various alternate carbon structures including graphene. There is also a potential for bulk carbide formation, which has been suggested to have a direct link to deactivation [36]. This link appeared to be support-dependent, with carbides being found on TiO_2 and Al_2O_3 supported Co but not SiO_2 supported Co.

1.4.3 Oxidation

Water is formed in the gas phase as a result of the Fischer-Tropsch process. If it exists at a high enough partial pressure relative to the hydrogen gas feed partial pressure it could stabilize oxide formation in the cobalt nanoparticles. Bulk cobalt is known to be resistant to oxidation under the temperatures and partial pressure ratios encountered in the reactor [37]. However, thermodynamic arguments have shown that Co(II)O may become stable in nanoparticles smaller than 4.4 nm in plausible reactor environments of 220 °C and partial pressure ratio $p_{H_2O}/p_{H_2} < 1.5$. Experimental studies involving steam co-feeds and pure water/hydrogen feeds have demonstrated some surface re-oxidization and subsequent deactivation due to loss of active sites in Fischer-Tropsch environments [38–40]. Oxidation is largely reversible through hydrogen reduction [30].

1.4.4 Sintering

Sintering is a thermodynamically driven process that changes the shape of a catalyst particle to have fewer active surface sites. This is based on lower surface area to volume ratio shapes being energetically favourable. It can be divided into two main processes: coalescence and ripening [41]. Coalescence is the surface diffusion of the nanoparticles across the surface and their eventual collision and partial combination. Ripening is the surface diffusion and random recombination of small groups of atoms that break off from the catalyst particles. Sintering has been explicitly shown to play a role in catalyst deactivation in other reactions, for example in sapphire-supported silver nanoparticles that act as catalysts for the synthesis of ethylene oxide [41, 42]. A recent review [43] describes sintering in cobalt-catalyzed Fischer-Tropsch as a process that is important in the first few weeks of the catalyst bed lifetime and favoured by particles in the 6-12 nm range and high CO conversion rates.

Figure 1.4 shows the ripening of Co partciles on a planar model silica/silicon support surface before and after 10 hours of exposure to Fischer-Tropsch conditions [44]. Small catalyst particles reduce in size or disappear. Figure 1.5 shows the progression of coalescence of Re-promoted Co catalyst particles on a titania support at zero, 32, and 48 days in high-conversion Fischer-Tropsch conditions [45]. This shows two nearby particles being combined into one over time, and then that one particle becoming rounder in shape further reducing active surface area.

A number of experimental studies have suggested that CO can bind to monotomic catalyst particles and create highly surface-mobile species that are likely to contribute

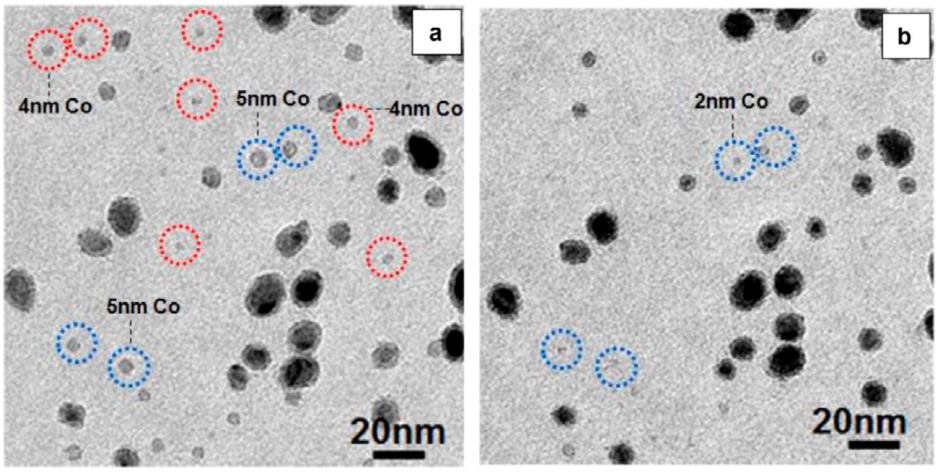

Fig. 1.4 TEM images of cobalt particles on a model silica/silicon support before and after 10 hours of exposure to Fischer-Tropsch conditions. Due to ripening, catalyst particles are reduced in size (blue circles) or disappear (red circles). Image source: [44], reproduced with permission from Elsevier.

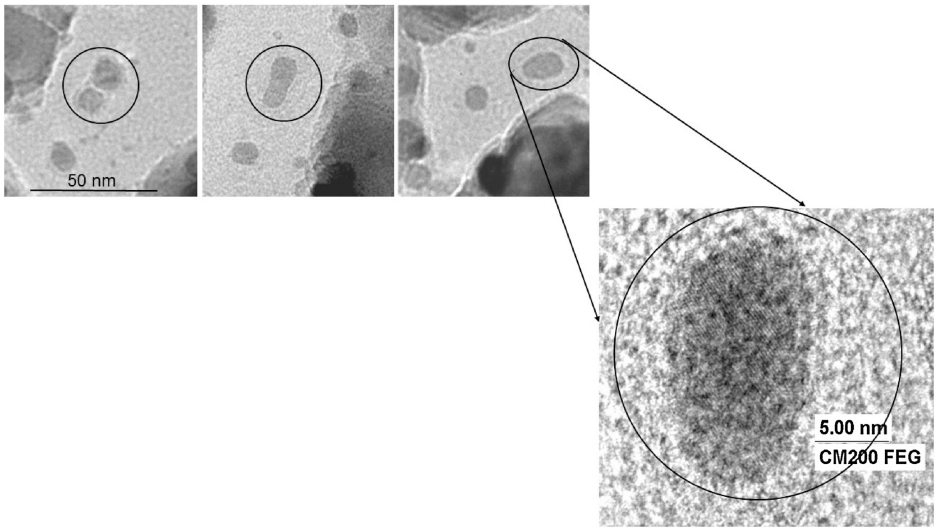

Fig. 1.5 TEM images of rhenium-promoted cobalt particles on a titania support before exposure to Fischer-Tropsch conditions (left), after after 32 days(center) and 48 days (right) of exposure to Fischer-Tropsch conditions. Over this time period two catalyst particles are observed to coalesce into one particle, which then forms into a rounder structure. A higher magnification of the latest image shows the crystal lattice features of the combined particle, indicating a single crystal. Image source: [45], reproduced with permission from Elsevier.

to ripening. Evidence has been found for the formation of carbonyls of Co on SiO_2 [44], Co on Al_2O_3 [46], Co on a clean Co surface [47], and Ni on Al_2O_3 [48]. This motivates a computational study to confirm these suggestions and extend them to the majority anatase surface, and to explore the effects of other species that may form from monotomic catalyst particles.

The Fischer-Tropsch process is highly exothermic so the potential for sintering is high. Experimentally it is found that water vapour accelerates the process [30]. Though sintering is largely an irreversible process, under some conditions it is possible to regain dispersion by a reduction-oxidation-reduction treatment of cobalt particles [49]. The re-dispersed catalyst may have a shortened lifetime [30].

1.5 Computational Studies related to FT GTL

Because of the improvements in computing hardware and in predictive modelling techniques, computational work has been done exploring the workings of GTL reactors including those running Fischer-Tropsch processes computationally. Using first-principles techniques like density functional theory it is possible to study individual processes within the reactor reliably without having to run expensive or infeasible experiments, including processes that contribute to catalyst deactivation or otherwise impact reaction activity. Ideally the mechanisms investigated computationally can then be used to give context to experimental results and help inform better reactor design and control.

1.5.1 Carbon Monoxide Adsorption and Dissociation on Cobalt

Activation of CO is central to the start of the Fischer-Tropsch process. Computational studies of CO adsorption and dissociation on cobalt can give insight into how catalyst structure can affect the process.

Liu *et al.* [50] performed a study of the adsorption and dissociation barriers of CO on several cobalt FCC and HCP surfaces. With reference to the Wulff construction [28] of cobalt it was determined that a large HCP crystal is much more active than an FCC crystal, with the majority (111) FCC surface, which makes up around 70% of the Wulff crystal, having a very high relative activation energy. A hydrogen-assisted route was also explored on the three most active surfaces of each crystal. It was determined to be favourable for the FCC surfaces and unfavourable for the HCP surfaces. Additionally,

the effect of step edges and corrugations in surfaces has been studied and found to produce favourable reaction pathways in some cases [51].

Alternative mechanisms for CO activation on pristine cobalt surfaces have also been explored. These studies indicate that CO activation is influenced by local catalyst geometry as well as CO coverage, carbon deposition, and other factors. This includes, for example, the formation of intermediate CHO and CH_2O species [52, 53]. They produced a moderately favourable pathway but the intermediate species was expected to be very unstable and may only form under high pressures [53]. Other potentially favourable reaction pathways involve CO binding to a growing hydrocarbon chain and separating there [54]. The effects of carbon deposition on clean and corrugated cobalt surfaces has also been studied, finding that the surface topology had the dominant effect in that case [55]. Another study examines CO activation mechanisms on carbon-terminated cobalt nanoislands with high CO coverage, influenced by thermodynamics and microscopy results [56]. Direct dissociation at the edges is found to be energetically expensive; instead the proposed mechanism is a multi-step process involving the step-edge adsorbed carbon sites and hydrogen assistance.

1.5.2 The Need for Linear-Scaling DFT

Most DFT studies in FT reactions have been carried out on surfaces or on idealized surface structures. Experimental data can provide realistic catalyst particle structures, but as particle sizes approach the nanometre range it becomes prohibitively expensive to perform studies on them with traditional cubic-scaling DFT. As a result, studies on the reactivity of nanoparticles have been largely limited to the Wulff particle limit, ignoring the surface-edge effects of moderately sized particles. Linear scaling DFT packages such as ONETEP [57, 58] are becoming promising candidates to accurately simulate even metallic systems, which have been historically problematic for linear-scaling approaches, at increasingly large scales. Recent work [59] has involved simulating experimentally imaged multi-nanometre platinum particles with several hundred atoms using novel metals methods implemented in ONETEP.

1.6 Project Aims

Part of this project aims to provide insight into mechanisms that might accelerate the ripening process. In particular, this project focuses on how atomic cobalt adsorbed

to the support interacts with reactor species and conditions, and how this interaction might make the cobalt more mobile. This is in part in response to experimental evidence that highly mobile $Co(CO)_{1-4}$ species may contribute to deactivation via ripening [44, 46, 47]. This study is feasible under traditional DFT, and is carried out with the plane-wave DFT code VASP [60–63]. VASP is appropriate for systems of this size; while it is cubic scaling, the number of atoms in this study were reasonably small (around 100), and VASP uses a real-space projection technique to reduce the cubic-scaling cost of the calculation [64].

While traditional density functional theory is powerful in its ability to predict mechanisms that drive or inhibit the Fischer-Tropsch process, the need for increasingly large models and those with low periodicity motivate the use of better scaling alternatives. There were several barriers that existed to the study of these systems in ONETEP at the start of this project. This included a restriction on metallic simulations that spin channels be held fixed at integer total occupancy, specified in the input file. This was problematic for systems which have, in an ensemble approach, non-integer net spins, and those with a net spin that is unknown to the user. ONETEP lacked the ability to rigorously determine transition states, those that define the energy barrier to a transition occurring, of a chemical reaction or physical transition, presenting LST/QST approximations instead (see Section 2.3). With this in mind, this project also describes work done to add further new functionality to ONETEP that is critical to predicting the properties of chemical reactions on these large catalyst structures, including those with *a priori* unknown metallic states. It also presents applications work of this functionality on small unsupported cobalt particles.

Chapter 2

Theory and Background

2.1 Density Functional Theory

2.1.1 Introduction to Kohn-Sham Density Functional Theory

DFT [65] is based on the idea that any property of a system of particles can be expressed as a functional of the ground state particle density of that system. In electronic structure this is applied to a system of interacting electrons in an external potential, often the electrostatic potential originating from fixed classical ions. The Hamiltonian of this system is given in Equation 2.1, where upper and lower case indices correspond to ions and electrons respectively and q_I is the proton number of ion I. The external potential $V_{\text{ext}}(\mathbf{r})$ is the electron-ion Coulomb interaction given in Equation 2.2. Note that unless otherwise specified atomic units are used; $\hbar = m_e = e = 4\pi\varepsilon_0 = 1$.

$$\hat{H} = -\frac{1}{2}\sum_i \nabla_i^2 + \frac{1}{2}\sum_{i\neq j}\frac{1}{|\mathbf{r_i} - \mathbf{r_j}|} + \sum_i V_{\text{ext}}(\mathrm{r}_i) \tag{2.1}$$

$$V_{\text{ext}}(\mathbf{r}) = -\sum_I \frac{q_I}{|\mathbf{r} - \mathbf{r}_I|} \tag{2.2}$$

Hohenberg-Kohn Theorems

The existence of the DFT functionals is proven by the two Hohenberg-Kohn theorems [66]. The first states that $V_{\text{ext}}(\mathbf{r})$ is uniquely determined up to a constant by the ground state electron density $n_0(\mathbf{r})$. Because the first two terms of Equation 2.1 are the same for all N-electron systems, $n_0(\mathbf{r})$ fully determines $\hat{H}$ and therefore all properties of the system. The second theory proves the existence of a universal

functional of the electron density $E_{\mathrm{HK}}[n(\mathbf{r})]$, the variational minimum of which is found at $n_0(\mathbf{r})$ and gives the correct ground state energy. This functional is often expressed as in Equation 2.3, where $T[n]$ is a kinetic energy term, $E_{\mathrm{e-e}}[n]$ is an electron-electron interaction energy term, $E_{\mathrm{I-I}}$ is the classical ion-ion Coulomb interaction energy, and $E_{\mathrm{ext}}[n] \equiv \int \mathrm{d}^3 r V_{\mathrm{ext}}(\mathrm{r}) n(\mathrm{r})$.

$$E_{\mathrm{HK}}[n] = T[n] + E_{\mathrm{e-e}}[n] + E_{\mathrm{I-I}} + E_{\mathrm{ext}}[n] \tag{2.3}$$

These existence-proofs do not provide any additional information about the form of the functionals in Equation 2.3, and in general no relationship is known between $n_0(\mathbf{r})$ and any set of properties for an interacting N-electron system in a given $V_{\mathrm{ext}}(\mathbf{r})$. "Orbital-free DFT" methods exist that attempt to approximate the form of the unknown terms in the total energy functional (see, for example, Reference [67]). More commonly the Kohn-Sham approach is used, which makes reference to an auxiliary system of non-interacting electrons.

Kohn-Sham Approach

In order to utilize the Hohenberg-Kohn theorems to produce useful results, the Kohn-Sham approach [68] is used. It defines a system of non-interacting electrons with the same electron density as the fully interacting system of interest. This is called the Kohn-Sham system and its total energy functional can be constructed using solvable independent-particle equations. The electron density can be constructed as in equation 2.4, where ψ_i^σ is the i-th spin-σ single-particle wave function of the Kohn-Sham system.

$$n(\mathbf{r}) \equiv \sum_\sigma n^\sigma(\mathbf{r}) = \sum_\sigma \sum_i^{N_\sigma} |\psi_i^\sigma(\mathbf{r})|^2 \tag{2.4}$$

The terms in Equation 2.3 can then be constructed from this density. The single-particle kinetic energy $T_s[n]$ is denoted as a density functional but its form is unknown, and in practice is calculated from the Kohn-Sham states as follows in Equation 2.5.

$$T_{\mathrm{s}} = -\frac{1}{2} \sum_\sigma \sum_i^{N_\sigma} \langle \psi_i^\sigma | \nabla_i^2 | \psi_i^\sigma \rangle \tag{2.5}$$

The electron-electron interaction is divided into a Hartree term $E_{\mathrm{H}}[n]$ that includes self-interaction, defined in Equation 2.6, and an exchange-correlation term $E_{\mathrm{xc}}[n]$ that includes all non-Coulombic electron-electron interactions. It is defined as in Equation

2.7 and its functional form is unknown; it is approximated in practice. The total energy functional $E_{\mathrm{KS}}[n]$ is then given by Equation 2.8.

$$E_{\mathrm{H}}[n] = \int \mathrm{d}^3 r \mathrm{d}^3 r' \frac{n(\mathbf{r})n(\mathbf{r}')}{|\mathbf{r}-\mathbf{r}'|} \tag{2.6}$$

$$E_{\mathrm{xc}}[n] = (E_{\mathrm{e-e}}[n] - E_{\mathrm{H}}[n]) + (T[n] - T_{\mathrm{s}}[n]) \tag{2.7}$$

$$E_{\mathrm{KS}}[n] = T_{\mathrm{s}}[n] + \int \mathrm{d}^3 r V_{\mathrm{ext}}(\mathbf{r})n(\mathbf{r}) + E_{\mathrm{H}}[n] + E_{\mathrm{xc}}[n] + E_{\mathrm{I-I}} \tag{2.8}$$

Variationally minimizing Equation 2.8 with respect to $\psi_i^{*\sigma}$ leads to the Schrödinger-like Kohn-Sham equations for the single-particle Kohn-Sham states, given by Equation 2.9, where $V_{\mathrm{eff}}^{\sigma}$ is the effective potential given by Equation 2.10.

$$\hat{H}_{\mathrm{KS}}^{\sigma}(\mathbf{r})\psi_i^{\sigma}(\mathbf{r}) = \left[-\frac{1}{2}\nabla^2 + V_{\mathrm{eff}}^{\sigma}(\mathbf{r})\right]\psi_i^{\sigma}(\mathbf{r}) = \varepsilon_i^{\sigma}\psi_i^{\sigma}(\mathbf{r}) \tag{2.9}$$

$$V_{\mathrm{eff}}^{\sigma} \equiv V_{\mathrm{ext}}(\mathbf{r}) + \frac{\partial E_{\mathrm{H}}}{\partial n(\mathbf{r},\sigma)} + \frac{\partial E_{\mathrm{xc}}}{\partial n(\mathbf{r},\sigma)} \equiv V_{\mathrm{ext}}(\mathbf{r}) + V_{\mathrm{H}}(\mathbf{r}) + V_{\mathrm{xc}}^{\sigma}(\mathbf{r}) \tag{2.10}$$

The total energy is then $E = \sum_{\sigma,i} \varepsilon_i^{\sigma} + E_{\mathrm{dc}}$, where E_{dc} is a double-counting term defined in Equation 2.11.

$$E_{\mathrm{dc}} = -\frac{1}{2}\int \mathrm{d}^3 r \mathrm{d}^3 r' \frac{n(\mathbf{r})n(\mathbf{r}')}{|\mathbf{r}-\mathbf{r}'|} + E_{\mathrm{xc}} - \int \mathrm{d}^3 r V_{\mathrm{xc}}(\mathbf{r})n(\mathbf{r}) \tag{2.11}$$

In practice the Kohn-Sham equations are self-consistently solved in a process outlined in Equation 2.12, starting with a guess set of orbitals and continuing until $V_{\mathrm{eff}}^{\prime\sigma}(\mathbf{r}) = V_{\mathrm{eff}}^{\sigma}(\mathbf{r})$. In practice the orbitals and operators are expressed in terms of a convenient underlying basis set, such as plane-waves or atomic orbital-like functions.

$$V_{\mathrm{eff}}^{\sigma}(\mathbf{r}) \rightarrow \{\psi_i^{\sigma}(\mathbf{r}), \varepsilon_i^{\sigma}\} \rightarrow n(\mathbf{r}), E \rightarrow V_{\mathrm{eff}}^{\prime\sigma}(\mathbf{r}) \tag{2.12}$$

2.1.2 Plane-Wave Density Functional Theory

It is common to impose periodic boundary conditions (PBCs) on a simulation cell especially in implementations designed for use on solid state systems. Under PBCs the plane-wave basis set [65] employed by VASP [60–63] and many other traditional DFT codes offers systematically tuneable accuracy by simply increasing the basis set size. The formalism here considers a periodic crystal but this method is also commonly used in systems that are not periodic in all directions. In these cases, periodic images

should be separated by a large enough region of vacuum space that they do not interact significantly.

A simulation cell is composed of a supercell of a crystal, repeated n_1, n_2, and n_3 times along each lattice vector $\mathbf{a}_1$, $\mathbf{a}_2$, and $\mathbf{a}_3$ respectively. Each Kohn-Sham state ψ_i^σ is expanded as in Equation 2.13, where $u_i^\sigma(\mathbf{r})$ has the same periodicity as the simulation cell and $\mathbf{k}$ is a vector in the first Brillouin zone called the crystal momentum [69].

$$\psi_{i,\mathbf{k}}^\sigma(\mathbf{r}) = \exp(i\mathbf{k}\cdot\mathbf{r})u_i^\sigma(\mathbf{r}) \tag{2.13}$$

In periodic systems, properties are expressed as integrals over the first Brillouin zone, in practice represented by a sum over sampled k-points. A sufficient k-point sampling is required to accurately reproduce the band structure of the Kohn-Sham system and calculate physical properties. A common selection is a Monkhorst-Pack grid, which is a regular grid in reciprocal space [70]. It is also common to use cell symmetries to reduce the number of k-points that must be explicitly handled. In directions which are not intended to be periodic, only k-points that are 0 in those directions are appropriate, and the special case of $\mathbf{k} = \mathbf{0}$ is termed the Γ-point.

The cell-periodic part of Equation 2.13 is typically expanded in some finite basis set and the Kohn–Sham equations are variationally minimized. In the plane-wave formalism, the periodic function $u_i^\sigma(\mathbf{r})$ is expressed as a truncated Fourier series as in Equation 2.14 with coefficients $c_{i,\mathbf{G}}^\sigma$. Here Ω is the volume of the simulation cell and the vectors $\mathbf{G}$ lie on a regular grid in reciprocal space, each point being defined by a linear combination of reciprocal lattice vectors. The plane-waves $|\mathbf{G}\rangle \equiv \frac{1}{\sqrt{\Omega}}\exp[i\mathbf{G}\cdot\mathbf{r}]$ form an orthonormal basis set. The Kohn-Sham orbitals can then be written as in Equation 2.15.

$$u_i^\sigma(\mathbf{r}) = \frac{1}{\sqrt{\Omega}}\sum_{\mathbf{G}} c_{i,\mathbf{G}}^\sigma \exp i\mathbf{G}\cdot\mathbf{r} \tag{2.14}$$

$$\psi_{i,\mathbf{k}}^\sigma(\mathbf{r}) = \frac{1}{\sqrt{\Omega}}\sum_{\mathbf{G}} c_{i,\mathbf{G}}^\sigma \exp[i(\mathbf{G}+\mathbf{k})\cdot\mathbf{r}] \tag{2.15}$$

One benefit of the plane-wave basis set is that the terms of the Hamiltonian matrix can be evaluated very simply. The kinetic energy matrix is diagonal and its terms are defined in Equation 2.16. Under periodic boundary conditions the potential can be expressed as the plane-wave expansion in Equation 2.17, supported by the same reciprocal space grid as the KS orbitals. The reverse Fourier transform which recovers the components $V_{\text{eff}}(\mathbf{G}_j)$ from the real-space potential is given in Equation 2.18. The

matrix elements are then given in Equation 2.19.

$$\langle \mathbf{k}+\mathbf{G}'| -\frac{1}{2}\nabla^2 |\mathbf{k}+\mathbf{G}\rangle = \frac{1}{2}|q|^2 \delta_{\mathbf{G}\mathbf{G}'} \tag{2.16}$$

$$V_{\text{eff}}(\mathbf{r}) = \sum_j V_{\text{eff}}(\mathbf{G}_j)\exp\left[i\,\mathbf{G}_j\cdot\mathbf{r}\right] \tag{2.17}$$

$$V_{\text{eff}}(\mathbf{G}) = \frac{1}{\Omega}\int_\Omega \mathrm{d}^3 r V_{\text{eff}}(\mathbf{r})\exp\left[-i\,\mathbf{G}\cdot\mathbf{r}\right] \tag{2.18}$$

$$\langle \mathbf{k}+\mathbf{G}'|\, V_{\text{eff}}\, |\mathbf{k}+\mathbf{G}\rangle = \sum_j V_{\text{eff}}(\mathbf{G}_j)\delta_{\mathbf{G}_j,\mathbf{G}-\mathbf{G}'} \tag{2.19}$$

The Fourier sums are infinite, but in practice are truncated at some $\mathbf{G}_{\text{max}}$. The cutoff is typically expressed in an energy representing a maximum kinetic energy of the plane-waves included in the sums at a given k-point, $E_{\text{cutoff}} \geq \frac{1}{2}|\mathbf{k}+\mathbf{G}_{\text{max}}|^2$.

2.1.3 Linear-Scaling Density Functional Theory in ONETEP

Density Matrix Approaches

The solution to the Kohn-Sham equations incurs a computational cost that scales cubically with the number of electrons in the system. For example, mutually orthogonalizing the Kohn-Sham eigenstates costs $\mathcal{O}(M^2)\times\mathcal{O}(N)$ where M is the number of occupied states and N is the number of basis functions used. The cubic cost quickly limits the size of problem that can be feasibly handled with DFT to hundreds of atoms. ONETEP [57, 58] and other linear-scaling DFT packages employ a density matrix approach, which avoids the explicit solution of the Kohn-Sham equations and, in principle, scales favourably into the thousands and tens-of-thousands of atoms. The central quantity of these approaches is the single-particle density matrix $n(\mathbf{r},\mathbf{r}')$, constructed as in Equation 2.20, where $f_i \in [0,1]$ is the occupancy of the i-th Kohn-Sham state of spin σ.

$$n^\sigma(\mathbf{r},\mathbf{r}') = \sum_i f_i \psi^{*\sigma}_i(\mathbf{r})\psi^\sigma_i(\mathbf{r}') \tag{2.20}$$

The electron density can be recovered by noting that $n(\mathbf{r}) = \sum_\sigma n^\sigma(\mathbf{r},\mathbf{r})$. The expectation value of an operator $\hat{Q}$ can be calculated as $\mathrm{tr}(\hat{n}\hat{Q})$ allowing, for example, the independent-particle kinetic energy T_{s} and Kohn-Sham effective potential energy E_{eff} to be expressed as in Equations 2.21 and 2.22 respectively.

$$T_{\text{s}} = -\frac{1}{2}\sum_\sigma \int \mathrm{d}^3 r' \nabla^2_{\mathbf{r}} n^\sigma(\mathbf{r},\mathbf{r}')|_{\mathbf{r}=\mathbf{r}'} \tag{2.21}$$

$$E_{\text{eff}} = \sum_{\sigma} \int \mathrm{d}^3 r' n^{\sigma}(\mathbf{r}, \mathbf{r}') V_{\text{eff}}(\mathbf{r}')|_{\mathbf{r}=\mathbf{r}'} \tag{2.22}$$

It is thus possible to evaluate total energies from the density matrix as in Equation 2.23, where the second term accounts for double-counting.

$$E_{\text{tot}} = \text{tr}(\hat{n}\hat{H}_{\text{KS}}) - E_{\text{dc}}[n(\mathbf{r})] \tag{2.23}$$

The density matrix is normalized to the total number of electrons in each spin channel N_σ as in Equation 2.24. If the occupancies f_i are restricted to be either 0 or 1, as is the case of insulators and zero-temperature metals, the density matrix is also idempotent, as defined in Equation 2.25. Idempotency is an expression of the orthogonality of the Kohn-Sham states, as can be seen by expanding the density matrices on the left hand side of Equation 2.25 as in Equation 2.20.

$$\int \mathrm{d}^3 r n^{\sigma}(\mathbf{r}, \mathbf{r}) = N_\sigma \tag{2.24}$$

$$\int \mathrm{d}^3 r'' n^{\sigma}(\mathbf{r}, \mathbf{r}'') n^{\sigma}(\mathbf{r}'', \mathbf{r}') = n^{\sigma}(\mathbf{r}, \mathbf{r}') \tag{2.25}$$

Using these properties as constraints, the energy in Equation 2.23, and thus the Kohn-Sham total energy, can be minimized with respect to the density matrix, avoiding cubic-scaling computational costs related to the solution of the Kohn-Sham equations. A description of the approach to maintaining idempotency and normalization of the density matrix in ONETEP can be found in Reference [71].

It has been shown analytically and numerically [72–74] that $n(\mathbf{r}, \mathbf{r}')$ for an insulator and a finite-temperature metal decays exponentially as $|\mathbf{r} - \mathbf{r}'|$ grows. The decay has been shown to be related to the size of the band gap such that a larger band gap decreases the range of the density matrix [72]. This limited range allows the density matrix to be truncated at some suitable cutoff r_{cut} so that $n(\mathbf{r}, \mathbf{r}') = 0$ when $|\mathbf{r} - \mathbf{r}'| \geq r_{\text{cut}}$. A representation of the 'near-sighted' density matrix in some suitable spatially-localized basis results in a sparse matrix whose size only grows linearly with the addition of atoms.

NGWFs

ONETEP and other linear-scaling codes re-express the density matrix in terms of the density kernel $K^{\alpha\beta}$, a sparse matrix defined by Equation 2.26. Note that summation convention is implied by Greek indices, except the spin label σ. The 'support' functions

ϕ_α are spatially localized, typically around ionic centres, and are bi-orthogonal to their contravariant duals; $\int \mathrm{d}^3 r \phi^\alpha(\mathbf{r})\phi_\beta(\mathbf{r}) = \delta^\alpha{}_\beta$.

$$n^\sigma(\mathbf{r},\mathbf{r}') = \phi^{*\sigma}_{\ \alpha}(\mathbf{r}) K^{\sigma,\alpha\beta} \phi^\sigma{}_\beta(\mathbf{r}') \tag{2.26}$$

The use of spatially localized support functions means the overlap matrix $S_{\alpha\beta} = \int \mathrm{d}^3 r \phi^*_\alpha(\mathbf{r})\phi_\beta(\mathbf{r})$ is also sparse and grows linearly with support function count. Inspection of the components of the Hamiltonian in Equation 2.9 show that the Hamiltonian has the same property. The total energy in Equation 2.23 can then be reformulated in terms of linear-scaling sparse matrices as Equation 2.27. The normalization and idempotency conditions can also be expressed in terms of these sparse matrices as Equations 2.28 and 2.29 respectively.

$$E_{\mathrm{tot}} = \sum_\sigma K^{\sigma,\alpha\beta} H^\sigma{}_{\alpha\beta} - E_{\mathrm{dc}}[n] \tag{2.27}$$

$$K^{\sigma,\alpha\beta} S^\sigma{}_{\beta\alpha} = N_\sigma \tag{2.28}$$

$$K^{\sigma,\alpha\beta} = K^{\sigma,\alpha\gamma} S^\sigma{}_{\gamma\delta} K^{\sigma,\delta\beta} \tag{2.29}$$

There are a number of physically-motivated options available for the localized support functions $\phi_\alpha(\mathbf{r})$. A common selection is a linear combination of functions resembling atomic orbitals as used in, for example, SIESTA [75]. These orbitals are intuitive and can provide a good description of chemical bonds with a small number of support functions, but cannot be systematically improved and require human input into the selection of orbital types used. ONETEP makes use of functions that are initialized to be atomic orbital-like but can be optimized *in situ*, illustrated in Figure 2.1 [76]. These functions, called Non-orthogonal Generalized Wannier Functions [77] (NGWFs), are designed to minimize the number of support functions required to accurately describe the system without sacrificing transferability. They are localized by restricting them to be non-zero only inside of an atom-centred sphere of fixed, user-defined radius. Figure 2.2a shows one localized NGWF centred on the branching carbon atom of a 4-Methyl-1-pentene molecule [78]. This NGWF was initialized like a p orbital and has adapted to its local environment. This is contrasted with Figure 2.2b which shows one Kohn-Sham orbital that spans the entire molecule.

It is important to note that ONETEP currently imposes a restriction on spin-polarized calculations that the same NGWFs are used in each spin channel. This effectively

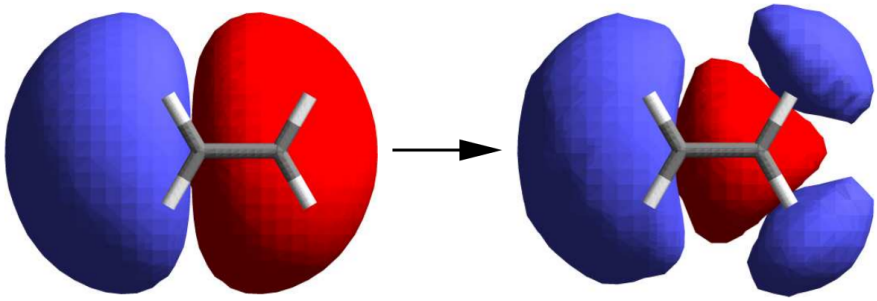

Fig. 2.1 An NGWF initialized as a p orbital optimizing *in situ*. It is not restricted to the symmetry of the p orbital it was initialized to. By optimizing the basis the density kernel is expressed in, a minimal basis set can be generated automatically. Image source: [79], reproduced with permission from Wiley.

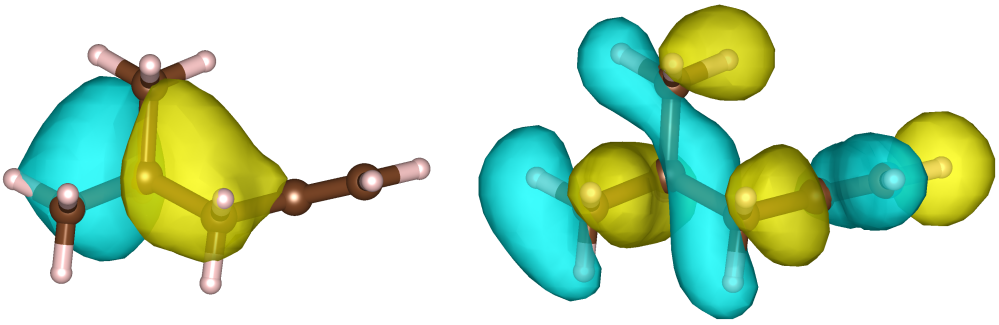

(a) NGWF (b) Kohn-Sham Orbital

Fig. 2.2 A 4-Methyl-1-pentene molecule with an isosurface of (a) a p-like NGWF of the branching carbon atom, which can be non-zero only in a sphere centered on the atom and (b) one Kohn-Sham orbital which can be nonzero across the entire system.

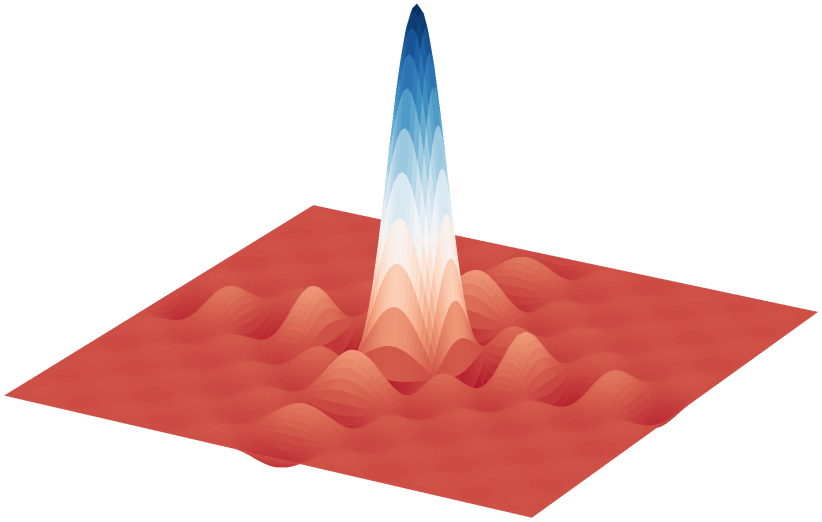

Fig. 2.3 A psinc function. It is zero at all grid-points except the origin and its periodic images. It is used to represent NGWFs in ONETEP because it retains key properties of the delta function while having a finite Fourier expansion.

halves the number of NGWFs required to do spin-polarized calculations, though an extension to optionally enable spin-polarized NGWFs is in development.

In order to optimize the NGWFs they are represented in a basis of delta functions on a regular real-space grid. By imposing periodic boundary conditions, the regular grid can be expressed conveniently as a finite Fourier series. This replaces the delta functions with psinc functions $D_{KLM}(\mathbf{r})$ shown in Figure 2.3 and defined in Equation 2.30, where K, L, and M are indices of the real-space grid with $2J_i + 1 \equiv N_i$ grid-points in the direction of lattice vector $\mathbf{A}_i$. $\mathbf{B}_i$ are the reciprocal lattice vectors and $\mathbf{r}_{KLM}$ is the position of grid-point (K, L, M).

$$D_{KLM}(\mathbf{r}) \equiv D_{000}(\mathbf{r} - \mathbf{r}_{KLM}) = \frac{1}{N_1 N_2 N_3} \sum_{P=-J_1}^{J_1} \sum_{Q=-J_2}^{J_2} \sum_{R=-J_3}^{J_3} e^{i(P\mathbf{B}_1 + Q\mathbf{B}_2 + R\mathbf{B}_3 +)\cdot(\mathbf{r}-\mathbf{r}_{KLM})} \tag{2.30}$$

The psinc basis retains the important property of the delta function basis that $D_{KLM}(\mathbf{r}_{VST}) = \delta_{KV}\delta_{LS}\delta_{MT}$, while also allowing the NGWFs to be represented simply in both the psinc and plane-wave basis as shown in Equations 2.31 and 2.32, respectively. Here, the plane-wave expansion coefficients $c_{PQR,\alpha}$ are related to the psinc expansion coefficients $C_{KLM,\alpha}$ by a discrete Fourier transform and V is the volume of the simulation cell. The localization condition on the NGWFs means that $C_{KLM,\alpha} = 0$ for $\mathbf{r}_{KLM}$

outside of the localization sphere α.

$$\phi_\alpha(\mathbf{r}) = \sum_{K=0}^{N_1-1} \sum_{L=0}^{N_2-1} \sum_{M=0}^{N_3-1} C_{KLM,\alpha} D_{KLM}(\mathbf{r}) \tag{2.31}$$

$$\phi_\alpha(\mathbf{r}) = \sum_{P=-J_1}^{J_1} \sum_{Q=-J_2}^{J_2} \sum_{R=-J_3}^{J_3} c_{PQR,\alpha} e^{i(P\mathbf{B}_1+Q\mathbf{B}_2+R\mathbf{B}_3)\cdot\mathbf{r}} \tag{2.32}$$

The projection of a function $f(\mathbf{r})$ onto a psinc basis function is given in Equation 2.33, where $f_D(\mathbf{r})$ is the Fourier series representation of the function with the same bandwidth-limiting as the basis and W is the volume of the simulation cell per grid-point. Using the orthogonality of the psinc functions, an overlap between $f(\mathbf{r})$ and any function represented on the psinc grid can therefore be calculated exactly as a sum over grid-points.

$$\int \mathrm{d}^3 r D_{KLM}(\mathbf{r}) f(\mathbf{r}) = W f_D(\mathbf{r}) \tag{2.33}$$

A fine psinc grid is also required which has twice the number of gridpoints in each direction. This is because the product of two psinc functions is a linear combination of fine-grid psinc functions. Using these tools, energy functionals can be calculated with integrals being calculated as simple summations over the grid or fine grid. The fact that the basis functions can be expressed simply as sums of plane-waves allows the Laplacian present in the single-particle kinetic energy operator to be handled trivially as a constant multiplying each plane-wave element. The only functional calculation that is in principle non-exact is the exchange-correlation functional which generally contains highly non-local terms that cannot be represented as sums over the grid or fine grid. However, the errors incurred by the approximation are also present in conventional wave function-based DFT approaches and are expected to be small [69].

While the localization of the NGWFs restricts the $C_{KLM,\alpha}$ to be zero outside of the localization sphere of ϕ_α, this localization is not carried over to reciprocal space; each psinc function is expanded in the set of plane-waves that are supported by the entire real-space grid. The number of grid-points and therefore the number of plane-waves scales with the size of the system, restoring a cubic scaling cost to the calculation. An efficient solution to this problem is the FFT box technique [80], which reformulates the psinc expansions in a way that is independent of system size while still maintaining key properties of operators such as Hermiticity. The new expansion includes only contributions from plane-waves supported by grid-points in a smaller parallelepiped that is geometrically similar to the simulation cell. The box must have its origin on

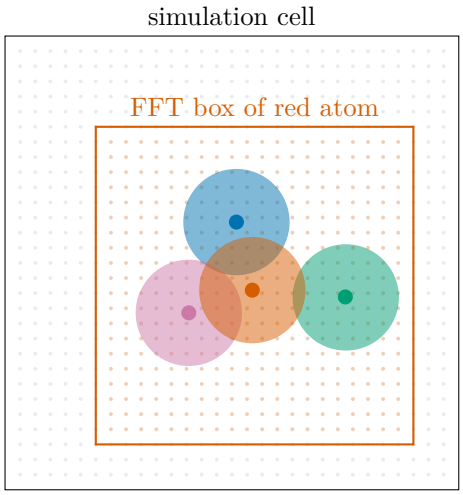

Fig. 2.4 Illustration of the FFT Box of an NGWF. It is large enough to contain any possible overlapping NGWF. In plane-wave expansions, only those supported by the gridpoints of this smaller box need be included, restoring linear scaling to reciprocal space calculations.

a grid-point of the full cell. This approach is illustrated in Figure 2.4. It has been shown that as long as the FFT box is large enough to contain any possible orientation of overlapping NGWFs, integrals between NGWFs can be calculated out using the box-limited psinc functions without sacrificing accuracy [80]. A similar approach is taken for evaluations on the fine grid.

Because both the density kernel and the NGWFs must be optimized, a double-loop optimization is performed, illustrated in Figure 2.5. The minimal energy E_{min} is obtained by Equation 2.34, where $L(\{C^{\sigma}_{KLM,\alpha}\})$ is defined in Equation 2.35 and the spin index σ has been reintroduced.

$$E_{\text{min}} = \min_{\{C^{\sigma}_{KLM,\alpha}\}} L(C^{\sigma}_{KLM,\alpha}) \tag{2.34}$$

$$L(C^{\sigma}_{KLM,\alpha}) = \min_{\{K^{\sigma,\alpha\beta}\}} E(\{K^{\sigma,\alpha\beta}\}, \{C^{\sigma}_{KLM,\alpha}\}) \tag{2.35}$$

The minimization in 2.35 also includes the imposition of the normalization and idempotency constraints in Equations 2.28 and 2.29 respectively. Many methods can be selected to do this constrained optimization; ONETEP uses a modification of the LNV method developed by Millam and Scuseria [81].

ONETEP provides a linear-scaling density matrix approach to DFT which is essentially a reformulation of traditional plane-wave DFT. It offers systematic convergence

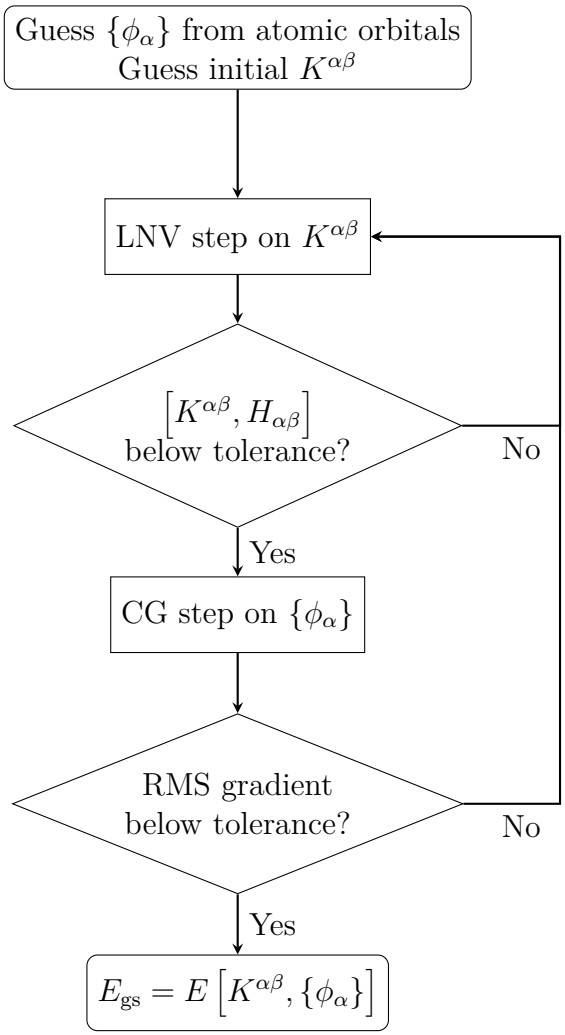

Fig. 2.5 An outline of the electronic energy minimization procedure in ONETEP. For a given set of NGWFs the normalized density kernel is optimized to minimize energy with a penalty on non-idempotency. The NGWFs are then updated with conjugate gradients until they converge.

with respect to the spacing of the psinc grid in an analogous sense to the reciprocal-space grid spacing controlling convergence in plane-wave DFT. It has been shown in a study on crystalline silicon [82] that increasing the cutoff radius of the NGWFs also systematically converges quantities calculated in ONETEP to plane-wave accuracy.

2.1.4 Projector Augmented-Wave Method in ONETEP

A bottleneck of DFT methods is the cost of accurately representing valence wave functions near ionic cores. Because they must be orthogonal to core states they have many nodes in this region which generally leads to a larger basis set requirement. Deep core states are not relevant to bonding and only contribute this orthogonality constraint on the valence wave functions. A widely used solution is the pseudopotential method proposed originally by Hellman [83]. This approach replaces the ions and frozen core elections with a pseudo-ion with an effective potential that deviates from the all-electron potential only within some cutoff radius r_c. Within this radius the valence wave functions do not meet the same orthogonality constraints and can vary smoothly, allowing a smaller basis set to be used, while still matching the all-electron result outside the cutoff radius where chemical interactions occur. Modern calculations typically use either norm-conserving [84] or ultrasoft [85] pseudopotentials.

The projector augmented-wave method (PAW) [86] is an alternative approach that allows the all-electron wave function to be reconstructed when needed. Inside ion-centred spherical augmentation regions the all-electron wave-function is replaced with a smooth pseudo-wave function, but projectors are maintained that allow the frozen core wave-function packaged with the PAW dataset to be recovered when required. The ability to recover the full wave-function means that PAW calculations are essentially all-electron calculations and can be highly accurate. This approach also relaxes the norm-conserving constraints put on classic pseudopotentials, allowing for a much 'softer' approximation requiring fewer basis functions.

PAW has been recently implemented in ONETEP [87]. Its implementation is similar to that of the ABINIT code [88].

2.1.5 Ensemble DFT in ONETEP

Calculations on systems that do not have a significant band gap such as metals can cause issues for standard DFT methods including linear-scaling DFT. These problems

are related to discontinuities in orbital occupancies near the Fermi level when the occupancies are restricted to be strictly integers [61].

Mermin extended density functional theory to apply to an ensemble of states at finite electronic temperature [89]. The molecular orbital occupancies in Equation 2.20 are now not restricted to be integers, and are instead determined by the orbital energies $\{\epsilon_i\}$ and the Fermi-Dirac distribution in Equation 2.36 at a given temperature T. The chemical potential μ is determined by the number of electrons in the system.

$$f_i(T) = \frac{1}{1 + \exp\left(\frac{\epsilon_i - \mu}{k_\mathrm{B} T}\right)} \tag{2.36}$$

The use of this occupancy smearing also introduces an entropy term defined in Equation 2.37. The functional to be minimized is then the Helmholtz free energy defined in Equation 2.38.

$$S(\{f_i\}) = -k_\mathrm{B} \sum_i \left[f_i \ln f_i + (1 - f_i) \ln (1 - f_i)\right] \tag{2.37}$$

$$A[T, \{|\psi_i\rangle\}] = E_\mathrm{KS}[\{|\psi_i\rangle\}] - TS[f_i] \tag{2.38}$$

In ONETEP the molecular orbitals $\{|\psi_i\rangle\}$ are expanded in the set of NGWFs $\{|\phi_\alpha\rangle\}$ as in Equation 2.39 with M_i^α being the expansion coefficients.

$$|\psi_i\rangle = M_i^\alpha |\phi_\alpha\rangle \tag{2.39}$$

The Kohn-Sham equations can be expressed in the NGWF representation as Equation 2.40 with the Hamiltonian matrix $H_{\alpha\beta}$ defined in Equation 2.41.

$$H_{\alpha\beta} M_i^\beta = S_{\alpha\beta} M_i^\beta \epsilon_i \tag{2.40}$$

$$H_{\alpha\beta} = S_{\alpha\gamma} \sum_i (M_i^\gamma \epsilon_i M_i^{\dagger\delta}) S_{\delta\beta} \tag{2.41}$$

A functional form of the Helmholtz free energy can then be defined in the NGWF representation and minimized. This functional is given by Equation 2.42. The occupancies $\{f_i\}$ can be determined from the $\{\epsilon_i\}$ obtained from solving the Kohn-Sham equations for a given Hamiltonian and set of NGWFs.

$$A\left[T, \{H_{\alpha\beta}\}, \{|\phi_\alpha\rangle\}\right] = K^{\alpha\beta} \langle\phi_\beta| \hat{T} + \hat{V}_\mathrm{ext} |\phi_\alpha\rangle + E_\mathrm{H}[n] + E_\mathrm{XC}[n] - TS[\{f_i\}] \tag{2.42}$$

ONETEP finds the Hamiltonian and NGWFs that minimize the free energy A in a nested loop. In the inner loop, the Hamiltonian is minimized for a fixed set of NGWFs. The incoming Hamiltonian matrix $H_{\alpha\beta}$ is diagonalized to find the energy eigenvalues and occupancies. A new density is generated and from it a new Hamiltonian $\tilde{H}_{\alpha\beta}$ is created. A line search in the space of Hamiltonians is then performed in the direction of $\Delta_{\alpha\beta} = \tilde{H}_{\alpha\beta} - H_{\alpha\beta}$. In the outer loop, conjugate gradients minimization of a projected free energy functional with respect to the NGWFs is performed with a fixed Hamiltonian.

Forces in EDFT

The partial occupancies of bands in ensemble DFT introduces a term in energy gradients that must be included for force calculations. These terms depend on the occupancy distribution used. It has been shown [90] that in the case of Fermi smearing these additional gradient terms due to fractional occupancies exactly cancel the free energy functional gradient contribution due to entropy. For this reason, forces in EDFT calculations are calculated as gradients of the free energy functional and do not require any additional terms compared to the forces in linear-scaling ONETEP calculations.

2.2 Formation Energy Calculations

Surface adsorption energies are useful for identifying which of several sites are favourable for a species to adsorb to. The adsorption energy of a species E_{bind} is given in Equation 2.43, where the terms on the right-hand side of the equation are the total energies of the adsorbed surface, the clean surface, and the isolated adsorbate optimized in a sufficiently large simulation cell, respectively. By this sign convention larger negative adsorption energies correspond to more strongly adsorbed species.

$$\Delta E_{\text{bind}} = E_{\text{surf+ads}} - E_{\text{surf}} - E_{\text{ads}} \tag{2.43}$$

While useful, adsorption energy is a 0 K quantity that also does not involve the partial pressure of the species. It lacks information about the conditions under which a species would favourably adsorb on a surface rather than remaining in the gas phase. This requires the formation energy ΔE_f of an adsorbate α defined in Equation 2.44. Here, $E_{\text{surf}+\alpha}$ is the total energy of the adsorbed system, E_{surf} is the total energy of the pristine surface, and $\mu_\alpha(T, p_\alpha)$ is a chemical potential of the adsorbate α at

temperature T and partial pressure of α p_α.

$$\Delta E_f = E_{\text{surf}+\alpha} - E_{\text{surf}} - \mu_\alpha\left(T, p_\alpha\right) \tag{2.44}$$

The first two terms of Equation 2.44 are available from the adsorption energy calculation. The chemical potential term requires consideration of the surface to be in contact with a reservoir of adsorbate particles at temperature T and (partial) pressure p_α. Taking an example of carbon monoxide adsorption, the chemical potential at a given temperature and partial pressure is given by Equation 2.45, where $\Delta G^0_{\text{CO (g)}}$ is the Gibbs free energy of formation of carbon monoxide from standard reference states of carbon and oxygen (graphene and molecular oxygen) at standard temperature and pressure, the chemical potentials for carbon and oxygen are the energies of forming the chemical reference states from the DFT reference states (they are essentially zero-of-energy correction terms), and the final term contains the change in chemical potential under different conditions based on ideal rigid dumbbells, given in Equation 2.46. $C^0_{P(\text{CO})}$ is the constant-pressure heat capacity of CO represented as an ideal diatomic gas. p^0 and T^0 are the standard pressure and temperature, 1 atm and 273.15 K respectively.

$$\mu_{\text{CO}}(T, p_{\text{CO}}) = \Delta G^0_{\text{CO (g)}} + \mu_C + \mu^0_{1/2[\text{O}_2\,\text{(g)}]} + \Delta\mu_{\text{CO}}(T, p_{\text{CO}}) \tag{2.45}$$

$$\Delta\mu_{\text{CO}}(T, p_{\text{CO}}) = k_b T \ln\left[\frac{p_{\text{CO}}}{p^0}\right] - \left(S^0_{\text{CO}} - C^0_{P(\text{CO})}\right)(T - T^0) - C^0_{P(\text{CO})} T \ln\left[\frac{T}{T^0}\right] \tag{2.46}$$

While $\Delta G^0_{\text{CO (g)}}$ as well as the standard entropies and constant-pressure heat capacity are known from experiment or from the ideal gas approximation, the chemical potentials μ_C and $\mu^0_{1/2[\text{O}_2\,\text{(g)}]}$ must be calculated from DFT results. This is straightforward for μ_C under the assumption that it is not very dependent on temperature. However, calculation of $\mu^0_{1/2[\text{O}_2\,\text{(g)}]}$ requires DFT calculation on a gas-phase molecule with nonzero temperature and pressure effects. An approach by Finnis *et al.* [91, 92] formulates the energy in a way that does not require direct calculation of gas-phase total energies by making use of experimental values. Consider that the oxygen reference is in (perhaps highly unfavourable) equilibrium with some oxide species that could form, for example bulk cobalt(II) oxide CoO. The experimentally known standard Gibbs free energy of formation is given in Equation 2.47 where again the 0 superscript is dropped where it is assumed that there is negligible dependence of energies on temperature or pressure.

$$\Delta G^0_{\text{CoO (s)}} = \mu_{\text{CoO (s)}} - \mu_{\text{Co}(s)} - \mu^0_{1/2[\text{O}_2\,\text{(g)}]} \tag{2.47}$$

Reordering Equation 2.47 yields a value of $\mu^0_{1/2[O_2\,(g)]}$ that can be calculated from experimental results and DFT calculations on solids only. Along with Equations 2.44, 2.45, and 2.46 (and the related assumptions discussed) this provides a methodology for accurately calculating formation energies involving gas-phase species without the need to perform DFT calculations on them.

2.3 Transition State Searching

Geometry optimization is a common and powerful tool in computational materials research. With the use of the Hellman-Feynman theorem [93] and efficient non-linear optimization methods, it provides a computationally cheap approach to structure prediction. However, geometry optimization cannot provide information about minimum energy paths connecting optimized structures or their saddle-point transition state structures. These are important for the construction of kinetic models for predicting activation energies for chemical reactions. For the purposes of this discussion, a minimum energy path is completely defined by the transition state or states on the path as the loci formed by steepest descent from each transition state to the energy minima in such a way that the reactant and product are connected. It should be noted that there is some additional care required to complete this definition for general degrees of freedom and also some discussion as to its applicability as a reaction coordinate [94].

2.3.1 Synchronous Transit

Often times only the transition state energy or structure is of interest, and the shape of the minimum energy path is unimportant. Even if the minimum energy pathway is to be used as a reaction coordinate of some kind, a single transition state connecting two minima fully defines the minimum energy path passing through that transition state between those two minima. Some approaches attempt to find the transition state without working backwards from an expensive determination of the minimum energy path or an even more expensive manual search of the potential energy surface for saddle points. The synchronous transit class of approaches fall in this category.

The basic approach to synchronous transit, 'LST/QST' [95, 96], is illustrated in Figure 2.6. In linear synchronous transit (LST) the maximum energy point on the linear interpolation between the product and the reactant is first located. This attempts to locate the saddle region and can be used as a transition state guess, though this state is

likely to have ridden up the saddle region walls. Instead, this guess structure is typically optimized orthogonal to the linear interpolation direction in configuration space. The resulting structure is the LST transititon state guess. In the quadratic extension (QST), this guess intermediate along with the two endpoints are interpolated with a parabola in configuration space. The QST guess intermediate is the highest-energy point along this parabola. This has been shown to be sufficient for simple pathways, but it makes clear and limiting assumptions about the nature of the minimum energy that prevent strong guarentees about the identified structure.

A number of improvements to this algorithm exist. One method [96] uses the LST/QST lines to approximate directions of negative curvature of the potential energy surface, starting with the initial LST maximum. If the saddle point is of first order, defined by its Hessian having exactly one negative eigenvalue, iterative conjugate-gradients searches utilizing an approximation that the synchronous transit methods provide an estimate for the negative curvature direction of the saddle region, allowing the energy to be maximized in that direction and minimized in all others. Occasional QST line maximizations should be performed to reset the negative-curvature direction and conjugate-gradients minimization. This has been demonstrated to be an improvement on LST/QST, but does not fundamentally improve the fact that synchronous transit methods are not rigorous.

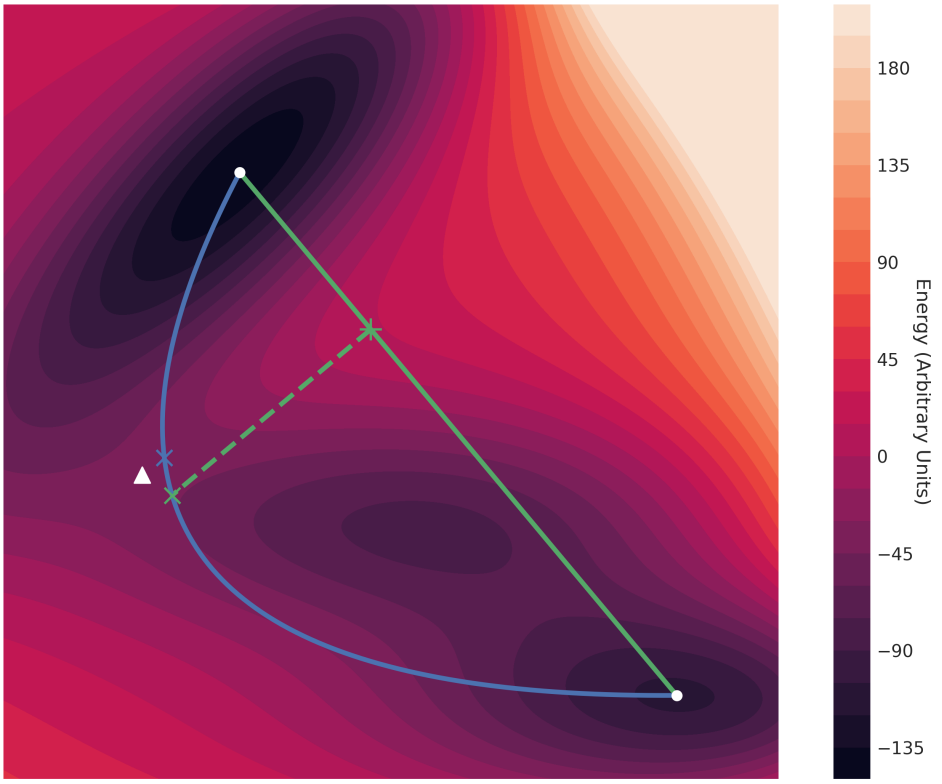

Fig. 2.6 A cartoon of the LST/QST approach to transition state searching over a Müller-Brown potential [97]. The reactant and product configurations are designated by white dots and the true transition state between them with a white triangle. The LST procedure is in green. The highest energy point on the linear interpolation between reactant and product is marked with a "+". A minimisation orthogonal to this is then performed, with lowest-energy point marked here with a green "X". This is the LST approximation to the transition state. The QST improvement finds the maximum energy point on the parabola passing through the reactant, product, and LST approximation, marked in blue with a blue "X" at the maximum. This image is not the result of simulations but is illustrative.

2.3.2 Nudged Elastic Band

The nudged elastic band (NEB) method is a robust approach to minimum energy path prediction. Consider constructing a chain between a reactant and product with a sequence of intermediate structures, or 'beads', connected to adjacent beads by springs of natural length 0. A geometry optimization of the beads in this chain, where the force on each bead is the sum of the real force and the spring forces from its two neighbors, provides an approximation to the minimum energy path. Two issues arise as a result of the 'plain' elastic band approach. The spring force acts to pull the beads off the minimum energy path, providing an overestimation of the transition state energy. Figure 2.7(a) illustrates this 'corner-cutting' for a simple potential energy surface and a spring constant of 1.0. This effect exists even in the infinite-bead limit [98]. Reducing the spring constant brings the beads closer to the minimum energy path, but promotes 'slipping' of the beads near the saddle point, reducing bead sampling near the transition state. This is illustrated in Figure 2.7(b) using the same potential energy surface but a spring constant of 0.1.

Corner-cutting is a result of the spring force perpendicular to the path, while slipping around the saddle point region is a result of the real force parallel to the path. The nudged elastic band method systematically fixes these issues by projecting out or 'nudging' these force components [99]. The force on bead i is now given by Equation 2.48, where the nudged spring force $\mathbf{f}^s_{i\,||}$ is given by Equation 2.49 and the nudged real force is $-\nabla V(\mathbf{r}_i)_\perp$ is defined in Equation 2.50. k is the spring constant of the chain springs and $\hat{\boldsymbol{\tau}}_i$ is the unit tangent to the path at $\mathbf{r}_i$.

$$\mathbf{f}_i = \mathbf{f}^s_{i\,||} - \nabla V(\mathbf{r}_i)_\perp \tag{2.48}$$

$$\mathbf{f}^s_{i\,||} = k(|\mathbf{r}_{i+1} - \mathbf{r}_i| - |\mathbf{r}_i - \mathbf{r}_{i-1}|)\hat{\boldsymbol{\tau}}_i \tag{2.49}$$

$$\nabla V(\mathbf{r}_i)_\perp = \nabla V(\mathbf{r}_i) - (\nabla V(\mathbf{r}_i) \cdot \hat{\boldsymbol{\tau}}_i)\hat{\boldsymbol{\tau}}_i \tag{2.50}$$

The result of nudging is a path that in principle is decoupled from its discrete representation, up to an approximation of the path tangent at each bead, and that lies strictly on the minimum energy path when converged. Additionally, the spring constant in the nudged band only affects the spacing of beads along the path. Figure 2.7(c) illustrates the NEB result on the same potential energy surface.

One common addition to the NEB method is a climbing image (Ci-NEB). The highest energy bead is chosen to feel no spring force and to move up the path to better

sample the transition state. The force on this bead is given in Equation 2.51. An illustration of this improvement is shown in 2.7(d).

$$\mathbf{f}_{\mathrm{ci}} = -\nabla V(\mathbf{r}_{\mathrm{ci}}) + 2[\nabla V(\mathbf{r}_{\mathrm{ci}}) \cdot \hat{\boldsymbol{\tau}}_{\mathrm{ci}}]\hat{\boldsymbol{\tau}}_{\mathrm{ci}} \tag{2.51}$$

Given enough beads to resolve the path, NEB robustly converges to a path connecting two minima on a potential energy surface. However, as one might imagine by picturing stretching a physical elastic band over a complex surface, the final path is dependant on the initial placement of the beads. There is therefore no guarantee that that the path found is the correct global minimum energy path. This must be considered when using this method.

Path Tangent Approximation

Because NEB utilizes a discrete representation of the minimum energy path, an approximation to the path tangent at a given bead's position must be chosen. Several options exist including a weighted or unweighted combination of the relative positions of its neighbors. An 'upwinding' tangent approximation has been suggested [102] in which the tangent at points that are not at energy extrema are determined solely by the relative position of the higher-energy neighbor, while points at extrema take a weighted average of its two neighbors' relative positions. This approximation acts to prevent the 'kinking' of the path that otherwise occurs in some situations, previously preventing correct minimum energy path sampling.

Bead i has position $\mathbf{R}_i$ and total energy E_i. In the case that it is not at an extremum its (non-normalized) path tangent approximation $\boldsymbol{\tau}_i$ is given by Equation 2.52, where $\boldsymbol{\tau}_i^+$ and $\boldsymbol{\tau}_i^-$ are defined in Equation 2.53.

$$\boldsymbol{\tau}_i = \begin{cases} \boldsymbol{\tau}_i^+; & E_{i+1} > E_i > E_{i-1}, \\ \boldsymbol{\tau}_i^-; & E_{i+1} < E_i < E_{i-1} \end{cases} \tag{2.52}$$

$$\boldsymbol{\tau}_i^+ = \mathbf{R}_{i+1} - \mathbf{R}_i; \qquad \boldsymbol{\tau}_i^- = \mathbf{R}_i - \mathbf{R}_{i-1} \tag{2.53}$$

If bead i is at an extremum, its tangent approximation is a weighted average of $\boldsymbol{\tau}_i^+$ and $\boldsymbol{\tau}_i^-$ whose weights are determined by the neighbor energies as in Equation 2.54.

Here $\Delta E_i^{\max}$ and $\Delta E_i^{\min}$ are defined in Equations 2.55 and 2.56 respectively.

$$\boldsymbol{\tau}_i = \begin{cases} \Delta E_i^{\max} \boldsymbol{\tau}_i^+ + \Delta E_i^{\min} \boldsymbol{\tau}_i^-; & E_{i+1} > E_{i-1}, \\ \Delta E_i^{\min} \boldsymbol{\tau}_i^+ + \Delta E_i^{\max} \boldsymbol{\tau}_i^-; & E_{i+1} < E_{i-1} \end{cases} \tag{2.54}$$

$$\Delta E_i^{\max} = \max\left(|E_{i+1} - E_i|, |E_i - Ei - 1|\right) \tag{2.55}$$

$$\Delta E_i^{\min} = \min\left(|E_{i+1} - E_i|, |E_i - Ei - 1|\right) \tag{2.56}$$

2.3.3 Improved Nudged Spring Force

In addition to the upwinding tangent, Henkelman's improved approach [102] included a modified nudged spring force given in Equation 2.57. This ensures the images remain properly spaced even in regions of high path curvature. Here the springs are assumed to have the same spring constant k.

$$\mathbf{f}_{i\,||\text{new}}^{s} = k\left(|\mathbf{R}_{i+1} - \mathbf{R}_i| - |\mathbf{R}_i - \mathbf{R}_{i-1}|\right)\hat{\boldsymbol{\tau}}_i \tag{2.57}$$

2.3.4 Updating Bead Positions

In practice the evolution of the chain must be handled in discrete steps (macroiterations) using some iterative nonlinear solver. A number of options exist, with quasi-Newton and molecular dynamics based methods being particularly attractive for their fast convergence and relative robustness. A review of several approaches specifically for updating a NEB chain was performed by Sheppard *et al.* [103]. The proposed approach was a L-BFGS [104] update approximating the inverse Hessian of the entire chain applied to the vector of positions of atoms in all NEB beads concatenated together. This approach is termed 'global L-BFGS' or 'GL-BFGS' and was shown to be superior to simply performing an L-BFGS update on each image individually, which approximates an inverse Hessian that does not include inter-image interactions. This can be performed with or without a line search, with the latter approach reportedly converging in fewer overall energy and force calculations.

Sheppard *et al.* [103] also compared first-order methods including steepest descents, conjugate gradients, quick-min [105], and the 'Fast inertial relaxation engine' (FIRE) [106]. Quick-min is a molecular dynamics based approach that that accelerates the system in the direction of the force until the velocity projection on the force is negative, at which point it resets. FIRE is a similar method that retains momentum,

using the velocity projection on the force to apply an acceleration to the current minimization direction and stopping when going uphill. FIRE was found to be the superior choice of this class of methods for use in NEB [103] and a more detailed description of the method is given below.

The L-BFGS Method

The BFGS algorithm [107] iteratively approximates the inverse Hessian of the system to be minimized to determine update steps by solving the analogue to Newton's equation given in Equation 2.58. Here H_i is the approximation to the inverse Hessian matrix at iteration i, $\mathbf{F}_i$ is the force vector obtained by concatenating the forces on each ion, and $\mathbf{x}_i$ is the resulting update step to reach the approximated minimum. The inverse Hessian approximation is then updated according to the update formula in Equation 2.59 where $\mathbf{s}_i = \mathbf{x}_{i+1} - \mathbf{x}_i$, $\mathbf{y}_i = \mathbf{F}_i - \mathbf{F}_{i+1}$, and $\rho_i = \frac{1}{\mathbf{y}_k \cdot \mathbf{s}_k}$.

$$\mathbf{x}_i = \mathrm{H}_i \mathbf{F}_i \tag{2.58}$$

$$\mathrm{H}_{i+1} = (\mathrm{I} - \rho_i \mathbf{s}_i \mathbf{y}_i^{\perp}) \mathrm{H}_i (\mathrm{I} - \rho_i \mathbf{y}_i \mathbf{s}_i^{\perp}) + \rho_i \mathbf{s}_i \mathbf{s}_i^{\perp} \tag{2.59}$$

NEB calculations in ONETEP can easily have several thousand degrees of freedom. As the number of degrees of freedom increases, the memory cost of representing the approximate Hessian or inverse Hessian matrices can limit the feasibility of a calculation. To mitigate this effect, a limited-memory form of BFGS, termed L-BFGS [104], is appropriate. With this approach the Hessian or inverse Hessian are never explicitly represented in memory. Instead, a fixed number of supporting quantities such as $\mathbf{s}$, $\mathbf{y}$, and ρ from previous updates are stored and used to apply the effect of the inverse Hessian implicitly.

It should be noted that without a well-defined objective function (a result of the NEB forces being non-conservative) quasi-Newton methods such as BFGS are not strictly appropriate for minimizing the NEB chain. However BFGS methods have been observed to effectively iterate NEB paths to a minimum [103]. Rather than testing for convergence against the change in an objective function and the value of its gradient, the magitude of the nudged forces on each bead can be compared against a tolerance, with convergence achieved when all beads in the chain beat this tolerance. Section 4.3.4 discusses optional by-bead energy and displacement convergence criteria.

Fast Inertial Relaxation Engine (FIRE)

FIRE is often introduced with the analogy of a blind skier attempting to navigate a slope, able to steer and brake but only able to determine the direction of the slope locally at the points they visit. The skier sets off in the steepest direction and applies acceleration in the direction of steepest descent, while maintaining motion due to inertia, and braking if they find themselves going uphill. This yields the equation of motion in Equation 2.60 where $\mathbf{v}(t)$ is the velocity at time t, m is the skier's mass, $\mathbf{F}(\mathbf{x})$ is the force at position $\mathbf{x}$, and $\gamma(t)$ is an adaptive quantity that is updated during the minimization. Additionally, if $|\mathbf{F}(\mathbf{x} \cdot \mathbf{v}(t)|$ is negative the velocity is zeroed [106].

$$\dot{\mathbf{v}}(t) = {}^{\mathbf{F}(\mathbf{x})}/_{m} - \gamma(t)\,|\mathbf{v}(t)|\left(\hat{\mathbf{v}}(t) - \hat{\mathbf{F}}(\mathbf{x})\right) \tag{2.60}$$

This equation of motion is discretised with a variable time step to further speed up convergence; the time step is increased while the minimization is accelerating and reduced when the velocity resets. The result is a relatively simple but powerful minimizer that rivals more sophisticated approaches like L-BFGS when optimizing many systems [106].

Doubly-Nudged NEB

An alternative formulation of NEB was proposed by Trygubenko and Wales [108] that reported improved convergence with a non-global L-BFGS update. This approach reintroduces a component of the spring force acting perpendicular to the path, formulated such that it will act to straighten the NEB pathway without corner-cutting the transition state. While this reformulation was found by Sheppard to improve convergence, it did not perform as well as vanilla NEB using GL-BFGS [103].

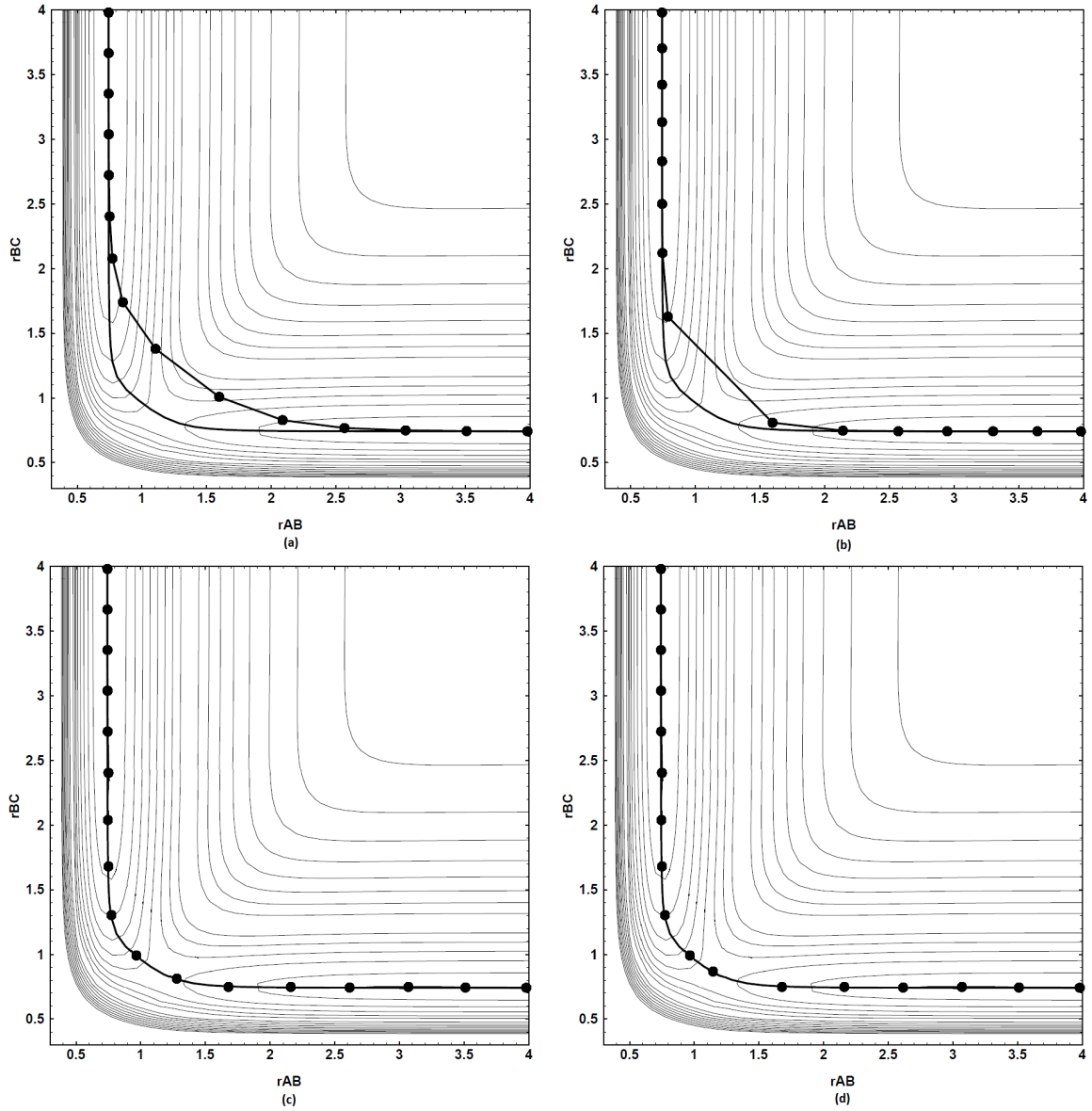

Fig. 2.7 Demonstrations of the elastic band methods for a simple potential energy surface. The potential was generated by a LEPS potential [100] describing the interactions between two free atoms A and C interacting with a fixed atom B. The dots in each diagram are NEB beads on a path generated by (a) the plain elastic band method with a spring constant of 1.0 (b) the plain elastic band method with a spring constant of 0.1 (c) the nudged elastic band method (d) the nudged elastic band method with a climbing image. Note that (c) and (d) are not the result of simulations but are illustrative. Image modified from [98], used also in my MPhil dissertation [101].

2.3.5 String Method

NEB is one in a class of chain-of-states methods designed to calculate minimum energy paths. The string method [109] is an alternative approach that ends up being very similar to NEB. Beads representing points on a continuous path are constructed and the same projection of the real force is used to update them. However, instead of applying a spring force between the beads to keep them spaced out across the path, a manual repositioning of the beads equally along the path is performed at each iteration. A review by Sheppard *et al.* [103] indicated that in practice the two methods provide similar performance.

A simplified formulation of the string method requires no path tangent approximation or force projection. Instead, it fits cubic splines between adjacent beads and redistributes beads along the total spline at the end of each macroiteration. Convergence is measured by the distance each bead moves each step. Tests show [103] that the simplified string method more accurately reproduces the minimum energy path compared to NEB when enough intermediate beads are used. However, the use of too few beads causes the method to become unstable and converge to an oscillating path, or fail to converge at all, whereas NEB will still provide good accuracy and is robust regardless of bead count. For the simple LEPS potential that Sheppard *et al.* used to demonstrate this, the simplified string provided a better estimate of the minimum energy path at 25+ beads, while in the 10-24 bead range it converged to an oscillating path and with fewer than 10 beads it failed to converge. In combination with the climbing image approach, NEB provides a reliable determination of the transition state with minimal bead count, from which the minimum energy path, if required, can be determined with arbitrary accuracy with a steepest descents approach. This makes NEB a stronger candidate for general use.

2.3.6 Transition State Refinement Methods

While NEB provides a robust determination of the minimum energy path, it is expensive to maintain the path while performing a climbing image search for the transition state, and the optimization relies on the approximation that the path tangent aligns with the min-mode direction (the direction aligned with the lowest eigenvalue of the Hessian) of the saddle region. A number of potential energy surface 'walkers' exist that attempt to find saddle points near a starting configuration, without reference to a specific reactant or product. These can be used to refine transition state guesses or, in some

cases, search for transition states from random slight perturbations of a reactant when potential products are unknown. A review of some of these methods was presented by Olsen *et al.* [110].

One of these methods is the 'dimer method' [111]. This method considers a 'dimer' consisting of two configurations that are able to rotate around the center of the line on the potential energy surface connecting them. When rotated in this way until the sum of the energies of the two configurations are minimized the dimer is aligned with the min-mode direction of the potential energy surface. The center of the dimer can then be updated in a similar way to the climbing image in Ci-NEB, where the force components parallel to the min-mode direction are mirrored.

A Lanczos-type approach can be adapted to approximate the lowest eigenpair of the Hessian [112]. A series of tridiagonal matrices are constructed in such a way that their lowest eigenvalues converge to that of the Hessian. A series of orthonormal 'Lanczos vectors' are also generated that can be used to recover the corresponding Hessian eigenvector. Without an exact Hessian, finite differencing is used to query the potential energy landscape along the Lanczos vectors. Lanczos methods require special care to be taken as the Lanczos vectors generated, especially without an exact Hessian, quickly lose orthonormality, destabilizing the series. Once the min-mode direction is identified the optimization step progresses as in the dimer method or Ci-NEB.

Finally, a rational function optimization (RFO) approach uses a modified Newton–Raphson approach to determine update step components along each Hessian eigenvector based on a decomposition of the gradient and the Hessian's eigenvalues [113, 110]. Without an exact Hessian, an approximate Hessian is updated each step, for example with a Bofill [114] scheme. Both the initialization of the Hessian and the selection of update scheme significantly affects the performance of this method [110]. Olsen *et al.* also proposed an extension to the RFO method designed to address the difficulty it has leaving convex regions. Under this 'Hybrid RFO' scheme the RFO update is performed only when the lowest Hessian eigenvalue is negative, otherwise it takes the maximum uphill step in the direction of the lowest eigenpair. This was shown to noticeably improve performance of the RFO method in the systems studied, where the initial configurations were near a minimum of the potential energy surface.

Chapter 3

Ensemble DFT Extensions in ONETEP

3.1 Description of Updates

Proper modelling of large metallic systems with ONETEP required extensions to the existing EDFT functionality [115]. Normal operation of ONETEP constrains the occupancy of each band to 0 or 1 in each spin channel through the idempotency of the density matrix. Because EDFT treats an ensemble of states with a distribution of occupancies, neither the occupancy of a band nor the total occupancy of a spin channel need be an integer. Additionally, the existing implementation of EDFT required spin channel total occupancy to be fixed over the course of a calculation. However it is often convenient to allow the net spin of a system to relax in cases where the net spin that minimizes the system's total energy is not known *a priori*, or where it may evolve such as in a geometry optimization or transition state search.

Fixing the net spin of a system is the same as assigning separate Fermi levels to the two spin channels. Each spin channel's Fermi level μ^σ is determined by a bisection search so that the Fermi-Dirac filling of the energy levels ϵ_i^σ gives the prescribed number of electrons in that spin channel N^σ, shown in Equation 3.1, at a given electronic temperature T. If the net spin is free the system has one global Fermi level μ^{global}, determined with a similar search that fills bands in both spin channels to produce the correct total number of electrons N_{tot}, shown in Equation 3.2.

$$N^\sigma = \sum_i \left[1 + \exp\left(\frac{\epsilon_i^\sigma - \mu^\sigma}{k_{\text{B}}T}\right)\right]^{-1} \tag{3.1}$$

$$N_{\mathrm{tot}} = \sum_{\sigma} \sum_{i} \left[1 + \exp\left(\frac{\epsilon_i^{\sigma} - \mu^{\mathrm{global}}}{k_{\mathrm{B}} T} \right) \right]^{-1} \tag{3.2}$$

The updates made to ONETEP allow a user to specify the net spin (and, in fact, the total electron count) of a system to be non-integer if the `edft` parameter is set to `true`. It is also possible to specify `spin_fix = n`, where `n` is an integer that dictates how the net spin is allowed to evolve. If negative, and by default, the net spin is held fixed at the defined value. Otherwise, the net spin is held fixed for `n` NGWF CG iterations and then allowed to relax.

In geometry optimizations in ONETEP, the calculation is largely reinitialized every several (L-)BFGS steps; resetting every 6 steps is the default value. This is to prevent the buildup of noise in the NGWFs as their cutoff spheres move relative to each other.

EDFT maintains a Fermi level at the finite electronic temperature. As the location of the Fermi level is generally a function of this temperature, care must be taken that properties dependent on the Fermi level are calculated based on the correct 0 K level. For example, determination of the HOMO and LUMO should be done with the correct 0 K filling of the energy levels in the system. When a spin channel is filled with a non-integer number of electrons, the Fermi level lies exactly on the partially filled energy level. By convention in ONETEP this partially filled molecular orbital is labelled the HOMO and the next orbital the LUMO.

3.2 Functionality Benchmarks and Example Usage

3.2.1 Bulk Magnetic Materials

As a demonstration of this functionality, the net spin per atom of cobalt (HCP), iron (BCC), and nickel (FCC) bulk were calculated for a range of bulk supercell sizes. The use of supercells in this case is analogous to the use of a k-point grid in a plane-wave code. NGWFs with a $12\,a_0$ radius were used when the simulation cell was large enough, and extended NGWFs were used for smaller cells. Co was initialized at a net spin of $3\mu_{\mathrm{B}}$ per atom, and Ni and Fe each at $1\mu_{\mathrm{B}}$ per atom. Figure 3.1 illustrates the result, showing that free-spin EDFT can reproduce experimentally determined values from Reference [116], but that good k-point sampling or the use of supercells is required to converge this quantity.

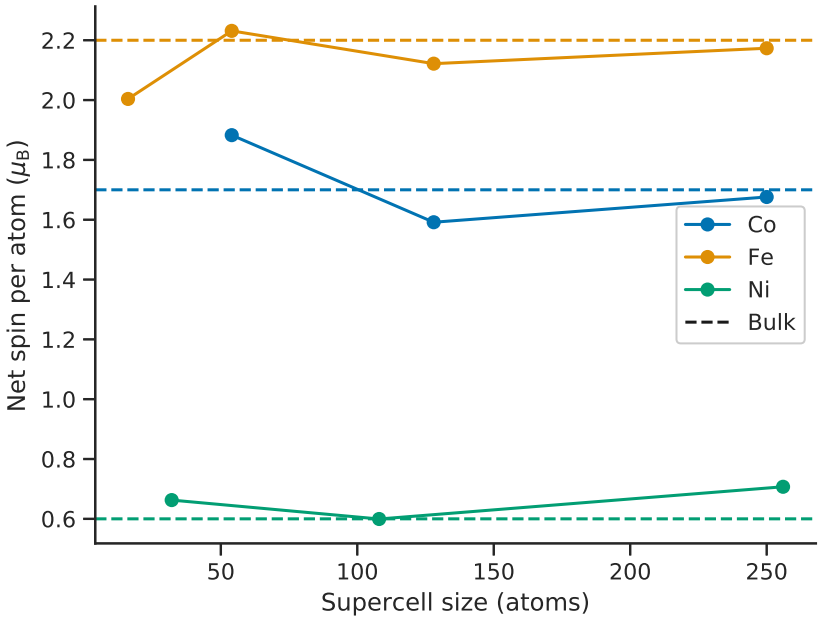

Fig. 3.1 Calculated net spin per atom values of bulk Co, Fe, and Ni for a range of supercells, compared to the experimentally determined bulk value reported in Reference [116].

3.2.2 Cobalt Clusters

Several high-symmetry FCC and HCP cobalt particles ranging in size from 1 atom to 153 atoms were geometry optimized with free-spin EDFT enabled. The particles were generated by adding layers of HCP or FCC nearest neighbours with a nearest neighbour distance of 2.5071 Å to a smaller cluster, starting with a single atom. These are also referred to as the first few of the 'magic number' clusters for these symmetries. In each case, the net spin was initially set to $3\mu_B$ times the number of cobalt atoms in the cluster, and was held fixed for typically 5 NGWF CG steps before allowing spin relaxation. This allowed an exploration of the effect of particle size on the net spin of clusters without either prior knowledge or a multi-calculation search over spin states. It also allows the spin state search and geometry optimization to be performed simultaneously.

Figure 3.2 shows the net spin per atom of these clusters, as well as a line indicating the net spin per atom of bulk Co, calculated both experimentally by Billas *et. al.* and in a ONETEP calculation on a 250-atom HCP bulk cell [116]. This shows a clear trend towards bulk-like spin as the particle size increases. To better understand this

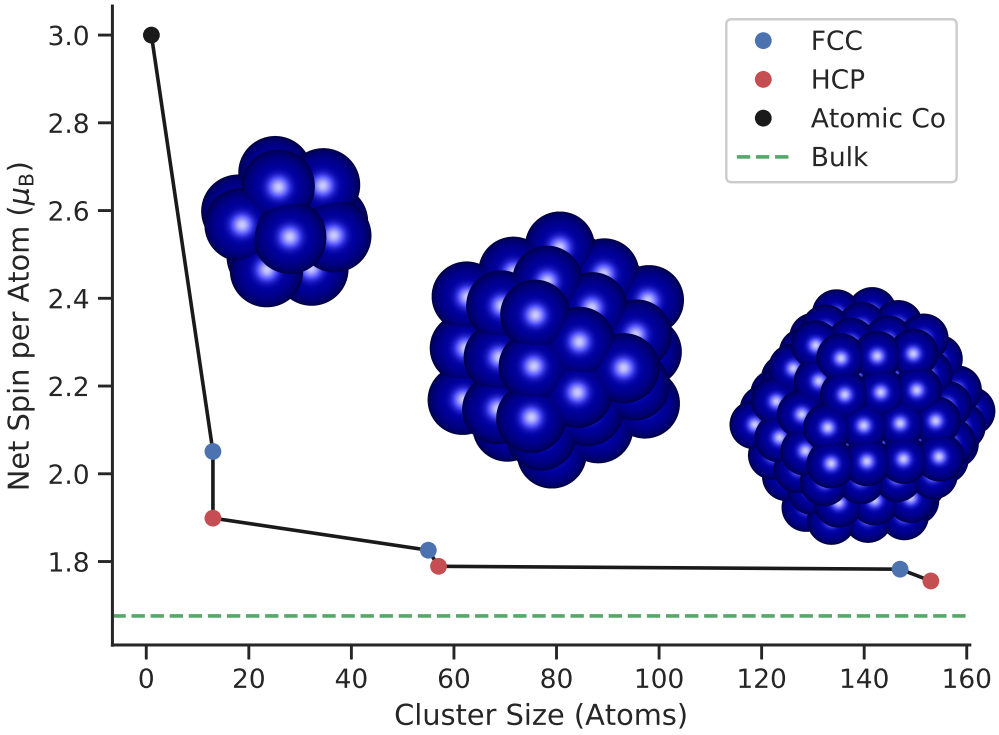

Fig. 3.2 Net spin per atom of HCP and FCC Co 'magic number' clusters of increasing size. Inset are, from left to right, the 13-atom HCP cluster, 55-atom FCC cluster, and 153-atom HCP cluster. A horizontal marker is added at the bulk value for HCP cobalt, determined from a ONETEP calculation.

behaviour, a Mulliken spin population partitioning [117] was performed to assign net spins to each atom. Figure 3.3 illustrates the result both on the surface of the 57-atom HCP cluster and on a cutaway. It is clear that surface atoms are assigned a higher net spin than core atoms and that the trend in net spin towards bulk can be described by a decreasing surface area to volume ratio of larger clusters. Figure 3.4 expands on this by plotting the distribution of the Mulliken spin of an atom against its nearest neighbor count, defined using a 2.6 Å cutoff, across all atoms in all clusters. The different distributions of net spins especially for the corner atoms with 5 and 6 nearest neighbors as a result of different geometric environments may help to illustrate the observed difference in net spin between similarly sized HCP and FCC clusters in Figure 3.2. It should be noted that the use of Mulliken partitioning here is not intended to be quantitative but is used only to demonstrate trends.

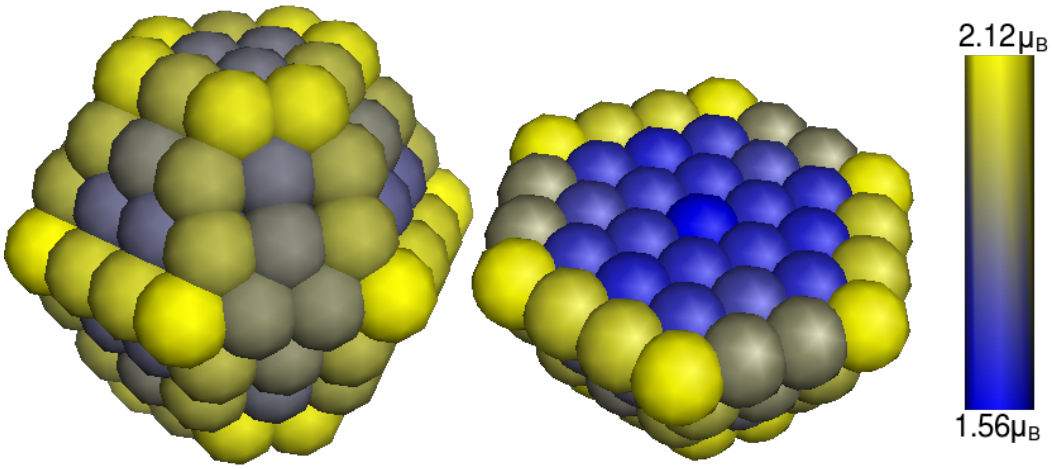

Fig. 3.3 Coloured representation of the Mulliken-partitioned spin population of the atoms in a 153-atom HCP Co cluster, showing both an external and cutout view. This demonstrates that the net magnetic moment per atom of a cluster is related to its surface area to volume ratio.

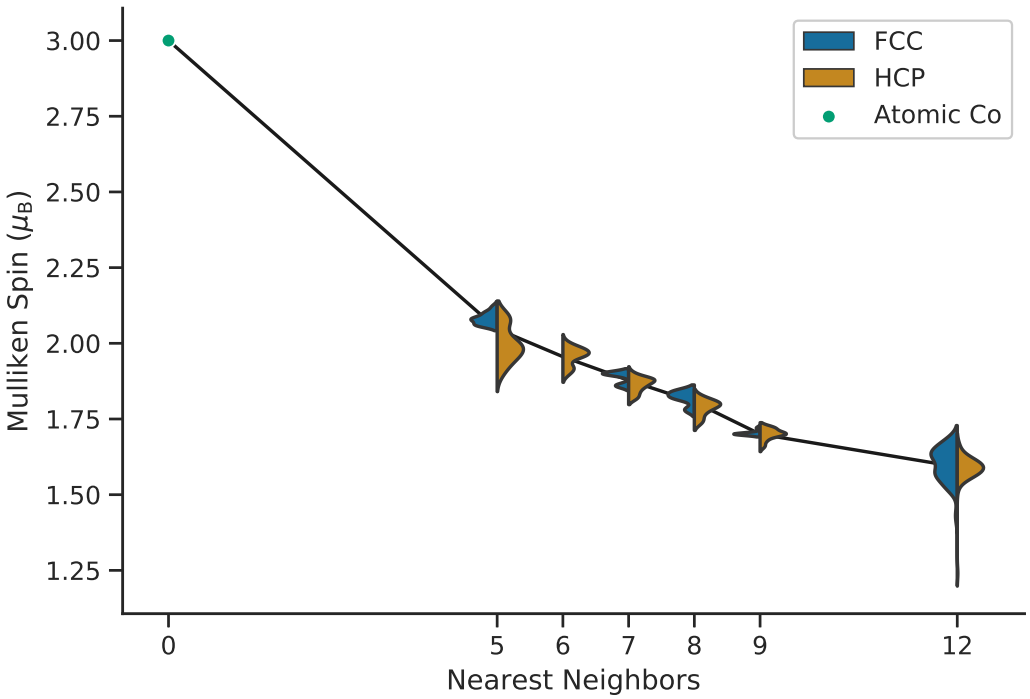

Fig. 3.4 Violin plot showing the distributions of Mulliken-partitioned spin of atoms in several cobalt clusters ranging from size 1–153 with different nearest neighbour counts. Nearest neighbours are taken to be within 2.6 Å. The background line connects the mean values of each group.

3.3 Further Work

As mentioned in Chapter 1, ONETEP imposes a restriction that both spin channels in a spin-polarized calculation use the same NGWFs, and instead only produces a spin-polarized density kernel and, in EDFT calculations, a spin-polarized Hamiltonian. The theory does not require this restriction, and current work is being done in the ONETEP development community to understand if spin-polarized NGWFs are required for a more accurate treatment of spin-polarized systems. Spin-polarized NGWFs are currently under development along with several other extensions to the current implementation of LS-DFT theory.

Another promising development is the AQuA-FOE method [118] recently developed and added to ONETEP by Aarons and the Skylaris group, which uses a Fermi operator expansion technique to avoid the cubic-scaling cost of EDFT calculations. This has been used for calculations on nanoparticles with over 10,000 atoms. With these extensions, predictive calculations on ferromagnetic particles of similar sizes are now feasible with ONETEP. At the time of writing this method only supports fixed spin, interger net spin systems, but a similar treatment to that described in this section could be applied directly to these methods to enable free-spin or non-integer net spin simulations.

3.3.1 ONETEP at Fixed Electrochemical Potential

The extension of EDFT runs to non-integer charge opens up the possibility of calculations with a variable total electron count. In particular, a control on electron chemical potential (electrochemical potential) is a highly useful analogue to a control on the number of electrons. The implementation details of this control depends somewhat on the application as care must be made to ensure the Fermi level selected is referenced to the correct zero of energy. For example, this approach could be used to perform defect calculations in a very straightforward way: A normal calculation is run on the perfect cell, and then a calculation on the defective cell is performed fixed at the Fermi level μ_{perfect} of the perfect cell. This simulates a defect cell in contact with an infinite bath of electrons in the perfect environment. By equating the Fermi energies of the two calculations the defect energy could be obtained trivially. However, an issue arises, in that removing an atom or otherwise creating a defective cell is likely to change the reference value for energies in the calculation, which in ONETEP is the system of bare pseudo-atoms with explicit electrons removed to infinity. Fermi energies are therefore not comparable between the defective and perfect cells. This could potentially

be addressed by aligning semi-core states under the approximation that they do not significantly change in energy when the chemistry of the system changes.

Chapter 4

Transition State Searching in ONETEP with NEB

4.1 Motivation and Context

The need for transition state searching and optimization tools in packages like ONETEP [57, 58] has been expressed in the linear-scaling DFT community [119]. ONETEP excels in fields like quantum biochemistry and surface chemistry where a predictive and highly accurate theory is required but system sizes are necessarily large, or they may be aperiodic in at least one direction. Previously, however, it lacked the ability to predictively explore chemistry in these classes of systems without a robust transition state searching method.

Currently external tools can be used to perform NEB calculations while using ONETEP as an energy and force calculator. The principal example of these tools is the Atomic Simulation Environment [120], a Python module designed to assist in the creation, running, and visualization of atomistic simulations. This approach allows tools to be built in a way that can be shared between energy and force calculators and allows calculations to be designed to be easily transferred and reproduced between packages. However, it does not have access to internal control over the ONETEP simulation, and a scalable setup requires configuring an MPI-enabled Python such as `gpaw-python` [121]. An internal solution simplifies distribution and use, and allows greater control over the simulation in its implementation. Commercial users usually access ONETEP through Materials Studio, distributed by Dassault Systèmes, which would ideally be able to expose an internal implementation.

This implementation of NEB in ONETEP should be considered the first tool in a suite of transition state tools that are necessary for studying chemistry in large-scale systems. One approach already being adopted in large scale studies using ONETEP for NEB is to perform the calculation on a couple-hundred-atom scale minimal model to identify the transition state, then move the intermediate states into the full system as an initial guess path in order to reduce the overall cost. A potentially more powerful approach would involve the use of saddle-point searching methods such as the dimer method, which attempts to approximate the negative-curvature direction of the potential energy surface and walk towards saddle-points. This could be used to validate and refine intermediates located in minimal models without the need to maintain a minimum energy path estimate for the full system. Additionally, robust and efficient implementations of synchronous transit methods [95, 96] could be used to provide inexpensive guess intermediates and a quadratic path to place beads on, potentially improving the initial guess path over a simple reactant-to-product linear interpolation.

4.2 Image-Parallel Running Mode

There are two non-intrusive approaches to implementing a NEB macroiteration in ONETEP. The first is to implement a new task that calculates the energy and force on each image sequentially, then finds new atomic positions and cycles back through the images until convergence. This requires either storage or regeneration of model data between visits to a given image, which incurs either a storage or computational cost. More importantly, the processor count for the simulation is limited by the parallelisability of a single calculation, limiting throughput due to the increase in calculation wall-time by a factor on the order of the number of NEB images compared to a geometry method. The second approach, mentioned above, is to use an external driving script to initialize several copies of ONETEP with the `Singlepoint` task to calculate the total energy and atomic forces of each NEB image, then read the output files and perform atomic position update calculations externally and re-initialize ONETEP with a new set of input files. This approach ensures scalability, as there is no hard limit on the processor count, but requires many sequential initializations of ONETEP with external maintenance, and uses disk operations for transferring information, making poor use of the underlying parallel architecture. It also requires the creation and

Fig. 4.1 Diagram of the three relevant MPI communicators in the image-parallel model for a ONETEP simulation containing 12 MPI processes divided into four ONETEP images.

maintenance of an external script which increases usage and distribution complexity and a scalable approach requires an MPI-compatible or otherwise distributed driver.

An internal driver approach provides the scalability of an external driver while also providing access to internal memory and parallel architecture. It also allows the functionality to be exposed in a simple and 'ONETEP-idiomatic' way. With this in mind, a new running mode termed 'image-parallel' has been introduced to ONETEP which allows many distinct simulations to be running in the same parallel environment. Figure 4.1 illustrates the three main MPI communicators used. The first is the `mpi_comm_world` of the simulation, containing all MPI processes. The world communicator is divided at runtime into a user-specified number of equally or manually sized groups or 'images'. This is controlled by the `num_images` parameter in the ONETEP input file. Each of these groups are initialized as their own simulation, with distributed matrix storage and parallel operations limited within each image. Their individual root processes have the same function as the root process of a typical ONETEP simulation including I/O and simulation management. Each image's root process is added to a communicator of root processes, called `pub_imroots_comm`, which allows each separate ONETEP simulation to communicate with the others for collective task management.

NEB was implemented using this running mode. Each NEB bead is assigned to one ONETEP image for energy and force calculations, with the root process on the `pub_imroots_comm` communicator handling distribution and collection of data, convergence checking, and atomic position update calculations for each macroiteration. One downside of this approach is that a relatively large system with a relatively small available processor count may force each image to be inefficiently under-parallelised

in order to reach the desired path resolution. Another downside of applying this approach is that NEB images that undergo relatively small position changes between macroiterations, such as those close to the endpoints, are expected be able to more effectively reuse information from the previous iteration and so will generally converge faster, wasting cycles until the other images have finished. While some dead-cycle cost cannot be avoided in general, systematic causes such as this one can be minimized. Potential future approaches to addressing these issues are discussed in Section 4.7.

4.3 NEB Implementation Details

4.3.1 Setting up a NEB Calculation in ONETEP

A NEB run in ONETEP requires the `task` to be set to `transitionstatesearch` and the `tssearch_method` to be `NEB`. It also requires the specification of a number of ONETEP images equal to the desired number of NEB beads, as described above. Reactant and product energies can be specified in three ways: they can be explicitly included in the input file, they can be quickly determined from previous results by specifying input files containing the NGWFs and density kernel (and/or Hamiltonian in the case of EDFT results), or they can be calculated from scratch at runtime. These options offer flexibility to the user in how best to set up a NEB calculation based on the results and simulation outputs they have available. As an example, it may be appropriate in some case to define the reactant energy of a multi-species reactant as if the constituent species start infinitely apart, by summing the total energies obtained from simulations of the constituent species. This energy can be used while the actual reactant structure has each component a finite distance apart in the same cell to get a better representation of the forward reaction barrier from the ONETEP report.

The initial path can be specified in a number of ways. The reactant and product structures must be specified, with the reactant taking up the normal positions block and the product taking a similar block ending in `_product`. In the case that only these structures are specified the path beads will be set by linear interpolation between them. An optional guess intermediate structure can be specified using the positions block ending in `_intermediate`. In this case the path will be specified by piecewise linear interpolation, with one bead placed exactly at the guessed intermediate. The intermediate bead is selected such that the beads are as close to equally spaced along

the path as possible. Finally, the placement of all beads can be read in, either directly from `.xyz` files or from the continuation file of an incomplete NEB calculation.

The climbing image can be enabled with the `neb_ci_delay` keyword, which specifies the number of NEB macroiterations after which the functionality will be enabled. A negative number disables climbing image entirely. Because the climbing image approach is appropriate only when the bead is near a saddle point, the path should be relatively well converged before enabling this functionality. Setting this value to a very large number has the effect of enabling climbing image once the path has met convergence criteria.

Because chemical reactions often involve band crossing, the use of ensemble DFT is recommended in NEB runs even if the system being simulated is not metallic to prevent convergence issues in intermediate structures that may have very small band gaps.

Additional input parameters and usage information can be found in the documentation at `onetep.org`. This functionality was designed so that it can be used as simply as possible; specifying the `task`, method, and reactant and product structures is all that is required in an otherwise familiar ONETEP input file.

4.3.2 NEB Macroiteration

The NEB macroiteration in ONETEP is handled by a driver managed by the root processors on each image. It starts with an energy and force calculation on each bead, followed by a calculation of the path tangent and nudged forces. Tangents are calculated using the upwinding tangent approach described in Section 2.3.2. A minimizer step is applied, either by the image root processors or on the global root process for the entire chain depending on the minimizer used. The new bead positions are then distributed to their assigned image. To calculate the nudged force on a particular bead the positions and energies of the two neighboring beads must be known, so the path must synchronize between energy and raw force calculation and the calculation of the nudged forces.

4.3.3 Available Minimizers

Several nonlinear minimizers are suitable for use with NEB. Sheppard *et al.* [103] performed a comparison of a selection of first-order and quasi-Newton methods that highlighted several promising candidates. Currently, FIRE [106], Quick-Min [105], and GL-BFGS [103] are implemented and can be selected by specifying `neb_update_method`

as `FIRE`, `QUICKMIN`, or `GLBFGS`. GL-BFGS is used by default. First order methods such as FIRE do not require any communication between images, whereas GL-BFGS requires a gathering of bead forces and scatter of update vectors each iteration. This communication is typically a small cost compared to the lockstep cost in waiting for all energy and force calculations to complete.

The choice of parameters for FIRE largely follow the recommendations of the source paper [106]. These are $N_{\min} = 5$; $f_{\text{inc}} = 1.1$; $f_{\text{dec}} = 0.5$; $\alpha_{\text{start}} = 0.1$; $f_\alpha = 0.99$. $\Delta t_{\max}$ is set to 5 fs.

In all cases, the step length is restricted on each bead individually. This prevents large forces from displacing any single image too much, reducing discontinuities in the NEB chain and safeguarding the minimization from taking very large steps into problematic geometries. If the largest ionic displacement $\mathrm{d}\mathbf{R}_{\max}$ is larger than $0.5\,a_0$, all ionic displacements in that bead are scaled by ${}^{0.5a_0}/_{|\mathrm{d}\mathbf{R}_{\max}|}$ to retain the direction of the update. This is an existing restriction on geometry optimization in ONETEP, and its impact on NEB's stability and performance needs investigation.

Because the potential energy surface changes when the climbing image is enabled for a particular bead, reusing GL-BFGS history from before it was enabled would be inappropriate. Additionally, the inclusion of a climbing image significantly affects the chain's Hessian. Tests involving the use of GL-BFGS with a climbing image resulted in poor convergence, as did tests involving using a separate minimizer only for the climbing bead. As a result, if climbing image is enabled the chain update method is automatically changed to FIRE.

4.3.4 Convergence Criteria

By default the NEB chain is converged if the largest nudged force on any ion across the chain is less than `tssearch_force_tol`. This tolerance is $5 \times 10^{-3}\,E_{\text{h}}\,{a_0}^{-1}$ by default. Optionally, energy changes and ionic displacements in a macroiteration can be added as convergence parameters similar to typical geometry optimizers. However, these values are not necessarily converged for a converged path as bead movement along the minimum energy path can cause displacements and energy shifts without changing the underlying path. The climbing image bead is unlike the other beads in that it does attempt to sample one point on the path. For this reason, the energy change and displacement convergence critera are again appropriate and are enabled for this image regardless of the convergence criteria used for the rest of the beads. Their default convergence values are $1 \times 10^{-5}\,E_{\text{h}}$ and $1 \times 10^{-2}\,a_0$ respectively.

4.4 Oxirane Ring Opening

A simple chemical reaction that can be used as a test case of the NEB functionality in ONETEP is the reaction betwen water and oxirane (ethylene oxide) to form ethylene glycol, shown in Equation 4.1.

$$(CH_2CH_2)O + H_2O \longrightarrow HO{-}CH_2CH_2{-}OH \tag{4.1}$$

The reactant and product of this reaction were optimized using ONETEP and added to a transition state search task. An intermediate state was found during the ring opening, similar to the product but rotated around the C–C bond into a 'cis' configuration. Two separate NEB calculations were performed, with the first breaking the oxirane ring and splitting the water molecule and the second simply rotating the carbon–carbon bond. Because a simple linear interpolation of the second pathway would result in configurations where the rotating oxygen, hydrogen, and carbon atoms are very close, a partially rotated intermediate was created manually. This illustrates one of the uses of this functionality as a quick control over the initial path guess when a linear interpolation is insufficient.

Figure 4.2 shows the reaction pathways for both parts of this reaction. In both cases, the path was allowed to fully converge before climbing image functionality was automatically enabled and the calculation was re-converged. In this way the transition states were accurately sampled. Inset in both figures are the reactant, product, and intermediate structures. It is found that the forward reaction barrier to oxirane ring opening is 1.98 eV. The very small minimum near path coordinate 0.6 in Figure 4.2(b) may be an artifact of the convergence criteria.

The first part of the oxirane ring opening reaction was used to validate the internal NEB implementation in ONETEP. Results of a converged 8-image climbing image run of the reaction was compared to an equivalent setup in ASE driving ONETEP, with parameters like spring constant set identically where possible. The energies of the transition state structures found in these two approaches agreed to within 5×10^{-3} eV, with this difference potentially being reduced by further iterations.

4.4.1 Comparison of Minimizers

Figure 4.3 compares the NEB convergence of the reaction pathway for the first part of the oxirane ring opening reaction. The minimizers compared include the new FIRE,

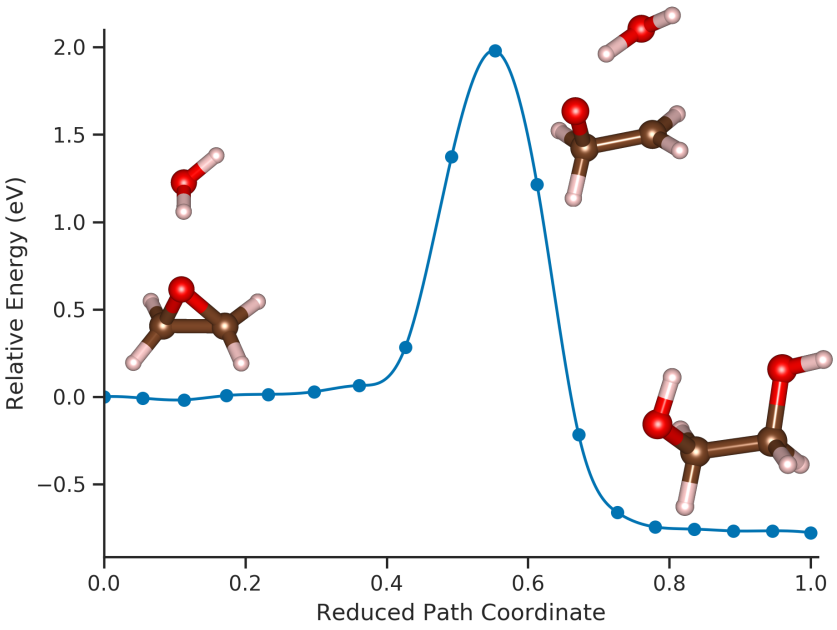

(a) Oxirane and Water to Intermediate

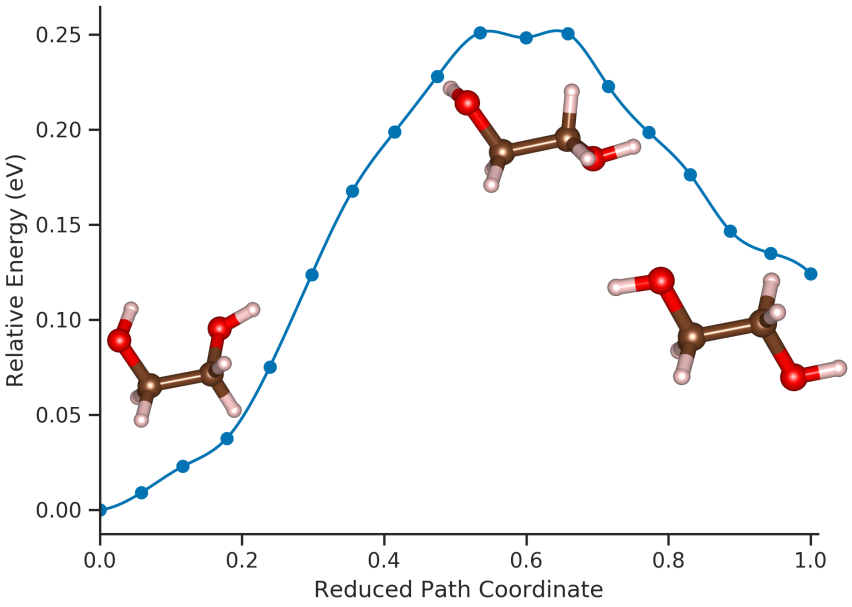

(b) Intermediate to Ethylene Glycol

Fig. 4.2 NEB reaction pathways of (a) oxirane and water reacting to form an intermediate structure and (b) the C−C bond and a O−H bond in the intermediate rotating to form the ethylene glycol product. Cubic splines are added between images on the path. Reactant, product, and intermediate structures are inset.

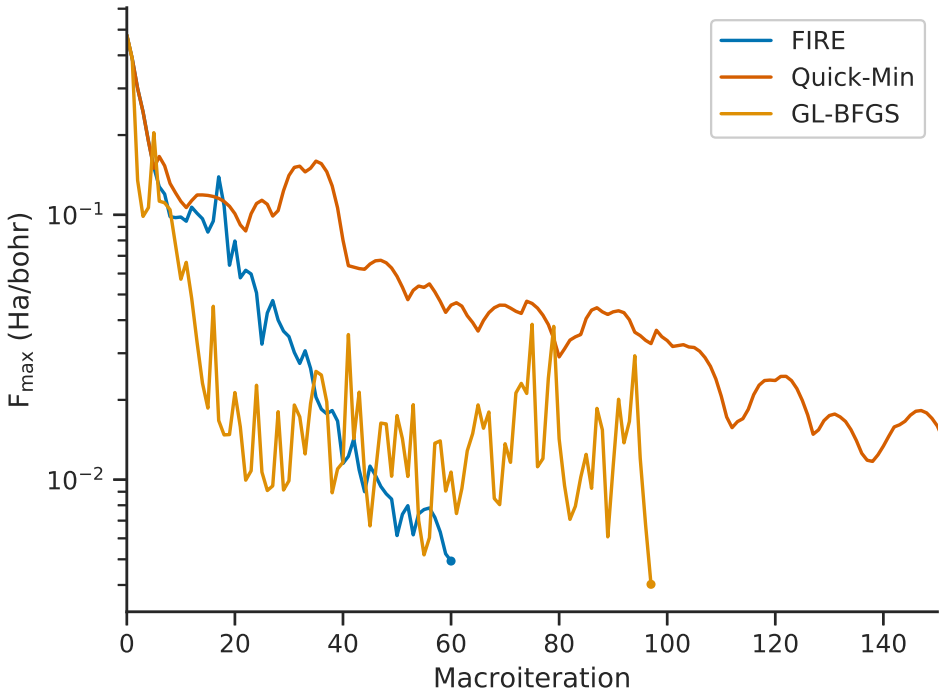

Fig. 4.3 Comparison of NEB minimizers available in ONETEP. Both FIRE and GL-BFGS converge to less than $5 \times 10^{-3}\, E_\mathrm{h}\, {a_0}^{-1}$ on any ion quickly, taking 61 and 98 macroiterations respectively. Quick-Min takes significantly longer at 340 iteration.

Quick-Min, and GL-BFGS minimizers. Of these, FIRE and GL-BFGS are clearly preferred approaches as they converge quickly to the force tolerance of $5 \times 10^{-3}\, E_\mathrm{h}\, {a_0}^{-1}$ on any ion. A minimizer that utilizes ONETEP's geometry optimizer to perform a non-global L-BFGS update on each bead was also investigated as there are reportedly conflicting opinions on its stability and applicability for NEB [103]. The minimizer as implemented was found to be unstable when applied for this system and did not reach convergence within several hundred iterations. Its fundamental shortcoming is its inability to represent the Hessian of the full NEB chain, instead only representing block-diagonal elements within each NEB bead.

4.4.2 Parameter Choices

A number of quantities in the NEB calculation can be considered as free parameters and are exposed to the user for input. These include primarily the number of NEB beads, the spring constant used for the chain, and the climbing image delay. The effects

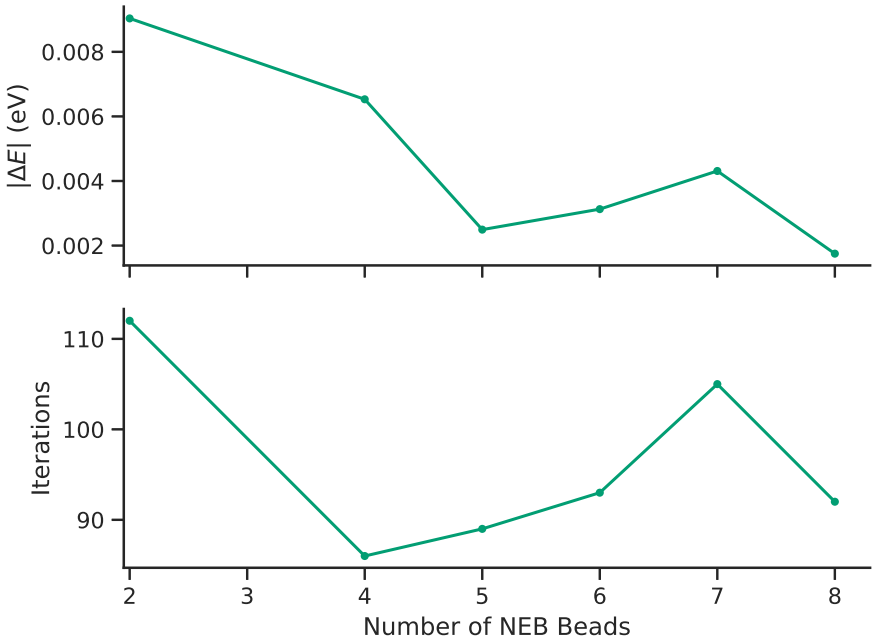

Fig. 4.4 Magnitude of transition state energy deviation from a 16-image run and total number of iterations required to converge a NEB calculation of the reaction illustrated in Figure 4.2a with varying image counts. Notably the three-bead calculation did not converge.

of these parameters on the accuracy and performance of NEB has been examined for the first part of the above reaction. In all cases the FIRE optimizer was used.

The number of NEB beads used in the calculation appear to have little effect on the accuracy of the result. Figure 4.4 shows the difference in barrier found between a 16-bead run and runs with 2 to 8 beads. It also shows the number of iterations it took to converge the path from an initial linear interpolation, with climbing image enabled only after the path was converged without it. The 3-bead calculation did not converge, and remained unstable after adjusting optimization parameters such as the spring constant. This indicates that, while it is possible to calculate accurate barriers for simple transitions with very few images, care must be taken to ensure the calculation remains stable.

The climbing image delay can have an effect on the resultant path and barrier. In this case, the path took 40 iterations to converge without a climbing image. Enabling the climbing image before this point may, but does not necessarily, reduce the total iteration count. Additionally it can affect the final barrier energy. Figure 4.5 shows

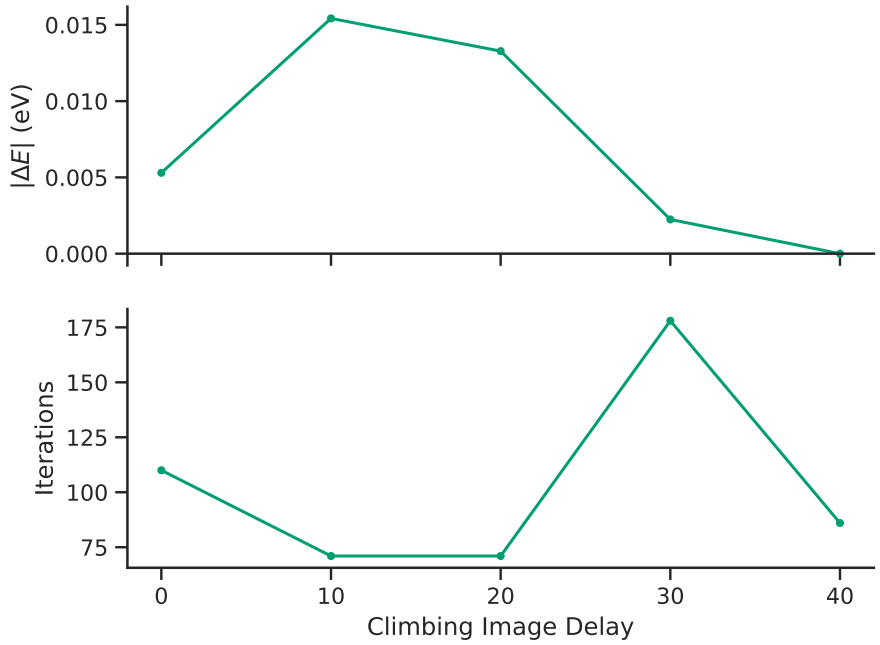

Fig. 4.5 Magnitude of transition state energy deviation and total number of iterations taken to converge a 4-bead NEB calculation of the reaction in Figure 4.2a with different climbing image delays, where the calculation took 40 iterations to converge without climbing image.

these effects for a 4-bead path, with the barriers reported relative to the 4-image path that enabled climbing image after converging without it.

As outlined in the theory, the spring constant appears to have little effect on the optimization of the path up to some limit after which the optimization becomes unstable. Figure 4.6 shows the accuracy and performance of the optimization with a range of spring constants for a 4-bead path. The barriers are only slightly affected by the choice of spring constant but above some threshold the performance is reduced dramatically, and eventually the optimization fails completely. The optimization failed with a spring constant of $1\,E_\mathrm{h}\,{a_0}^{-2}$

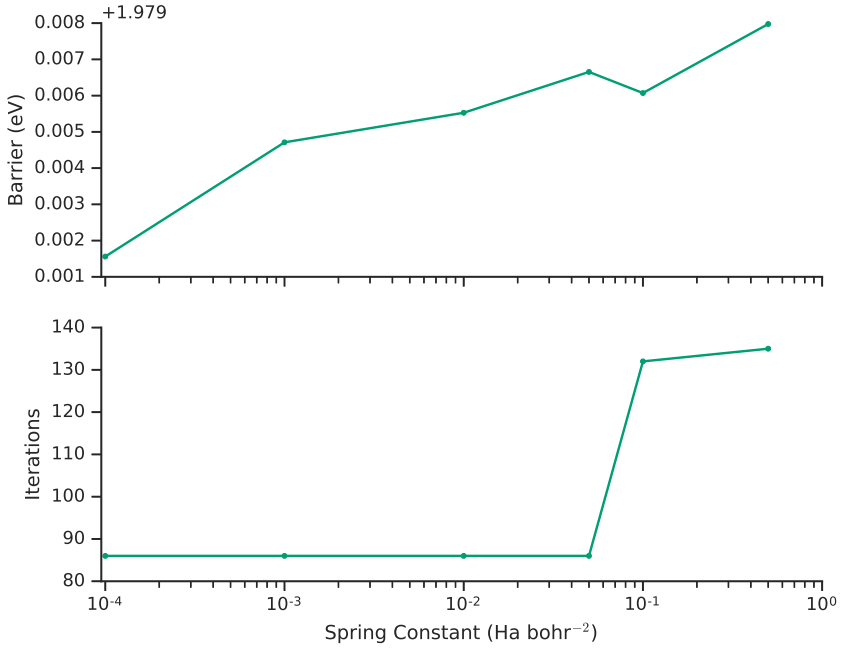

Fig. 4.6 Absolute transition state energies and total number of iterations taken to converge a 4-bead NEB calculation of the reaction in Figure 4.2a as the spring constant of the spring interactions between the beads is varied.

4.5 A Tangent: NEB Minimizers Adapted for Geometry Optimization

The minimizers implemented for NEB are general methods for geometry optimization. ONETEP typically uses a BFGS or L-BFGS minimizer with a line search to perform geometry optimizations. NEB's searchless L-BFGS in particular is potentially a powerful alternative that may reduce the total number of energy and force calculations required to optimize a particular structure. To this end, these geometry methods were adapted for use in general geometry optimization methods.

Figure 4.7a illustrates the geometry optimization of a stretched oxirane molecule using ONETEP's default minimizer as well as the new searchless L-BFGS and FIRE optimizers. Figure 4.7b shows the performance of the same optimizers on a sumatriptan molecule, which is a migraine treatment drug [122]. The searchless L-BFGS outperformed the existing implementation in the optimization of the oxirane molecule. In the case of the Sumatriptan molecule, both new minimizers take longer to converge but find a slightly better final structure. They pass the existing optimizer's final energy at the

iterations marked with vertical dashed lines in Figure 4.7b. FIRE does not generally appear to perform as well as the other optimizers, though a re-parameterization may yield different results.

Both implementations of L-BFGS were also tested on the optimization on a CO molecule adsorbed to a CO_{13} cluster. Figure 4.8 shows that the new searchless L-BFGS outperforms the existing optimizer in terms of the number of energy and force calculations performed. This increased performance may be due to a reduced cost of local gradients producing bad search directions, or may be cause to examine the line search procedure in ONETEP, or in a worst case its energy and force consistency.

In addition to potential performance advantages, the new optimizer is built to be flexible and extensible. A geometry optimizer state struct has been created, and each geometry method is a function that takes in the state and force information, and returns a geometry update step while updating the optimizer state struct. In this way, the optimizer can be passed around the code, and can used natively with any kind of new geometry method including alternative transition state methods. The optimization method can be changed by simply applying a different function to the state, and several different optimizer states can be maintained and evolved independently.

An important note is that while the number of energy and force calculations is an intuitive and common comparison between optimizers, in this case it must be taken with a caveat about the costs of energy and force calculations in practice. ONETEP typically reuses the previous step's NGWFs and density kernel but resets them periodically. Trial steps in the line search are not counted towards this reset count, so the default optimizer may use fewer NGWF CG steps per energy and force calculations on average. However, the searchless L-BFGS still typically performs better when making the more applicable comparison between total NGWF CG counts.

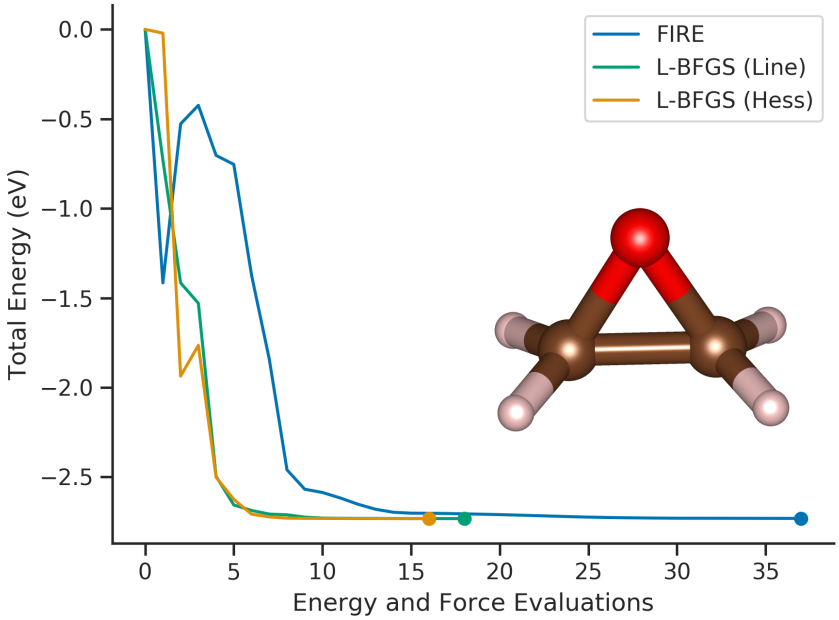

(a) Oxirane molecule

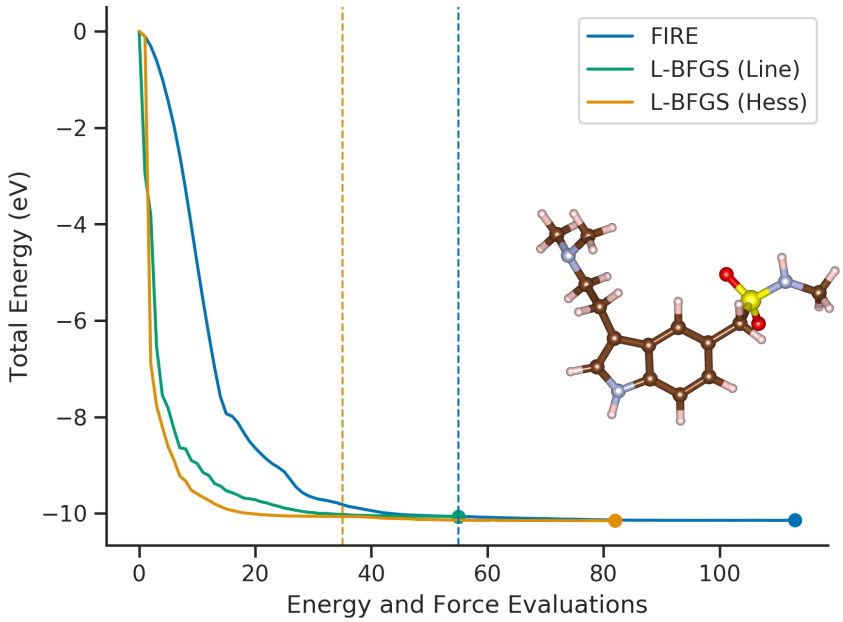

(b) Sumatriptan molecule

Fig. 4.7 The progression of total energy and force evaluations in geometry optimizations on two systems using three different optimizers. L-BFGS is implemented either with a line search ('L-BFGS (Line)') or applying the Hessian to get the update step ('L-BFGS (Hess)'). For 'L-BFGS (Line)', the default method in ONETEP, several of these energy and force evaluations are used on trial steps in the line search. Energies are relative to the unoptimized structure's starting energy. In (b) the new minimizers found a lower minimum than the L-BFGS (Line), and the iterations at which they beat its minimum are marked with dashed lines.

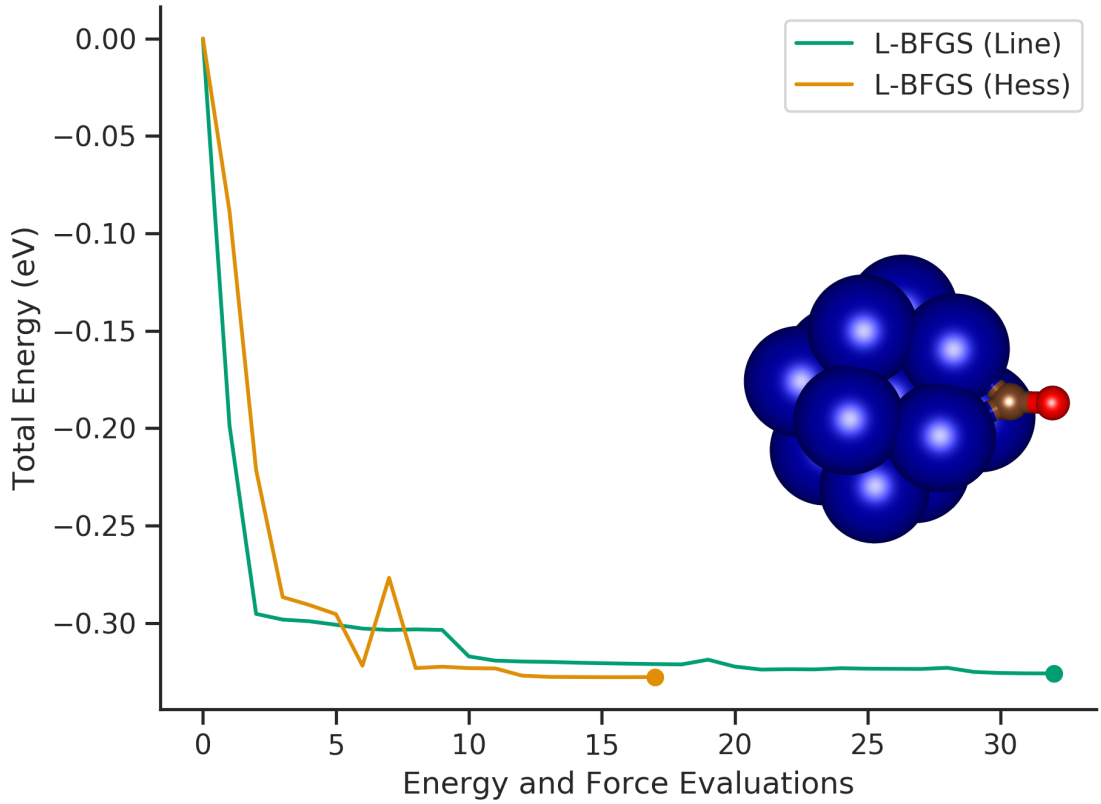

Fig. 4.8 Comparison of L-BFGS with and without a line search in optimizing a CO molecule adsorbed on a Co_{13} cluster.

4.6 Further Transition State Tools in ONETEP

As discussed, NEB is one of many tools appropriate for a complete approach to robust large-scale transition state searching. Several methods exist to search for nearby transition states that make no reference to reactants or products nor require the costly maintenance of an approximation to an entire minimum energy path. These techniques can be used to refine approximate transition states found with non-climbing NEB, or found on a smaller model subsystem of a much larger structure such as the local protein environment of a large metalloprotein. A few of these methods were briefly discussed in Section 2.3.6. One such approach, the dimer method, has been recently developed for use in ONETEP.

4.6.1 The Dimer Method

The dimer method utilizes part of the hyperdynamics approach developed by Voter [123], which performed a dimer rotation to locate the direction corresponding to the lowest eigenvalue of the Hessian using only first derivatives of the potential energy surface. The central concept is that, for a dimer with a fixed center and dimer separation, the target orientation is that which minimizes the sum of the dimer point energies. This is based on a numerical approximation to the second derivative of the potential energy surface and the quadratic approximation implied by Hessian search methods, and is outlined in Equation 4.2 where $V(\mathbf{r})$ is the total energy at a configuration $\mathbf{r}$, $\epsilon(\mathbf{s})$ is the minimal eigenvalue approximation along the dimer orientation $\mathbf{s}$, and η is a small number representing the dimer separation [123].

$$\epsilon(\mathbf{s}) = \left[V(\mathbf{r}+\eta\mathbf{s}) + V(\mathbf{r}-\eta\mathbf{s}) - 2V(\mathbf{r})\right]/\eta^2 \tag{4.2}$$

From an initial guess orientation $\hat{\mathbf{N}}$, a scaled rotational force on the dimer is calculated as $\mathbf{F}_{\text{rot}} = (\mathbf{F}_1^{\perp} - \mathbf{F}_2^{\perp})/\delta x_{\text{D}}$ where $2\delta x_{\text{D}}$ is the dimer separation and $\mathbf{F}_i^{\perp} = \mathbf{F}_i - (\mathbf{F}_i \cdot \hat{\mathbf{N}})\hat{\mathbf{N}}$ are components of the force calculated on the two points of the dimer. This is also calculated at a small finite rotation $\delta\theta$ in the plane defined by the force and dimer orientation vectors to obtain an approximation of the force derivative $F' = (\mathbf{F}^*_{\text{rot}} \cdot \hat{\mathbf{F}}^*_{\text{rot}} - \mathbf{F}_{\text{rot}} \cdot \hat{\mathbf{F}}_{\text{rot}})/\delta\theta$, where starred quantities are those of the rotated dimer. By applying a quadratic approximation of the potential energy surface a target rotation can be calculated as in Equation 4.3. [111] This can be done repeatedly until the

rotational force is below some tolerance.

$$\Delta\theta = -\frac{1}{2}\arctan\left(\frac{2F}{F'}\right) \tag{4.3}$$

Once this orientation has been determined the center-point of the dimer can be moved in a modified potential energy surface, where the force component along the min-mode direction is flipped, as in Equation 4.4. This is very similar to the motion of the climbing image in a Ci-NEB calculation, where the approximation to the path tangent takes the place of the approximate min-mode direction.

$$\mathbf{F}_{\mathrm{m}} = \mathbf{F} - 2(\mathbf{F}\cdot\hat{\mathbf{N}})\hat{\mathbf{N}} \tag{4.4}$$

4.6.2 The Dimer Method in ONETEP

A dimer method has been recently implemented in ONETEP using image comms. A ONETEP image is responsible for energy and force calculations at each of the two dimer points during the rotation phase. One image collects the energy and force of each dimer point, calculates new dimer orientations for the trial and rotation steps, and checks convergence criteria. The other image only receives this information and performs energy and force calculations at its dimer point.

The dimer method is divided into rotation steps where a min-mode direction is determined, and translation steps where the dimer centrepoint is moved towards a saddle point. The initial min-mode direction used by the first rotation step can be either randomly initialized or can be read in from the continuation file of a NEB bead, in which case it will use the tangent approximation of the bead provided. In subsequent rotations it will re-use the min-mode from the previous rotation step. Olsen *et al.* [110] determined sensible default parameters for the dimer method, as well as a few other transition state methods. Some of these parameters are applied as defaults to control the convergence criteria of the dimer rotation. They note that a cutoff on the number of rotation steps allowed can provide a tradeoff between converging the min-mode direction and taking a reasonable step towards the saddle point. This is optional in the current implementation of the dimer method in ONETEP.

The dimer is translated using the new geometry optimizer methods discussed in Section 4.5, based on an approximation of the force on the dimer's centrepoint given in

Equation 4.5. The centrepoint energy can also be approximated by Equation 4.6 [111].

$$\mathbf{F}_{\mathrm{C}} = \frac{\mathbf{F}_1 + \mathbf{F}_2}{2} \tag{4.5}$$

$$E_{\mathrm{C}} = \frac{E_1 + E_2}{2} + \frac{\delta x_{\mathrm{D}}}{2} \left(\mathbf{F}_1 - \mathbf{F}_2\right) \cdot \hat{\mathbf{N}} \tag{4.6}$$

Olsen *et al.* [110] discuss a modification to several transition state searchers that involves a modified step size and direction when in a 'convex' region, where all Hessian eigenvalues are positive. In these regions the TS searcher is moved a large set distance along the lowest eigenmode only, aiming to leave this region and enter the vicinity of a transition state quickly.

Demonstration on Oxirane Ring Opening

To test the applicability of the dimer method as a transition state refinement tool, a dimer search was initialized at each of the final bead positions on the 16-bead path making up the reaction coordinate of the first part of the oxirane–water reaction. Each dimer's orientation was initialized from the NEB tangent approximation at that bead, and to allow the beads to move away from low-force endpoints the dimer was required to take at least ten translation steps before converging. In total, four beads were able to locate the transition state. Figure 4.9 shows the span of beads along the NEB path in which it was possible for the dimer to find the transition state.

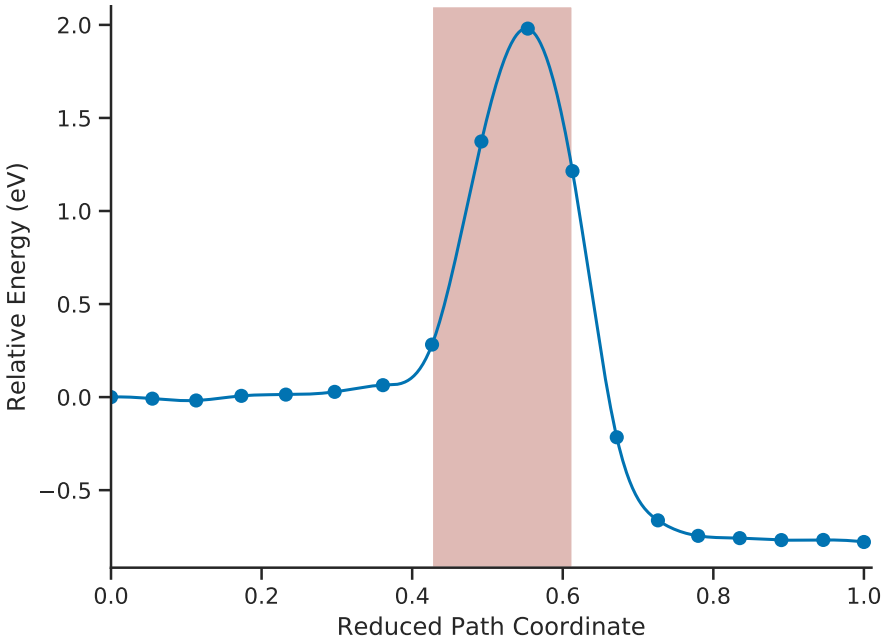

Fig. 4.9 Reproduction of Figure 4.2a showing the first part of oxirane ring opening. The dimer method was run from each bead's final position. The area in which the dimer method was able to locate the intermediate is shaded.

4.7 Further Work

4.7.1 Image Comms and NEB

Recently a preconditioner has been added to ONETEP's geometry optimizer that has been shown to substantially accelerate geometry methods such as optimization and saddle point searches [124]. More recently, this preconditioning scheme as well as an adaptive timestep method has been prepared specifically for minimum energy path serching methods such as NEB, offering both faster convergence and increased accuracy [125]. An implementation of this approach in ONETEP would bring these benefits to ONETEP's transition state tools. Additionally, the currently proposed preconditioner only affects the component of the NEB forces due to the potential energy surface, leaving open further work on the spring force components.

While the image-parallel running mode was implemented with NEB in mind, it was built directly on top of ONETEP's communications infrastructure and is not tied to any particular task. This functionality can be used in future to provide scalable implementations of tasks that involve interactions between similar systems. One

such task would be path integral molecular dynamics, which incorporates quantum mechanics into the nuclear degrees of freedom using Feynman path integrals [126], implemented by multiple systems connected by springs and interacting in lock-step in a way not dissimilar to NEB. Additionally, the simulations that an image-parallel run is made up of do not need to be the same size, making it applicable to different kinds of tasks involving potentially very different systems or systems being treated with different levels of theory that must interact during the progression of the task.

As mentioned, the current implementation of NEB handles one bead on each ONETEP image. This restricts the balance between wall time and processor count for a NEB calculation. Allowing more than one NEB bead to be managed by one ONETEP image would allow more user freedom to set up the same NEB calculation with fewer processors, at the cost of wall time. Some groundwork has been laid for this, including the geometry optimizer state struct that will allow multiple different geometry optimizations, one for each bead, to be maintained by one ONETEP image. This approach could mitigate lockstep cost under the assumption that faster-moving parts of the chain will have more expensive energy and force calculations. Moving a large distance along the potential energy surface can be assumed to cause a larger change in the NGWFs which limits the benefit of reusing them from the previous macroiteration as a starting guess. A worse starting guess generally requires more NGWF CG iterations to find the correct minimum, increasing the energy and force cost. On the other hand, parts of the chain that move relatively small distances each step, such as those next to the reactant or product, can be expected to converge quickly when reusing the NGWFs and density kernel of the previous iteration. By pairing up beads from different parts of the path on one ONETEP image, the expected lockstep cost can be expected to be minimized. Figure 4.10 shows the total number of NGWF CG iterations each bead took in converging both parts of the oxirane reaction illustrated in Figure 4.2. This demonstrates that intermediate images required more iterations to converge than those near the reactant or product.

A more flexible distribution of NEB beads to processor groups would also allow for the implementation of extensions such as AutoNEB, which automatically adds beads to increase resolution in sections of the path where the potential energy surface is steep or where the path resolution is low [127]. This method has been demonstrated to converge in fewer overall energy and force calculations than NEB for several systems. Reference [127] also discusses an observed tendancy for NEB's nudging to trap beads in local minima, inadvertantly increasing path length, reducing path resolution. An

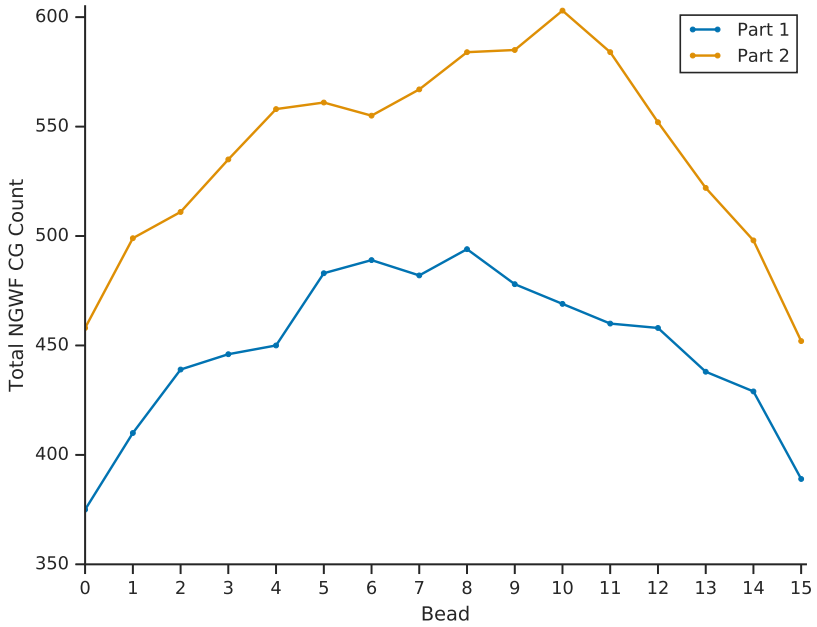

Fig. 4.10 Total NGWF CG count for each of the 16 beads in both parts of the oxirane reaction described in Section 4.4, including climbing image iterations. It shows in both cases that intermediate beads take on average longer per iteration to converge, motivating future work in load balancing.

elastic band method without nudging but with a climbing image is proposed to avoid this path lengthening.

Currently only the magnitude of the nudged force on atoms is used as a convergence criteria for non-climbing beads. While this is common for NEB implementations, it is not necessarily the only relevant condition. Currently displacement is not used as a convergence criteria as bead movement along a well-converged minimum energy path doesn't matter. A meaningful displacement criteria could be reintroduced by projecting out the component of displacement along the path direction. This would prevent convergence when beads are moving significantly perpendicular to the path but ignores motion along the minimum energy path. This kind of perpendicular motion would affect tangent approximations and change the overall path dynamics and so strictly should not be ignored.

The performance of the FIRE optimizer is dependent on the selection of its many parameters. The parameters currently used in ONETEP are mostly those reported in the FIRE source paper [106]. It is reported there that the parameters are not very sensitive to system, but a broader investigation of this in ONETEP for both geometry optimization and NEB could improve performance. In particular, the parameter controlling the maximum timestep is only given as a rough estimate.

4.7.2 Transition State Refinement

The dimer method has several parameters that must be tuned for good performance. It is possible that a better parameterization could lead to a more robust approach to refine the transition state. In particular, the limits and convergence criteria of the rotation step should be carefully investigated. This functionality was developed after most of the results in this thesis were generated. Next steps could involve using this functionality to determine CO dissociation energies from NEB calculations performed without a climbing image to reduce the overall cost of arriving at the tranisiton state.

As discussed in Section 2.3.6, the dimer method is one of several transition state refinement methods that do not require knowledge of the final states. A method that did not use multiple ONETEP images like the Lanczos approach described in Section 2.3.6 [112] could be more appropriate for large systems and would contribute to a more complete suite of transition state tools in ONETEP.

The 'exact' dimer method described here is implemented with two ONETEP images, one responsible for each point making up the dimer during rotation, with the energy and force of the centerpoint approximated. It is possible to implement an approximate

dimer method that performs calculations on only one of the dimer points explicitly. [110]. The forces at the centerpoint and one of the dimer points are calculated exactly, and the current approximations rearranged to instead approximate those quantities at the other dimer point. These approximations are updated as the explicit dimer point rotates. The dimer energy is not explicitly calculated and is not used as a convergence criteria, though it could also be approximated. This approach would give a single-image alternative implementation of the same method.

Chapter 5

Role of CO feed binding in the mobility of Co on TiO_2

Note on the Republishing of Data

My MPhil project [101] involved a study of cobalt adsorption and mobility on the (101) anatase-form TiO_2 surface in the presence of reactor species. Mobility was considered by constructing a single path across a portion of the surface connecting two unique adsorption sites and performing a NEB calculation in VASP. In addition to atomic Co, CoO and CoCO were considered, as was Co in the presence of surface-adsorbed water, which is a product of the Fischer–Tropsch reaction. The study showed a connection between both adsorption strength and mobility barriers and the presence of surface water or Co-bound reactor species. However, the NEB paths were generally slightly under-converged and revealed a number of better-adsorbed geometries that were not accessed by geometry optimization. Since then, the results have been refined and the study greatly extended in scope, and some values from the original study are reproduced here for clarity and context. Specifically, the adsorption energies on the dry surface of Co at both adsorption sites, CoO at site B, and CoCO at site A, as well as the Co mobility barrier, are reproduced from my MPhil dissertation, as are the adsorption energies of Co at sites A and B of the hydrated surface. Reference [101] is cited where results containing these values are used.

The study described in this chapter is also reported in Reference [128]. The data generated in producing these results are available at https://doi.org/10.17863/CAM.10158.

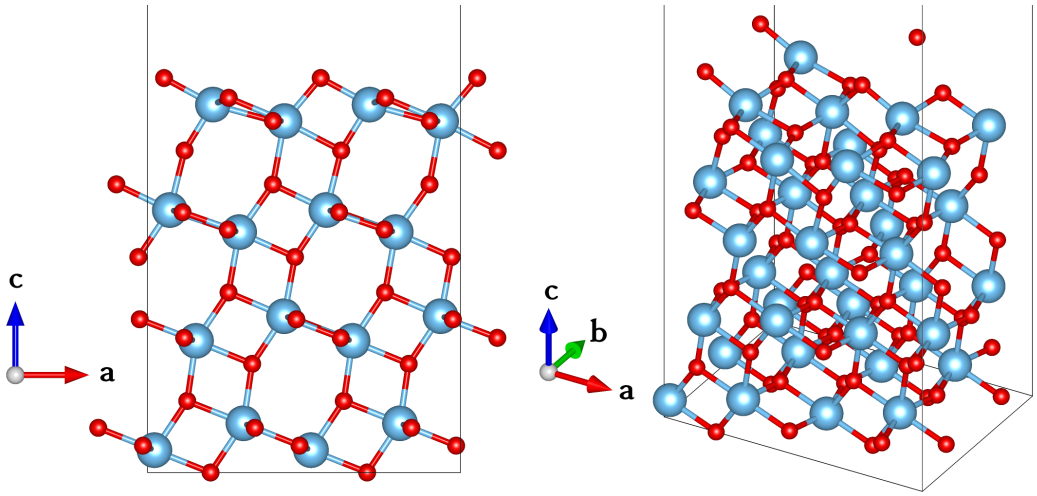

Fig. 5.1 Simulation cell for the anatase (101) surface. Axes show the $\mathbf{a} = [10\bar{1}]$,$\mathbf{b} = [010]$, and $\mathbf{c} = [101]$ directions. Image source: [101].

5.1 Simulation Parameters

Calculations in this study were performed using the VASP code [60–63]. VASP was chosen because the system size is relatively small and its real-space projector calculation for the non-local part of the pseudopotential reduces the cubic-scaling cost as well as the cost due to vacuum space [64]. Calculations on isolated molecules were k-point sampled at the Γ point only, while those on surfaces were sampled on a 2×2 Γ-centred Monkhorst-Pack grid [70]. PAW datasets were used, generated using the PBE [129, 130] GGA exchange correlation functional. This functional was chosen for its general applicability. A plane-wave kinetic energy cut-off of 400 eV was used. Geometry optimization energy and force parameters were set to 1×10^{-5} eV and 0.01 eV Å^{-1} respectively. Convergence of the simulation parameters is discussed in my MPhil dissertation [101]. Climbing-image NEB was used to generate minimum energy paths between sites A and B on the surface. This functionality in VASP is maintained by the Henkleman group at UT Austin [131]. Between 6 and 8 NEB beads were used for each path.

The (101) anatase TiO_2 surface was modelled using 96 atoms, four surface layers, in a 10.332 Å×7.636 Å×27.005 Å orthogonal periodic box, giving 14 Å of vacuum above the surface. This surface is depicted in Figure 5.1. For geometry optimizations, the bottom layer of 24 atoms was held fixed in the bulk-like configuration. Cell dimensions were always held fixed.

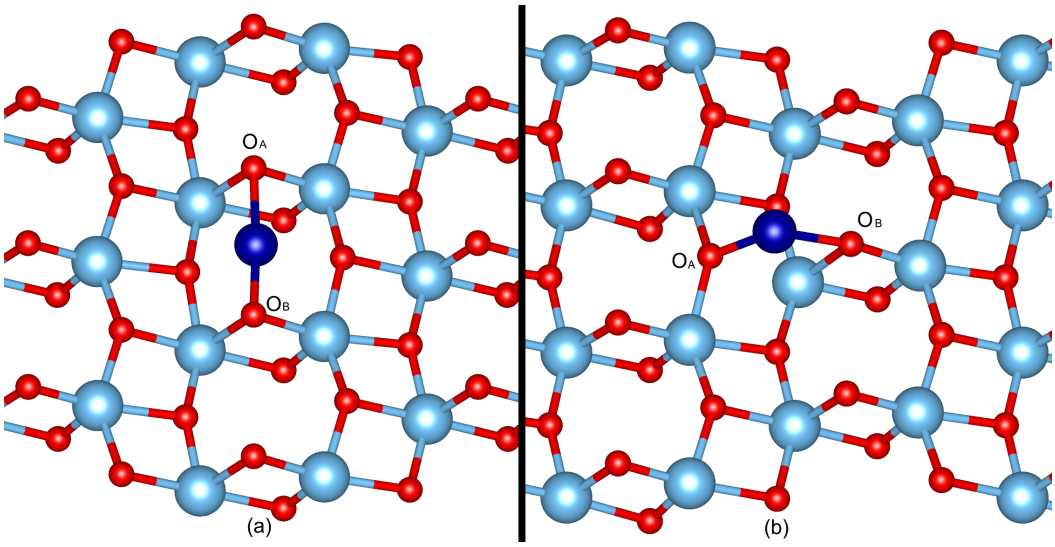

Fig. 5.2 The adsorption sites of atomic cobalt on the surface. The oxygens labelled O_A and O_B act to define the surface angle, reported in Appendix A. These sites were found in the MPhil year. The site in (a) is the strongest binding site, labelled site A, and (b) is the second-strongest binding site, labelled site B.

This study involves two adsorption sites on the surface. These sites were identified in previous work as the sites with the strongest and second-strongest adsorption of atomic Co, referred to as sites A and B respectively. These sites were determined by a search of optimized Co positions and energies starting from several positions within one repeat of the anatase surface. Figure A.1 identifies both of these sites. Adsorption energies ΔE_{bind} are defined as in Section 2.2.

Key geometry parameters for adsorbed configurations are reported in Appendix A. These include, where applicable, Co–O or Co–C bond lengths, coordination numbers of the Co atom with the surface oxygens, surface angles, and adsorbate heights relative to that of atomic Co. An oxygen is considered coordinated if it is within 2.5 Å of the cobalt atom. Surface angles are defined as the O_A–Co–O_B angle at the relevant site in Figure A.1. Bader charge analysis indicates that the adsorbed cobalt atom exists mostly in the +2 oxidized state with some reduction when under-coordinated. Details of the Bader charge analysis are in Appendix B.

5.2 Results

5.2.1 Extension of Dry-Surface Adsorption Study

A fourth species of interest was identified: CoOH can be formed through water-splitting, either in a surface or gas-phase reaction. The adsorption and mobility of CoOH were therefore also investigated. Figures 5.3 and 5.4 show the geometries of CoOH adsorbed at sites A and B respectively.

The adsorption and mobility properties of $Co(CO)_2$ and $Co(CO)_3$ were also calculated to investigate the effect of additional potentially relevant reactor species on cobalt sintering. Figures 5.5 and 5.6 show the respective geometries of $Co(CO)_2$ at sites A and B. Figures 5.7 and 5.8 show the respective geometries of $Co(CO)_3$ at sites A and B. Because $Co(CO)_3$ is only coordinated to one surface atom, the path from A to B does not involve any chemical bond breaking or forming and the mobility barrier cannot be interpreted in the same way.

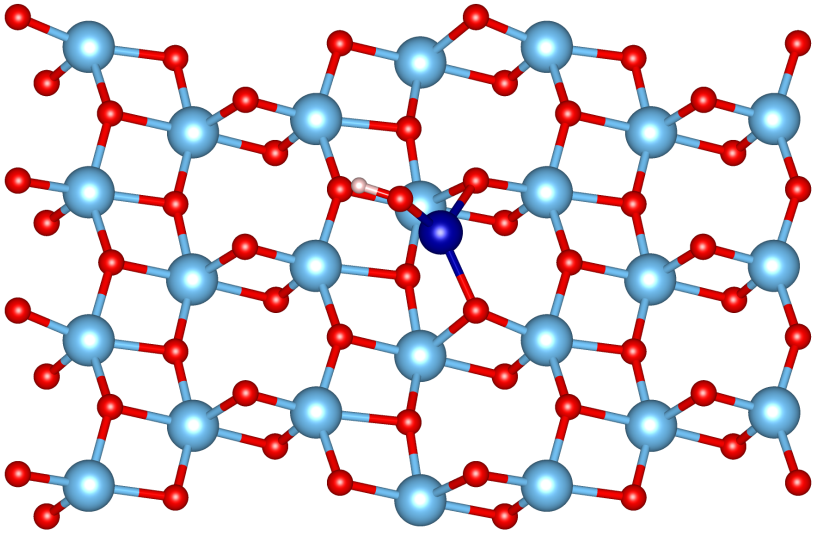

Fig. 5.3 Site A geometry of CoOH, with an adsorption energy of 3.350 eV. As with other molecular adsorbates, the Co atom has moved away from one of its coordinated surface O atoms.

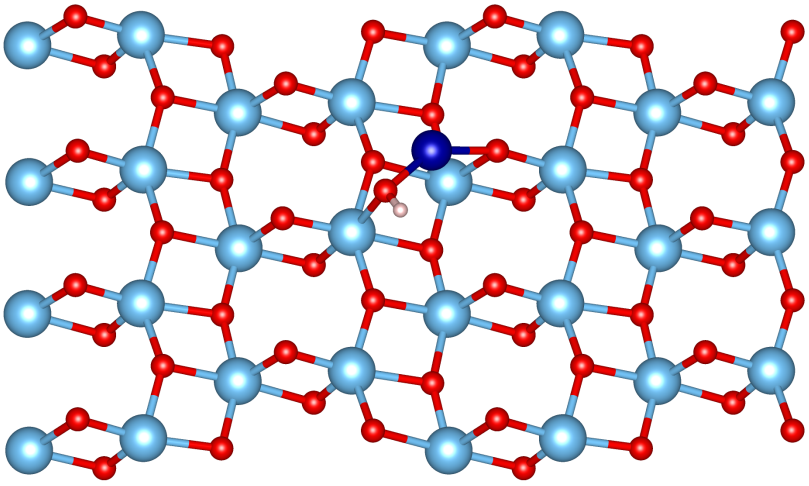

Fig. 5.4 Site B geometry of CoOH, with an adsorption energy of 2.878 eV. In order to coordinate with one of the surface Ti atoms the Co atom is pulled off of its higher-symmetry adsorption site.

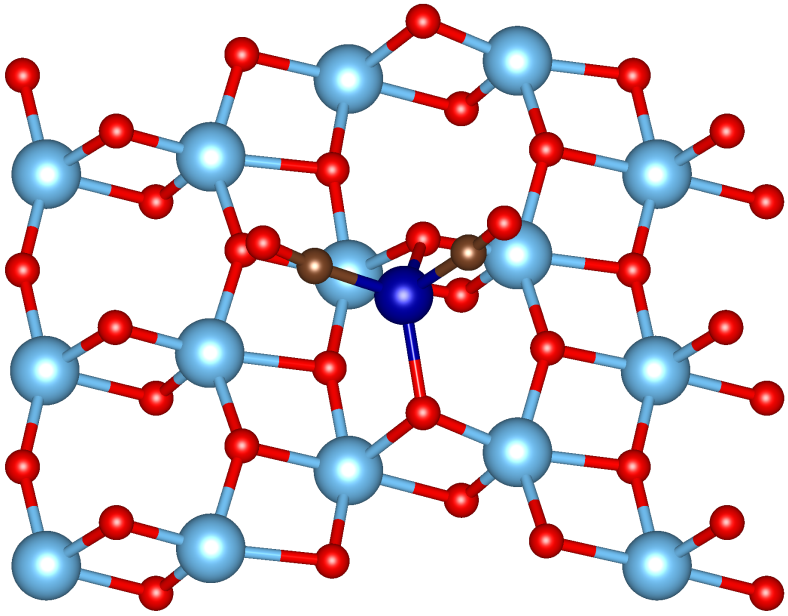

Fig. 5.5 Site A geometry of $Co(CO)_2$, with an adsorption energy of 1.653 eV

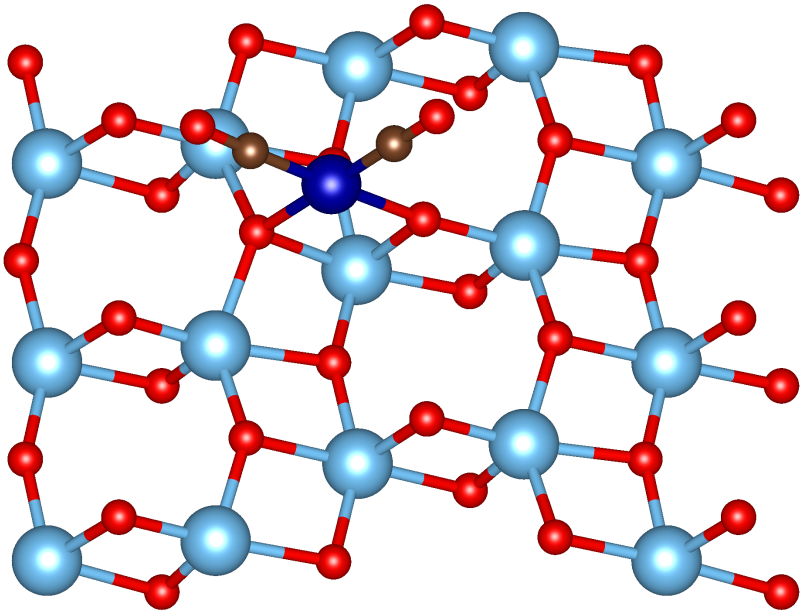

Fig. 5.6 Site B geometry of $Co(CO)_2$, with an adsorption energy of 1.684 eV

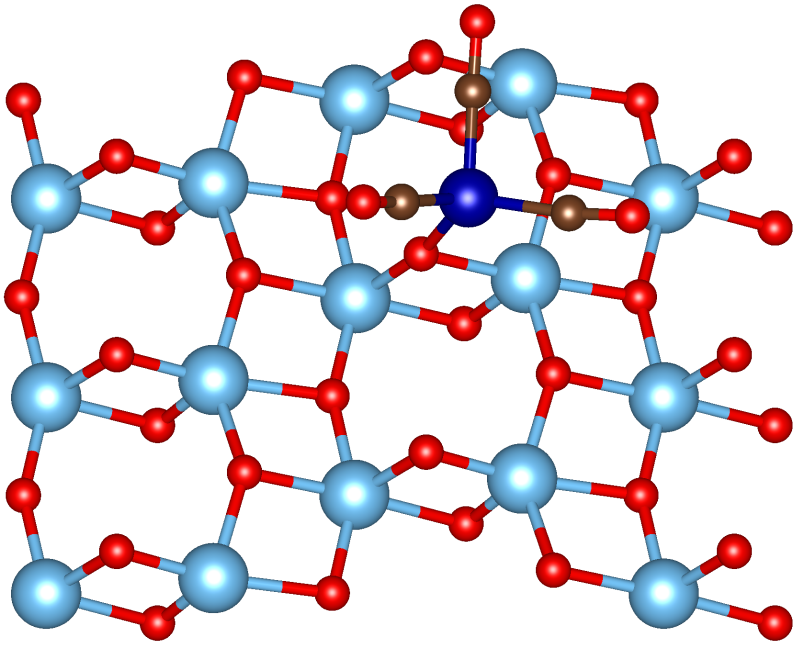

Fig. 5.7 Site A geometry of $Co(CO)_3$, with an adsorption energy of 1.015 eV

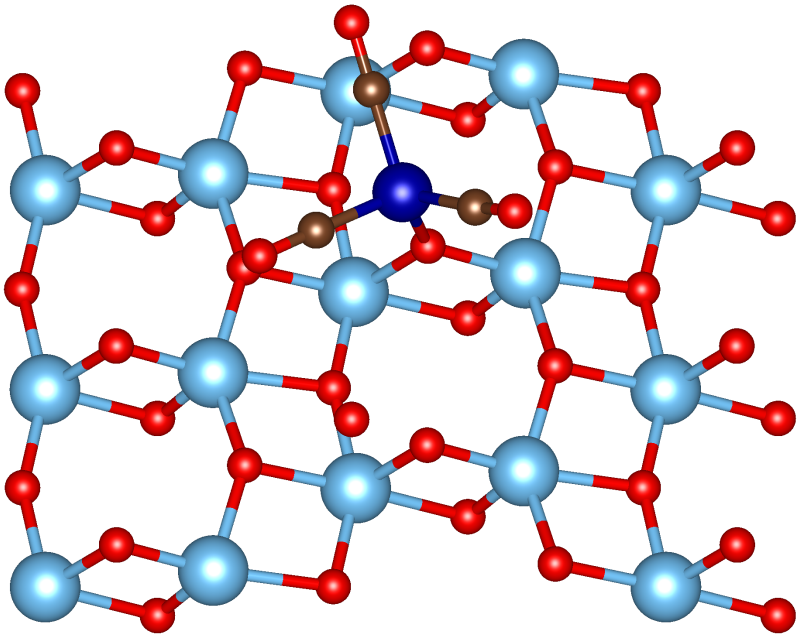

Fig. 5.8 Site B geometry of $Co(CO)_3$, with an adsorption energy of 0.752 eV

Figure 5.9 shows the adsorption energies at sites A and B of Co, CoO, CoOH, and cobalt carbonyls up to $Co(CO)_3$ [101]. Generally site A has a stronger adsorption than site B. This can be attributed to the higher coordination of the Co atom with the oxygen atoms in the surface and the proximity to an under-coordinated surface Ti atom for interaction with oxygen-containing adsorbates. In addition to CoOH, Figure 5.10 shows CoO at site A also coordinating with a surface Ti atom. Another feature of note is that when bound to a reactor species Co moves to reduce its surface coordination number and maintain 4 bonds. This can be seen particularly with the carbonyls; each additional carbonyl decoordinates the cobalt atom with a further surface oxygen atom.

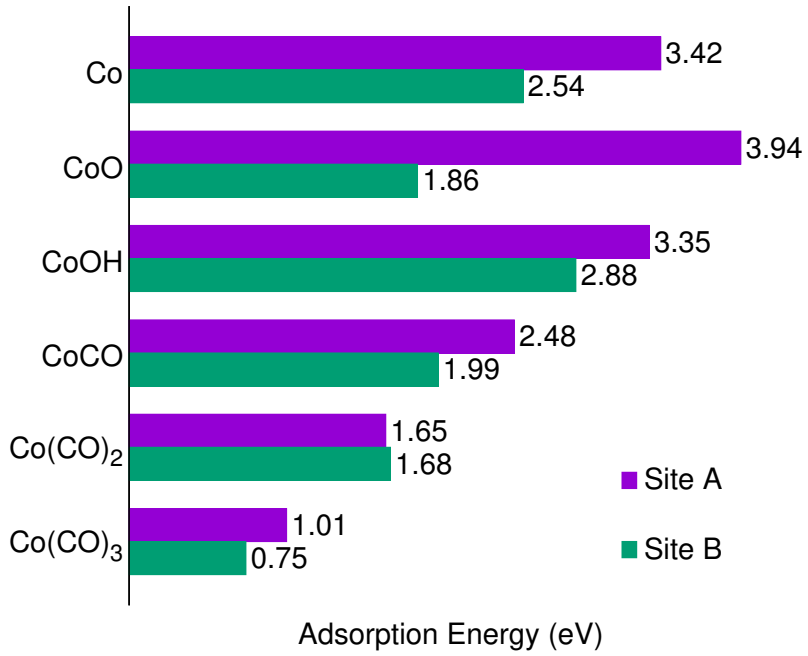

Fig. 5.9 Adsorption energies of several Co-containing species on the anatase TiO_2 (101) surface.

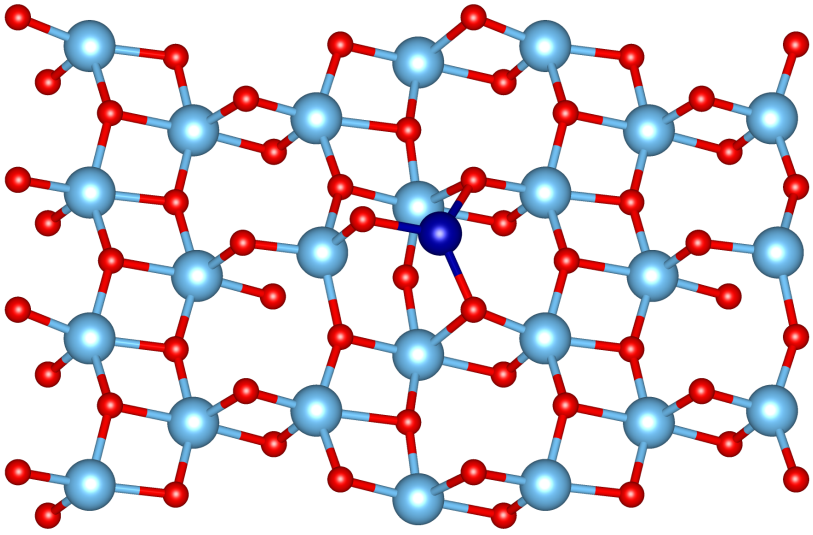

Fig. 5.10 Site A geometry of CoO, with an adsorption energy of 3.940 eV. The O atom in the adsorbate coordinates one of the exposed undercoordinated Ti atoms on the surface.

5.2.2 Mobility on the Dry Surface

Figure 5.13 shows the forward barrier for motion from site A to site B on the support surface of each adsorbate [101]. This path involves rotating around one of the surface oxygens between the two sites. This path is depicted in Figure 5.11, and the NEB energy profile of the path is shown in Figure 5.12 [101]. While this path does not provide a full path for 2D surface motion, it does in most cases break important Co – O surface bonds in the most tightly bound configuration. A complete surface diffusion model would require breaking the bond with the second oxygen atom and motion to the next A site in the $[10\bar{1}]$ direction. As CoO bonds with an exposed Ti atom at site A it has a strong barrier compared to other adsorbates. The barrier found had two parts, consisting of the initial breaking of the Co with one of the surface oxygen atoms into a shallow intermediate, with an adsorption energy of 3.198 eV and a forward barrier from site A of 0.752 eV, followed by a breaking of the Ti – O bond making up the majority of the energy cost.

CoCO and CoOH have significantly reduced mobility barriers compared to that of Co, likely due to the reduced coordination of the adsorbate to the surface. This trend is continued with a further reduced barrier for $Co(CO)_2$.

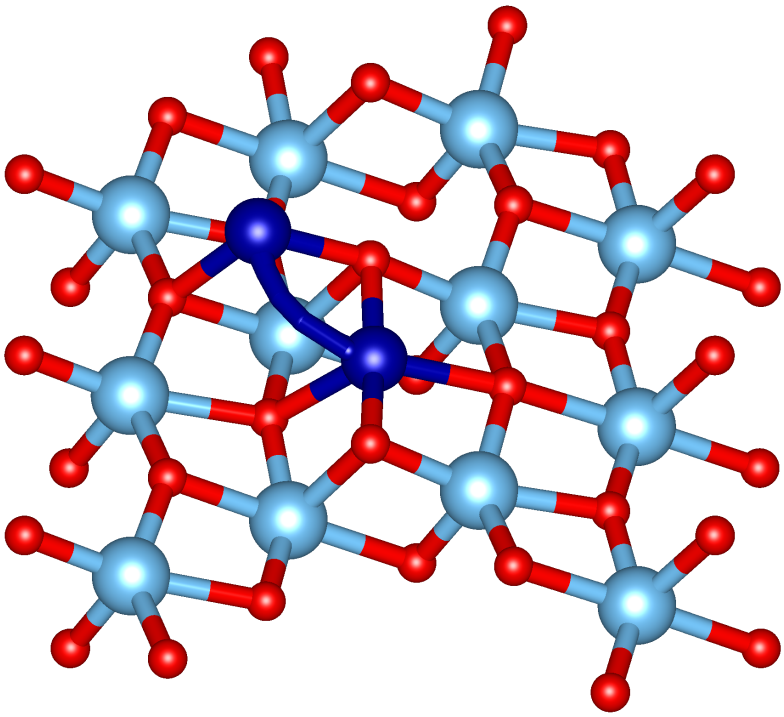

Fig. 5.11 Representation of the path taken by Co in moving from site A to site B.

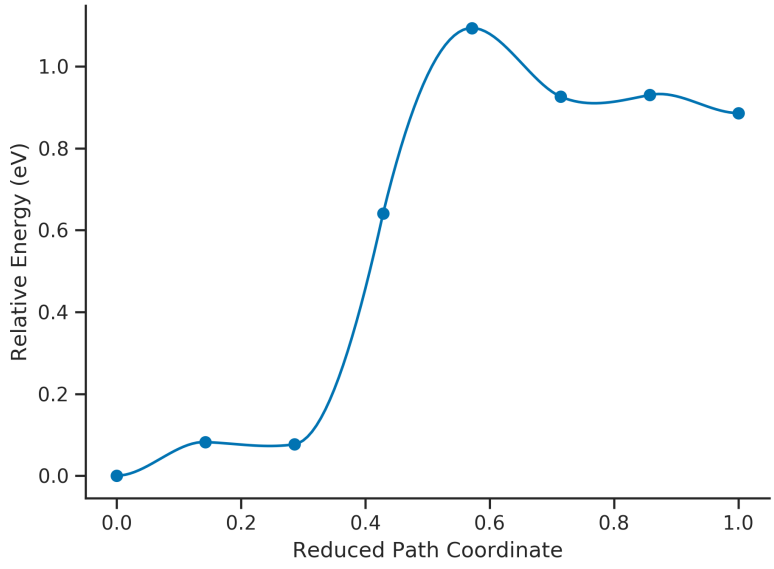

Fig. 5.12 NEB energy profile of the path taken by Co between sites A (reduced coordinate 0.0) and B (reduced coordinate 1.0). A cubic spline has been added. Six beads represented the path between the two sites.

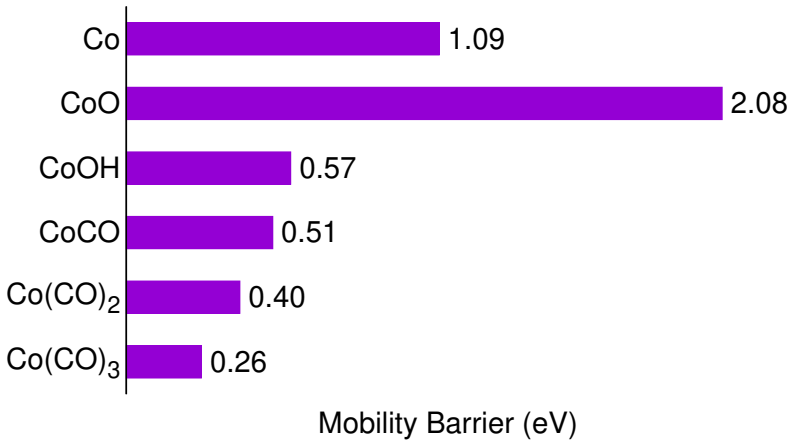

Fig. 5.13 Forward mobility barriers from site A to site B of several cobalt-containing species on the anatase (101) surface.

5.2.3 Effects of Surface Hydration

The support surface is generally not dry, with water being generated in the form of steam by the Fischer–Tropsch process. The structure of the anatase (101) surface covered with a monolayer of water is known [132]. The surface with a single monolayer (mL) of water is shown in Figure 5.14. The effect of water coverage on atomic Co was investigated at a preliminary level in the MPhil project [101]. Since then, a detailed investigation has been performed on a range of adsorbates. Note that for adsorption energy calculation the clean surface is defined as the relaxed surface with 1mL water coverage.

Both CoO and CoOH were found to interact strongly with the water layer when placed near their adsorption sites and their relaxed geometries contain some chemical changes. Specifically, both species induced one of the surface water molecules to split into a surface-adsorbed OH group. Figure 5.16 shows that CoO adsorbed at site B has the OH coordinated to an under-coordinated surface Ti atom, while the remaining H atom binds to the adsorbate to form CoOH. CoO at site A, shown in Figure 5.15, does not have the same chemical change, instead displacing a water molecule from the monolayer to adsorb in a similar way to the dry surface case. Figure 5.17 shows CoOH at site A splitting the water to again become a surface-adsorbed OH group, this time forming a water molecule above an atomically adsorbed Co atom. A similar process happens at site B, shown in Figure 5.18.

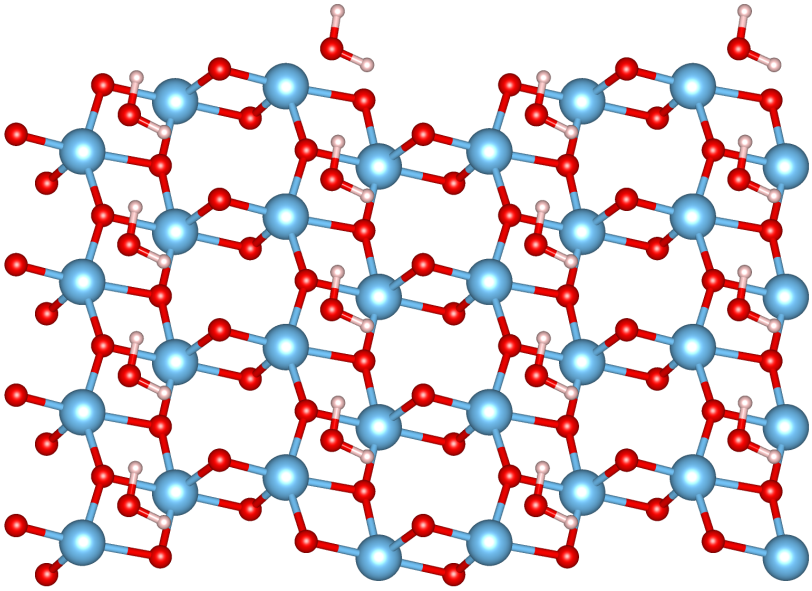

Fig. 5.14 Geometry of the 1ML hydrated TiO_2 anatase (101) surface. Water molecules adsorb to the surface in such a way that they coordinate one of the surface Ti atoms.

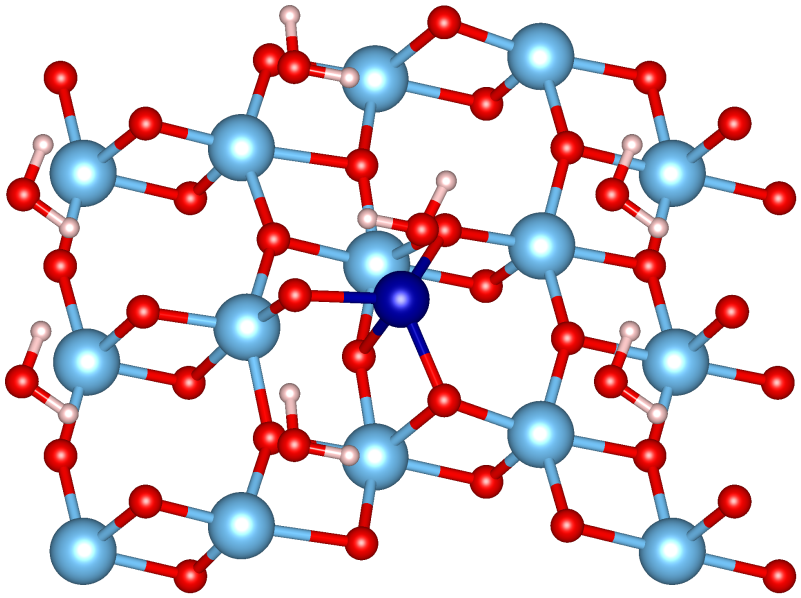

Fig. 5.15 Site A geometry of CoO on the 1ML hydrated surface. Unlike at site A it retained its chemical structure during optimization at this site.

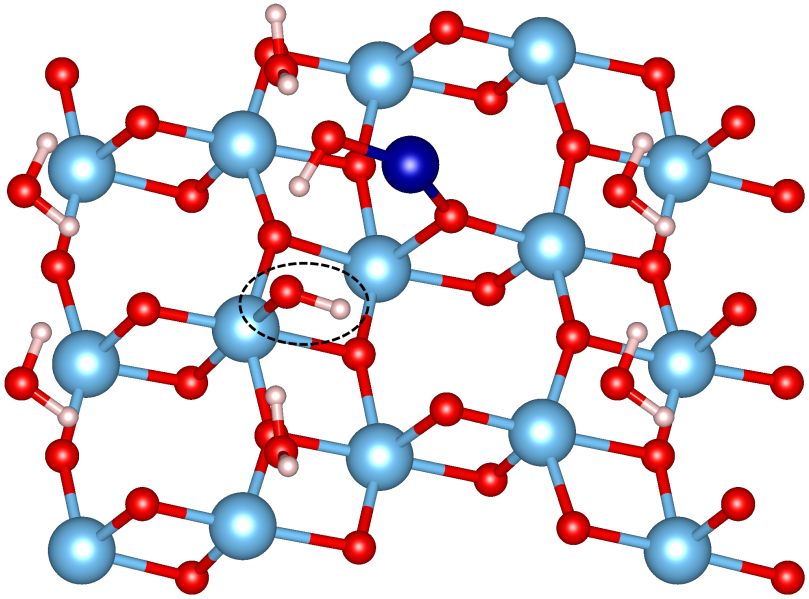

Fig. 5.16 Site B geometry of CoO on the 1ML hydrated surface. The adsorbate has split one of the water molecules, creating a surface-adsorbed OH group (circled) and a CoOH molecule.

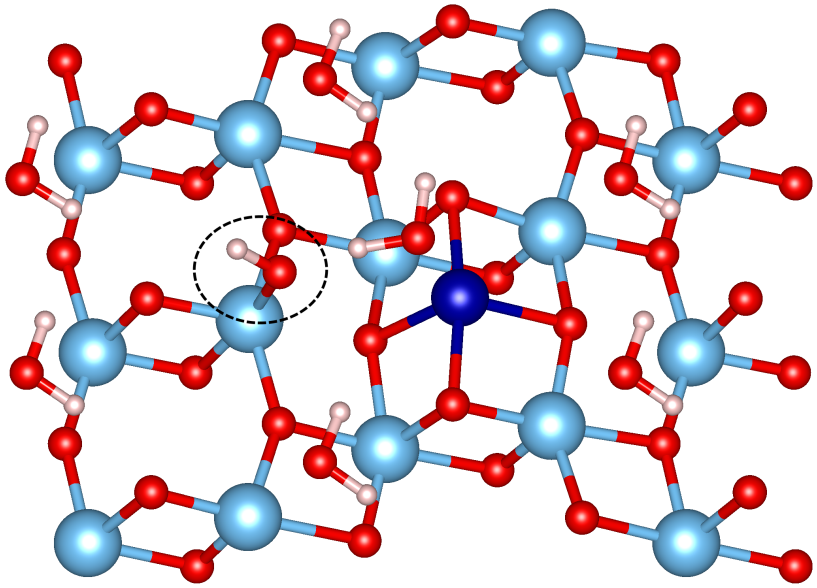

Fig. 5.17 Site A geometry of CoOH on the 1ML hydrated surface. The adsorbate has split one of the water molecules, creating a surface-adsorbed OH group (circled) and a water molecule along with atomically adsorbed Co.

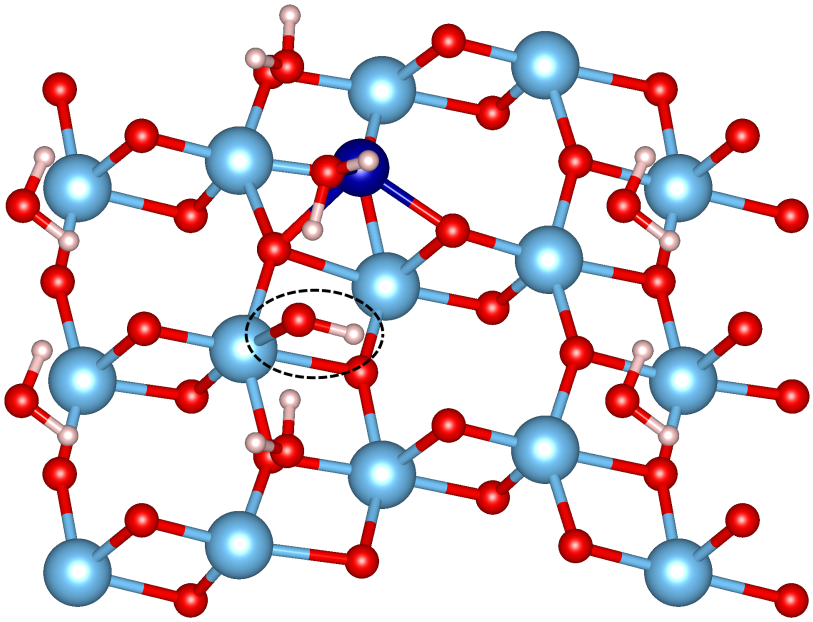

Fig. 5.18 Site B geometry of CoOH on the 1ML hydrated surface. As at site A, the cobalt is adsorbed similarly to the atomic case, forming instead a surface-adsorbed OH group (circled) through interaction with the water layer.

These results indicate that the adsorption of oxygen-containing adsorbates may be made unstable in the presence of water. The support-adsorbed OH group in each case brings an under-coordinated surface titanium atom to bulk-like coordination which may be highly favourable. However, this suggestion is not conclusive and these results are not directly comparable to the rest of the results obtained. Instead, the hydrated study focuses on the cobalt carbonyls which are found not to interact significantly with the water monolayer. Figures 5.19 to 5.23 show the adsorbed geometries of the cobalt carbonyls up to $Co(CO)_3$ at sites A and B of the hydrated surface. $Co(CO)_3$ was only found to have one adsorption site on the hydrated surface.

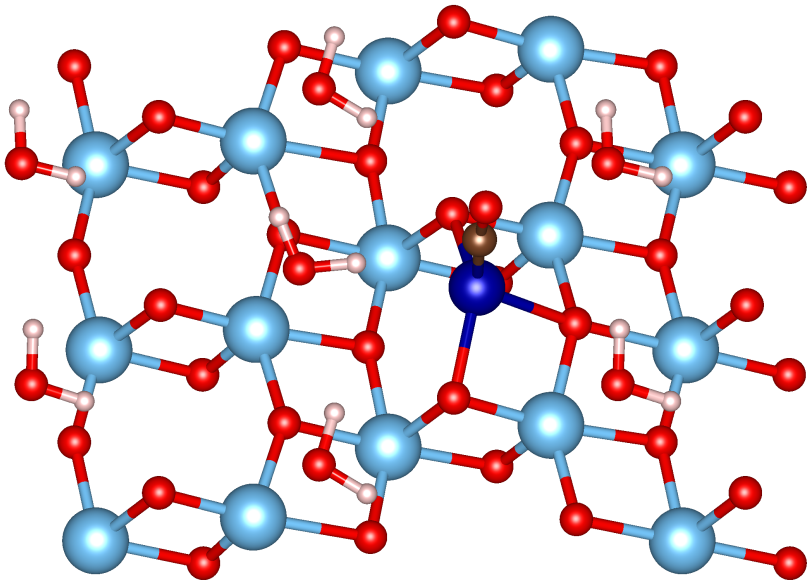

Fig. 5.19 Site A geometry of CoCO on the 1ML hydrated surface with an adsorption energy of 1.971 eV.

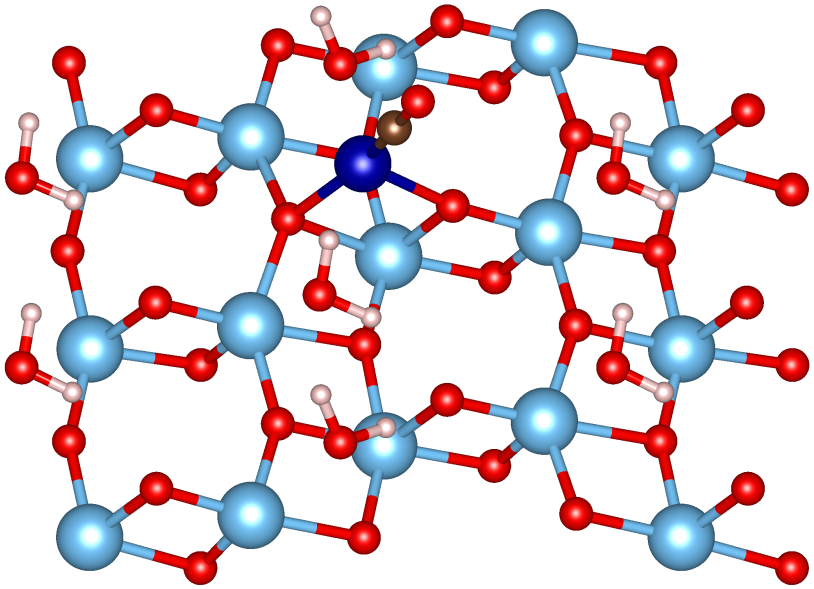

Fig. 5.20 Site B geometry of CoCO on the 1ML hydrated surface with an adsorption energy of 2.273 eV.

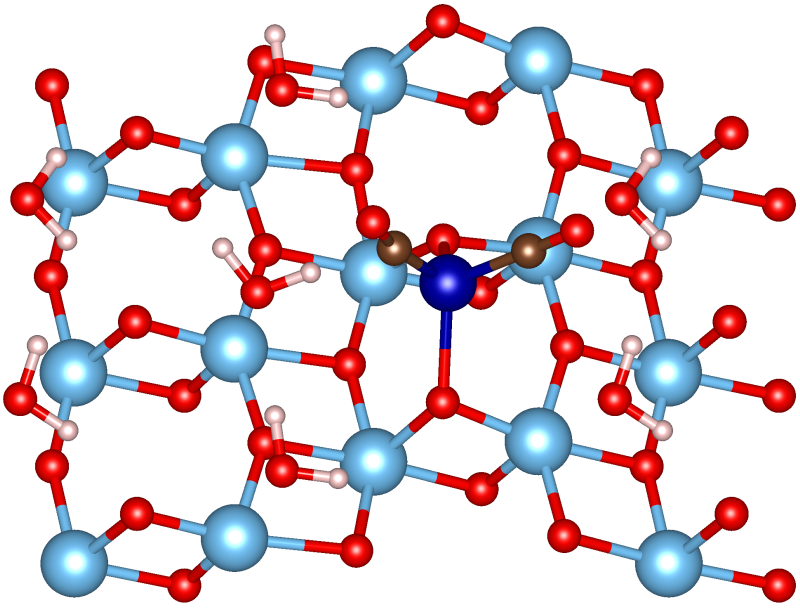

Fig. 5.21 Site A geometry of $Co(CO)_2$ on the 1ML hydrated surface with an adsorption energy of 1.104 eV.

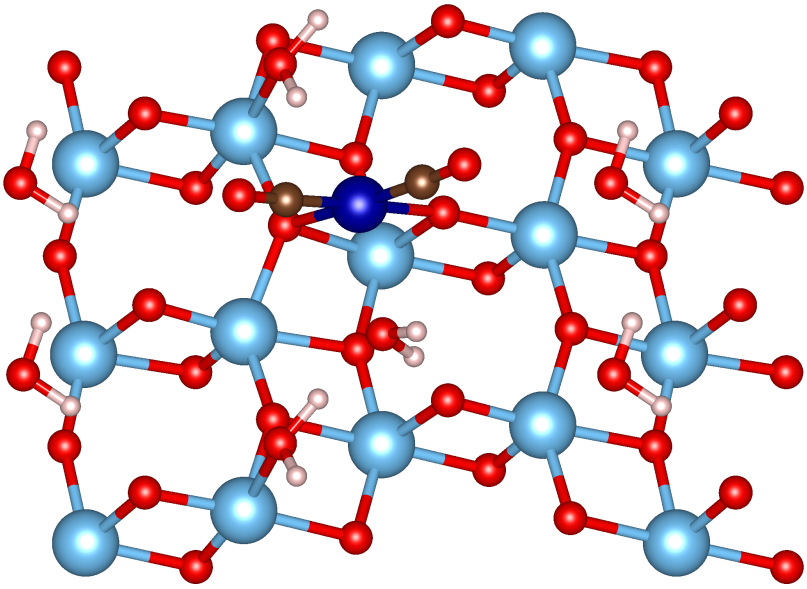

Fig. 5.22 Site B geometry of $Co(CO)_2$ on the 1ML hydrated surface with an adsorption energy of 1.748 eV.

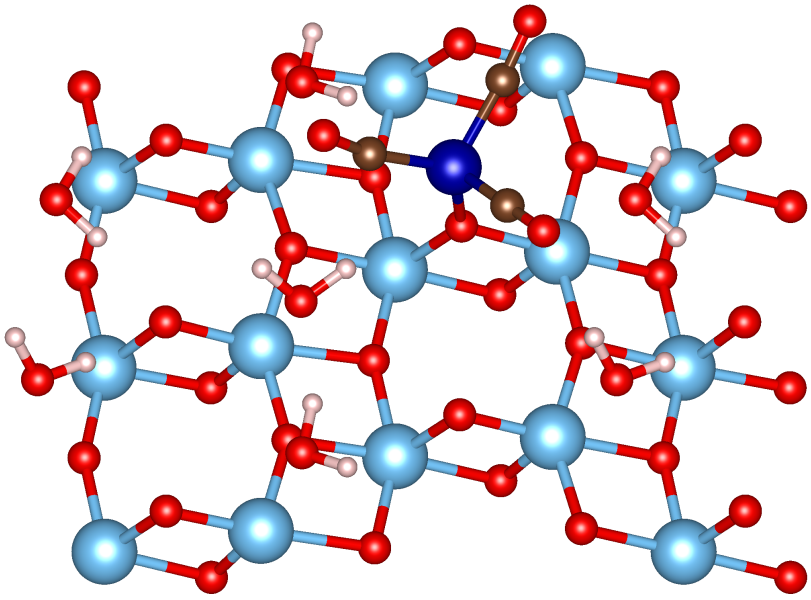

Fig. 5.23 Geometry of $Co(CO)_3$ adsorbed on the 1ML hydrated surface with an adsorption energy of 0.819 eV.

Figure 5.24 shows the adsorption energies of Co and the cobalt carbonyls up to $Co(CO)_3$ at sites A and B on the 1ML hydrated surface [101]. The adsorption energies of Co and CoCO were not significantly affected by the presence of water; the carbonyl still has a strong and comparable effect on reducing the adsorption energy of the adsorbate. Surface hydration also had a minor effect on the mobility barriers of these to species, with hydration reducing the barrier from 1.094 eV to 1.046 eV for Co and from 0.512 eV to 0.448 eV for CoCO.

The site A adsorption energy of $Co(CO)_2$ was significantly reduced on the hydrated surface. Additionally, the mobility barrier from site A was found to be negligible. Instead, an intermediate state, shown in Figure 5.25, was identified with a much stronger adsorption energy of 1.748 eV and a forward mobility barrier to site B of 0.247 eV. This intermediate was identified by a second minimum in the NEB path and a geometry optimization of that minimum's structure. The site A structure would likely transition quickly into this state in practice. This intermediate has an adsorption energy comparable to the adsorption energies of $Co(CO)_2$ on the dry surface.

$Co(CO)_3$ was found to have only one adsorbed configuration that is similar to its adsorption on the dry surface. It remains relatively weakly bound to the surface.

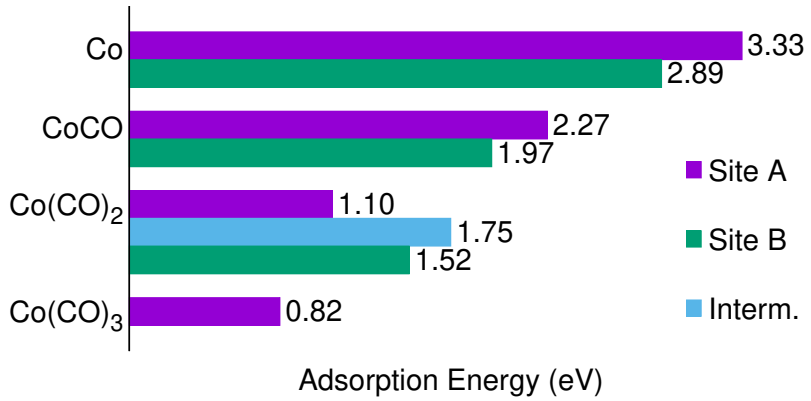

Fig. 5.24 Adsorption energies of several Co-containing species on the 1ML hydrated anatase TiO_2 (101) surface.

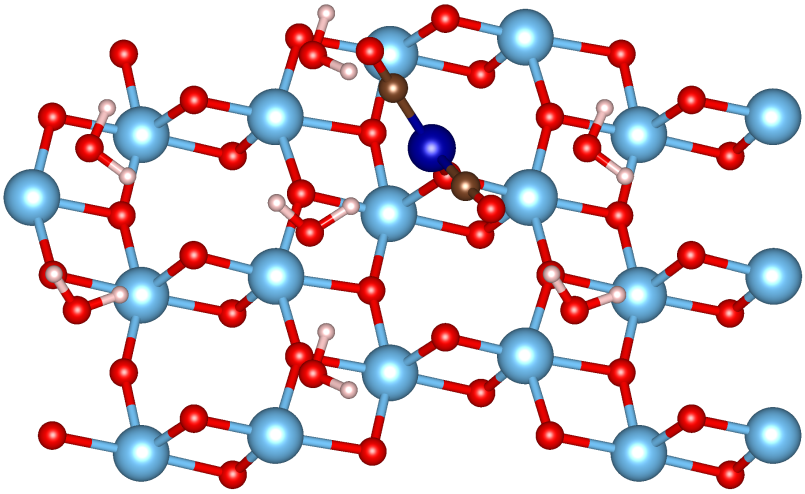

Fig. 5.25 Intermediate structure on the 1ML hydrated surface with an adsorption energy of 1.748 eV.

5.3 Formation Energies of the Cobalt Carbonyls

The adsorption and mobility properties of the cobalt carbonyls and their apparent stability in the presence of water make them potentially active in the ripening process if they form in reactor conditions. An argument for their formation can be made based on a theoretical reactor environment. Details of this approach are given in Section 2.2. The energies here refer to formation from a slab of the anatase support with a cobalt atom adsorbed to it, in equilibrium with an ideal gas of the carbon monoxide feedstock at a given partial pressure and temperature. Figure 5.26 show the formation energies of the carbonyls at 500 K in the CO partial pressure range at which they cross. At 10 atm the formation of $Co(CO)_3$ remains favourable at temperatures exceeding 1500 K, well beyond those found in a reactor. It is clear that over all pressure ranges that would be encountered in a realistic reactor the formation of large and mobile carbonyl species from isolated cobalt on the surface, according to this model, is favourable.

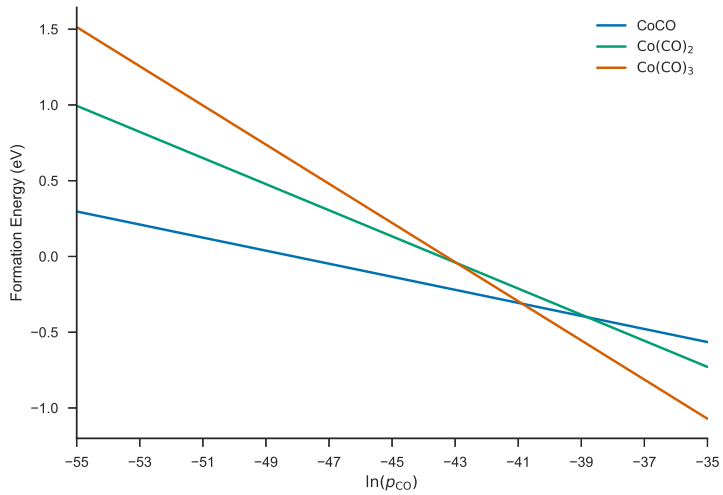

Fig. 5.26 Formation energy of the cobalt carbonyls from a support-adsorbed cobalt atom at 500 K over a range of pressures over which they become favourable and cross. At this temperature the formation of large mobile carbonyls remains favourable under reactor conditions. Pressures are in atm.

5.4 Discussion of Results

The results indicate a strong relationship between the reactor environment and the adsorption and mobility of surface Co. Gas-phase species binding to the Co atom at

its binding site were found to decrease its surface coordination. This is expected to decrease adsorption energy, as can be seen with CoCO, but the new molecule also gained the ability to interact with the nearby exposed Ti atom, as is the case with CoO and CoOH. Once a highly interactive species like CoO forms it may be difficult to remove from the surface by desorption or surface transport without further chemical interaction.

Water was known to adsorb to the surface at sites coordinating the exposed Ti atom [132]. It appears from the results that a surface OH group at that site is stable enough to induce a chemical change in CoOH, and CoO at Site B. This indicates that both of these species may break down into cobalt and water on short time scales or remain adsorbed to the surface. Because the hydrated surface is a more realistic model, this effect would reduce their potential impact on ripening. The surface-adsorbed water had little effect on the adsorption or mobility of Co or CoCO, neither of which interacted strongly with the water later at their adsorption sites.

CoO on the dry surface had a large site A adsorption energy and mobility barrier. Examination of the minimum energy path shows the motion having two stages. The first is a rotation of the Co around its O atom from site A to site B, with the O atom remaining relatively stationary relative to the surface Ti. The second stage has a higher energy cost and is associated with the desorption of the O atom. Both the intermediate and product lie in very shallow energy minima, indicating that at finite temperature the adsorbate would likely return to the main binding site very quickly. A more thorough investigation of the effect that water has on CoO near site A is required to reveal whether this configuration is stable under reaction environments or if it will also eventually break down into surface-adsorbed Co.

Both CoCO and CoOH had a significantly smaller mobility barrier than atomic Co on the dry surface. Unlike CoOH, CoCO does not interact with surface-adsorbed water or the surface itself. Because of the decrease in both adsorption energies and in mobility barriers, the results indicate that CO feed binding may act to accelerate ripening in realistic surface conditions. However, the identification of a strongly-adsorbed intermediate state of $Co(CO)_2$ that is present only on the hydrated surface indicates that deeper interactions between the adsorbate and a hydration layer not identified here are possible. Additionally, coordinated motion or reaction paths involving chemically distinct intermediates were not explored.

Arguments based on the formation of cobalt carbonyls in a reactor environment indicate that when cobalt is atomically adsorbed to the support surface it is favourable

to form highly mobile large cobalt carbonyls. These species desorb from the surface and migrate across it much more readily than a lone cobalt atom, potentially re-adsorbing to larger cobalt clusters and contributing to the ripening process.

The results found here are in line with experimental findings that CO-driven ripening involving monotomic cobalt may contribute to deactivation of the FT catalyst on some surfaces [44, 46, 47]. This study provides a predictive model of this effect on an anatase support. An experimental investigation into these effects on the anatase surface, and in particular how the anatase support surface composition may affect ripening under reactor conditions with and without the presence of CO, could provide additional support for the results found here and provide a direction towards mitigation of CO-driven ripening.

These results suggest that once the ripening process breaks monatomic cobalt onto the surface of the reactor, it will be accelrated by the reactor feed in realistic conditions. Further experimental work based on these results might be directed at better understanding the conditions under which monatomic cobalt breaks onto the support surface, and if this step is preventable without losing reactor performance. It also prompts further work in understanding the extent to which CO-driven ripening affects deactivation and whether the breaking or the CO-accelerated recombination are the rate-limiting steps of this ripening process. Further computational work supporting those studies might explore the breaking off of cobalt atoms from cluster surfaces, and if reactor species and conditions may affect that step as well.

Chapter 6

Carbon Monoxide Adsorption and Dissociation on Small Cobalt Particles

The developments described in Chapters 3 and 4 can be used to explore new aspects of Fischer–Tropsch catalysis that are now accessible in ONETEP. This includes construction of cobalt structures and study of adsorption and chemical processes on them. This chapter illustrates some of these studies that can now be done in ONETEP. While the sizes of systems explored here are also treatable with traditional, cubic-scaling DFT methods, this chapter serves to illustrate new functionality that could be applied to larger systems, and to provide a starting point for further research that could be extended to larger systems.

All the simulations in this chapter were carried out using ONETEP [57, 58]. In all cases, the density kernel was not truncated and the PBE GGA exchange-correlation functional was used [129, 130]. Free-spin EDFT was used, with net spins initially relaxed from $3\mu_{\mathrm{B}}$ times the number of cobalt atoms in the clusters. The fixed spin period varied from 0 to 2 NGWF CG iterations. A cutoff energy of 1100 eV was used, yielding a 117×117×117 psinc grid in the 25 Å×25 Å×25 Å cubic simulation cell. NGWFs of $12\,a_0$ were used, with 13 NGWFs on Co atoms and 4 each on C and O atoms, with core states represented by the JTH PAW datasets for the PBE functional [133].

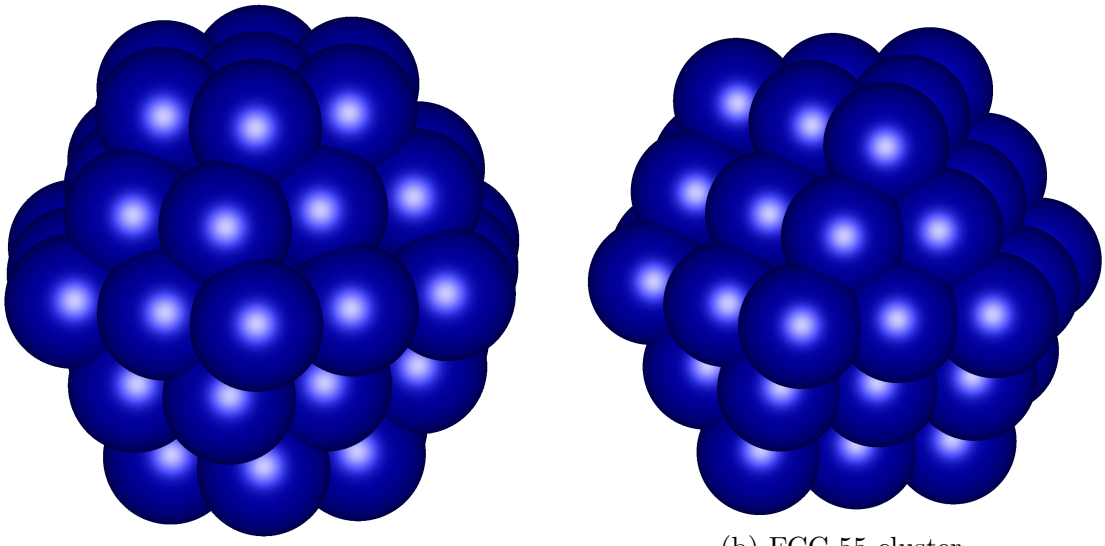

(a) HCP-57 cluster

(b) FCC-55 cluster

Fig. 6.1 Optimized structures of (a) the 57-atom HCP cobalt cluster and (b) the 55-atom FCC cobalt cluster.

6.1 CO Adsorption on Small Cobalt Clusters

There is an established relationship between cobalt particle size and adsorption and dissociation favourability of carbon monoxide [134]. The optimized geometries of several cobalt particles were presented in Chapter 3. To reiterate, these are 'magic number' clusters generated by iteratively adding nearest neighbors to clusters from a single atom nucleant. Adsorption of CO to several sites on the 55-atom FCC cluster and the 57-atom HCP cluster have been calculated. The optimized structures of the clusters are shown in Figure 6.1.

On each cluster, unique hollow sites were identified by examining the nearest neighbors of the site's Co atoms. The CO atom was placed over the center of the hollow site oriented along the normal of the site's plane. From there the entire structure was allowed to relax.

6.1.1 A Note on the Adsorption Problem in PBE-DFT

It is known that the order of preference of binding sites of small molecules like CO on transition metals found in DFT varies with exchange-correlation functional selection. This was initially introduced as "The CO/Pt(111) Puzzle" [135]. Luo, Zhao, and Truhlar performed a study of the effects of several XC functionals on the predicted

lattice constants, surface formation energies, and CO adsorption energies on several transition metal surfaces [136]. Generally it was demonstrated that a functional could be selected to accurately produce the experimental values for some but not all of these quantities. Two meta-GGAs were reported to perform well in all categories on the selected systems, these being the M06-L functional [137] and RevTPSS [138] (noting that the study was carried out by the group that developed the former). These functionals are not currently available in ONETEP. The only other functional to outperform PBE in CO adsorption energy calculation on average was RPBE [139]. However this improvement was highly material-dependent, for example predicting that CO adsorption on Ag was endothermic, and it performed generally worse than PBE in the other categories, particularly in calculation surface formation energies [136].

Here the PBE functional is used for better comparison with relevant literature results. It is left for future work to explore the effects of XC functional choice on the properties explored here.

6.1.2 55-atom FCC Cluster

The 55-atom FCC cluster exposes two surfaces: (111) and (001). There are two unique hollow sites on the (111) surface and only one on the (001) surface. These are depicted in Figures 6.2a-6.2c. The (111) sites are distinguished by their distance from the edges leading to the (001) surface; one site is on the edge and the other is in the centre of the surface. Each of the hollow sites on the (001) surface are indistinguishable.

In addition to the hollow sites, the FCC cluster was used to demonstrate additional adsorption locations created by the abundance of cluster edges and corners. Figure 6.3a shows a CO molecule adsorbed to the edge between the (111) and (001) surfaces. Figure 6.3b shows a CO molecule adsorbed at the corner between two (111) surfaces and two (001) surfaces.

Table 6.1 shows the adsorption energies E_{ads} of each of the 3 sites shown, as well as literature values for the adsorption energies on each surface of the clean surfaces in the Wulff construction E_{ads}^{Wulff} [50]. It also shows the adsorption energies of the edge and corner sites. CO is found to have a stronger binding to the cluster than to the equivalent Wulff construction surfaces. Additionally, the position on the surface relative to edges between surfaces is significant, with the edge site on the (111) surface having a stronger adsorption energy than the centrally located one. These effects are attributable to the presence of cobalt atoms with more severe under-coordination than would be present on the clean surface, leading to a stronger bond.

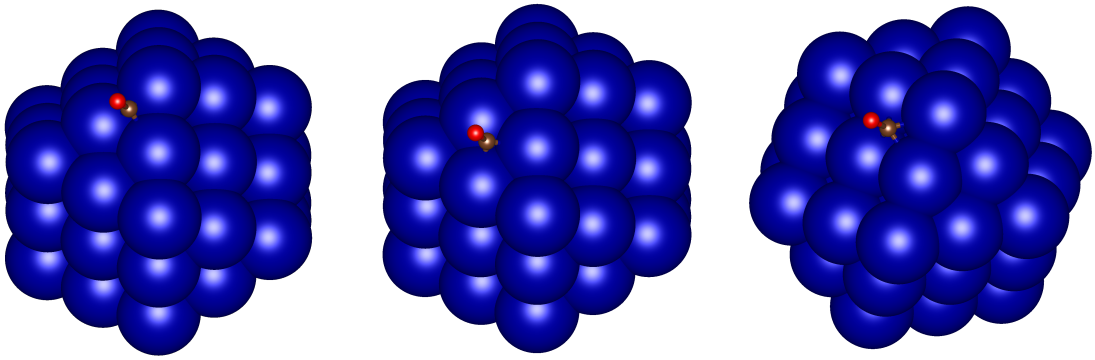

(a) (111) site A (b) (111) site B (c) (001) site A

Fig. 6.2 CO molecule adsorbed to (a, b) the (111) surface and (c) the (001) surface of the 55-atom FCC cobalt cluster.

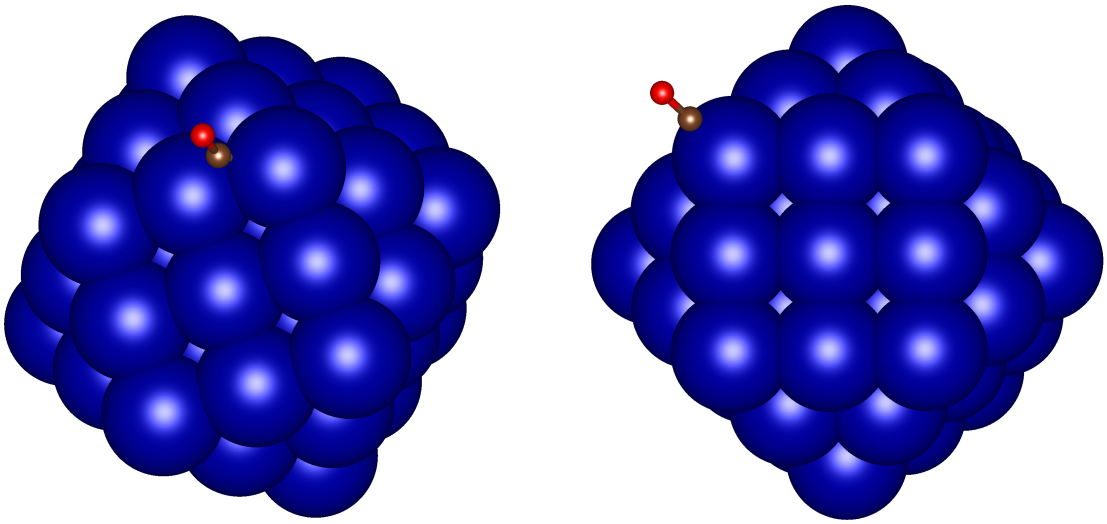

(a) Edge site. (b) Corner site.

Fig. 6.3 CO molecule adsorbed to the (a) edge and (b) corner between the (111) and (001) surfaces of the 55-atom cobalt cluster.

Site	E_{ads} (eV)	E_{ads}^{Wulff} (eV)
(111)A	1.986	1.61
(111)B	1.773	1.61
(001)A	1.769	1.71
Edge	1.905	
Corner	1.855	

Table 6.1 CO hollow site adsorption energies on surfaces of the 55-atom cobalt FCC cluster compared to those on the clean surfaces as reported by Liu *et. al.* [50]

6.1.3 57-atom HCP Cluster

The 57-atom HCP cobalt cluster consisted of several small surfaces with nonequivalent sites. An HCP cluster of this type consists of two (0001) ends and 12 $(10\bar{1}1)$ surfaces connecting them. The $(10\bar{1}1)$ surfaces have alternating 3- and 4-atom hollow sites which give rise to the many possible environments. Figure 6.4 shows the two unique (0001) and two unique four-atom $(10\bar{1}1)$ sites found on this cluster.

Table 6.2 shows the adsorption energies E_{ads} of each of the sites shown, as well as literature values for the adsorption energies on each surface of the clean surfaces in the Wulff construction E_{ads}^{Wulff} [50].

The study used for literature comparison only considered the 4-atom hollow sites on the $(10\bar{1}1)$ surface. The adsorption of the unique three-atom hollow sites on this surface have been examined on the 57-atom cluster to further examine the effects of adsorption environment. Figure 6.5 shows the four unique 3-atom adsorption sites available. Their energies are reported in Table 6.3.

Site	E_{ads} (eV)	E_{ads}^{Wulff} (eV)
(0001)A	1.900	1.64
(0001)B	1.859	1.64
$(10\bar{1}1)$A	1.890	1.85
$(10\bar{1}1)$B	1.707	1.85

Table 6.2 (0001) and 4-atom $(10\bar{1}1)$ hollow site CO adsorption energies on the 57-atom HCP cobalt cluster compared to those on the clean surfaces as reported by Liu *et. al.* [50]

Site	E_{ads} (eV)
$(10\bar{1}1)$C	1.967
$(10\bar{1}1)$D	1.863
$(10\bar{1}1)$E	1.839
$(10\bar{1}1)$F	1.863

Table 6.3 3-atom $(10\bar{1}1)$ adsorption sites found on the 57-atom HCP cobalt cluster

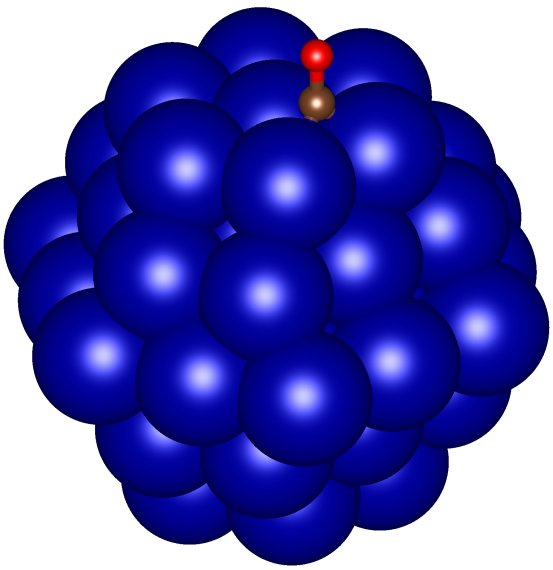

(0001) Site A

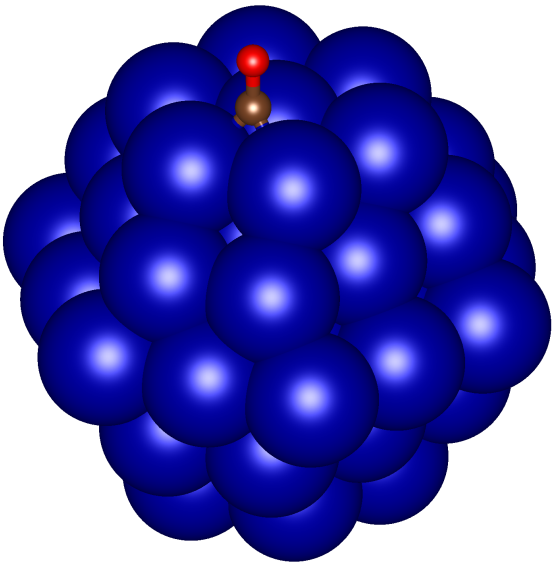

(0001) Site B

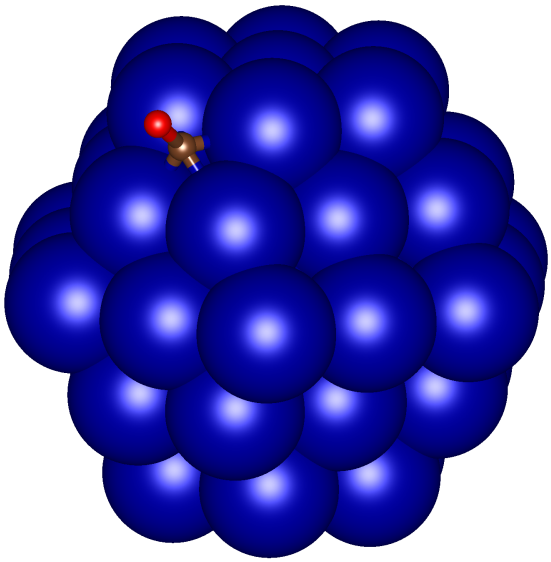

(10$\bar{1}$1) Site A

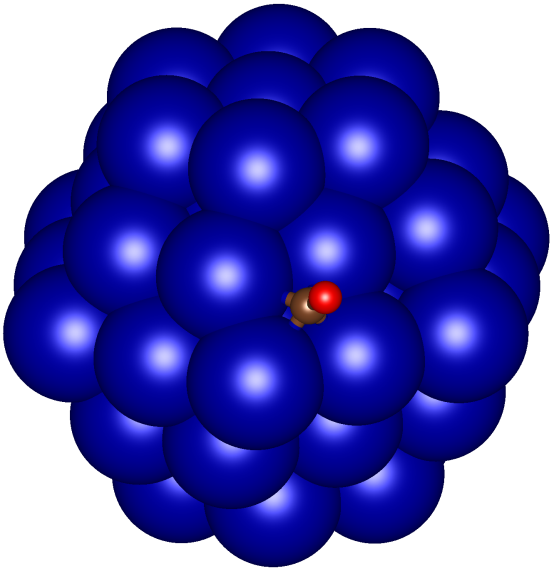

(10$\bar{1}$1) Site B

Fig. 6.4 CO adsorption to the (0001) sites and the 4-atom (10$\bar{1}$1) sites of the 57-atom cobalt cluster

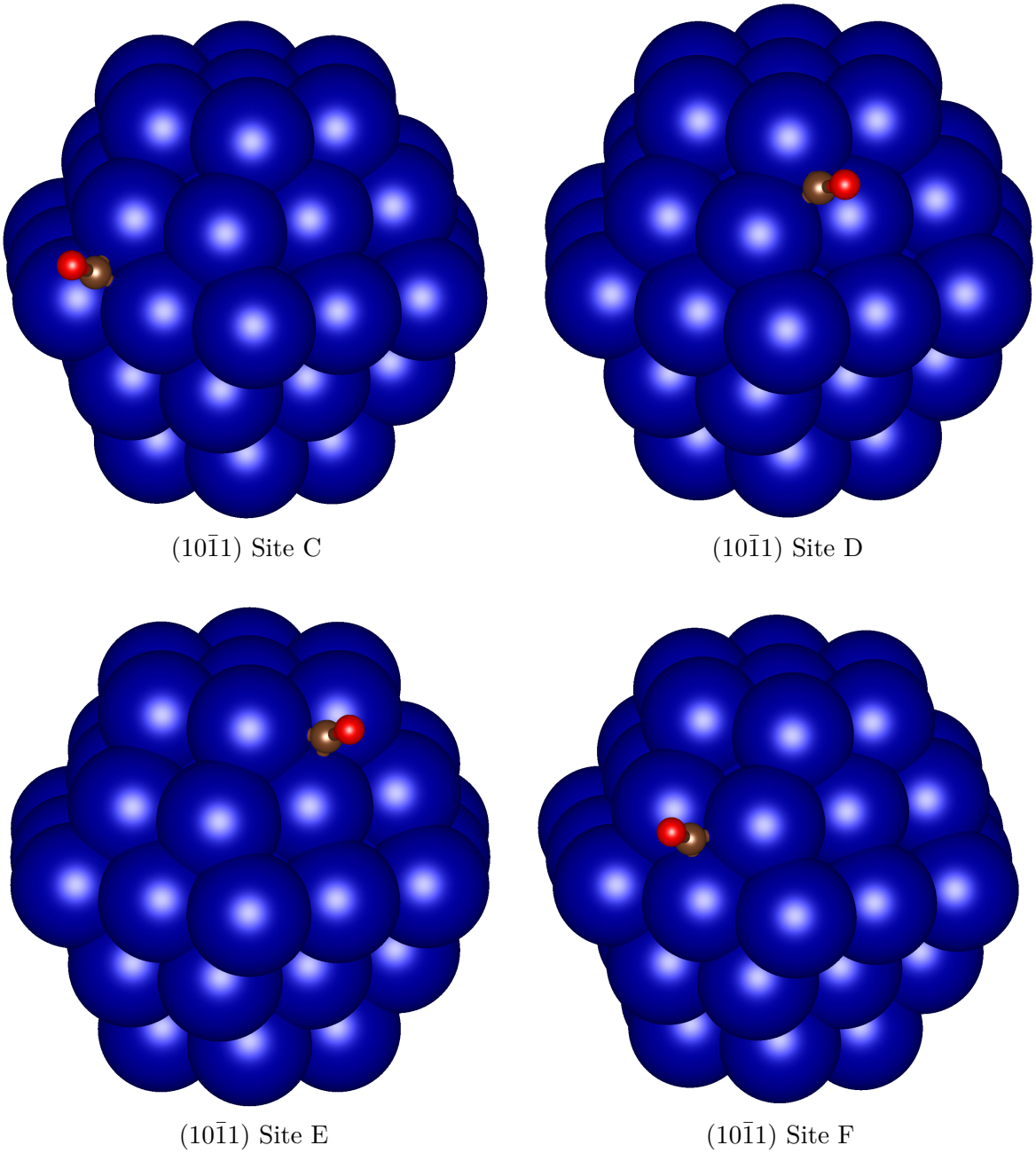

($10\bar{1}1$) Site C ($10\bar{1}1$) Site D

($10\bar{1}1$) Site E ($10\bar{1}1$) Site F

Fig. 6.5 3-atom ($10\bar{1}1$) hollow site CO adsorption energies on the 57-atom HCP cobalt cluster.

6.2 CO Dissociation on Small Cobalt Particles

The 55-atom FCC cobalt cluster was shown to have stronger CO adsorption properties on each surface than on those of a Wulff particle. The presence of edge sites, and their dominance in small clusters like these, may also affect CO dissociation compared to the Wulff construction, and provide new opportunities for dissociation such as paths resulting in the oxygen and carbon atoms adsorbed on different surfaces.

Two pathways for CO dissociation were calculated using NEB and free-spin EDFT, starting from site (111) A (Figure 6.2a) on the 55-atom FCC cluster, where the CO is on a hollow site of the (111) surface. One pathway is dissociation onto the surface, and the other is dissociation over the ridge so the oxygen atom sits on a hollow site of the (100) surface. Simplified depictions of these two pathways that only include movement of the oxygen atom are shown in Figure 6.6.

In addition to the motion of the oxygen, the carbon atom also moved closer into the cluster after dissociation. The average distance from the carbon atom to its neighboring cobalt atoms was 1.975 Å before dissociation, which was reduced to 1.778 Å and 1.765 Å after surface and over-the-ridge dissociation respectively.

Each path was optimized from a linear interpolation, with the climbing image enabled at or near the point at which the path converged. The forward barrier for CO dissociation on the (111) surface of the 55-atom cluster (Figure 6.6a) was found to be 2.223 eV. This can be compared to a literature value of the same pathway on the clean (111) surface of 2.48 eV [50]. The (111)-(001) ridge dissociation pathway (Figure 6.6b) was found to have a forward barrier of 2.578 eV. Both paths are endothermic, with the surface pathway having a reaction energy of 0.493 eV and the ridge pathway having a reaction energy of 0.687 eV. The literature value for the clean (111) surface dissociation reaction energy is 0.73 eV [50]. Figures 6.7 and 6.8 show the energy landscape of the reaction pathways of these two paths as well as the reactant, intermediate, and product structures.

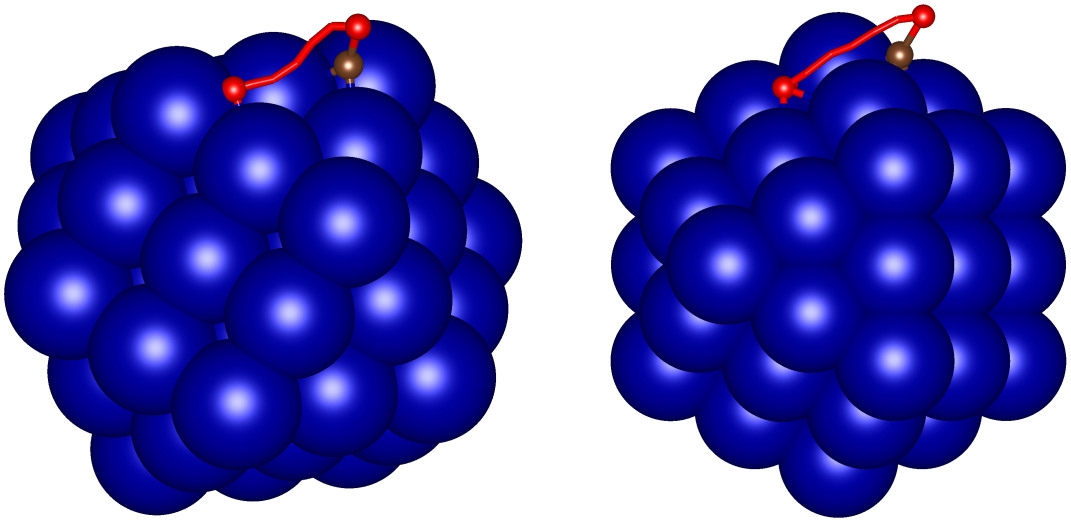

(a) Surface Dissociation (b) Ridge Dissociation

Fig. 6.6 Simplified representations of CO dissociation pathways on the 55-atom FCC cobalt cluster (a) on the (111) surface of the cluster and (b) over the ridge leading to the (001) surface. Motion of the carbon atom and the cluster itself during the transition was non-negligible but is omitted for clarity.

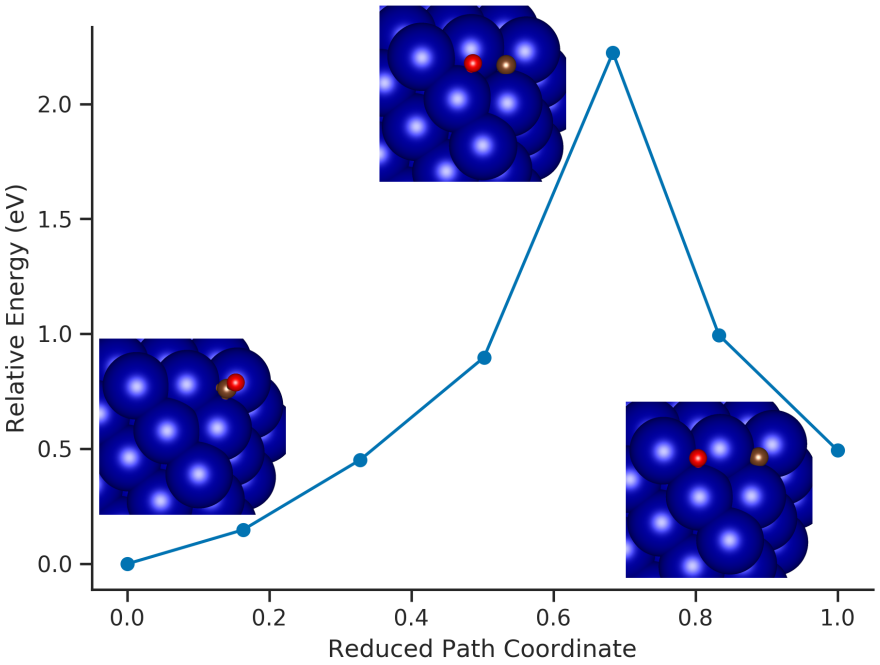

Fig. 6.7 Surface dissociation of CO on the (111) surface of the 55-atom FCC cluster.

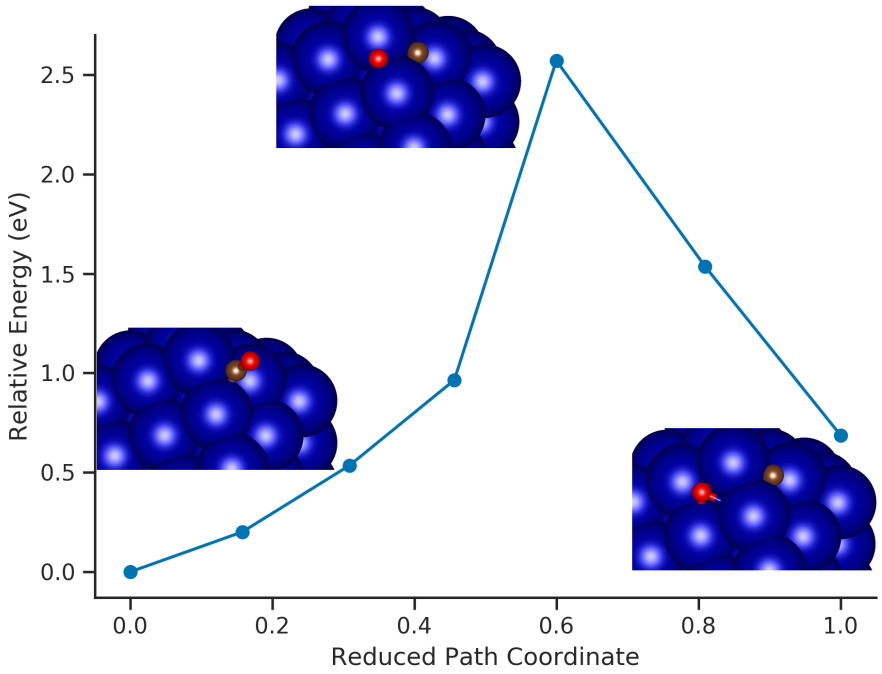

Fig. 6.8 Over-the-ridge dissociation of CO on the (111) surface of the 55-atom FCC cluster, resulting in the oxygen on the (001) surface.

6.3 Discussion

The applications work presented here shows that smaller clusters will have different surface adsorption properties to the Wulff particle limit. CO adsorption to under-coordinated cobalt sites is generally stronger, and both edge and corner sites were also found to be strongly bound. These sites make up an appreciable fraction of the available binding sites of smaller particles, and their stronger adsorption energy is supportive of the experimental finding that smaller particles support CO adsorption [134], though the full range and surface dependence of this effect must be explored on larger particles.

It was discussed in Section 1.5 that CO activation is influenced by local catalyst geometry. Here the FCC (111) surface was selected for an exploration of CO dissociation. While it was found to be relatively inactive on large particles, it is the majority surface on the FCC Wulff construction of cobalt by a large margin [50]. Finding new, more active pathways on inactive surfaces is a significant focus of modern computational work on cobalt-catalysed FT, discussed in Section 1.5. This study found a modest decrease in dissociation energy on the (111) surface of the 55-atom particle compared to that of the clean surface. Additional dissociation pathways involving multiple surfaces are also possible on small particles, though this study found that the over-the-ridge CO

dissociation pathway depositing the oxygen to the (001) surface is about as inactive as surface dissociation on the clean (111) surface. Dissociation on the small particle surface was found to be significantly less endothermic than on the clean surface, as was over-the-ridge dissociation, though to a lesser extent. It should be noted that, while an effort has been made to make these results comparable, some differences in energies may be due in part to different electronic structure approaches.

While these results demonstrate the promise of ONETEP in studying systems of industrial interest, including chemistry on large clusters, there are a number of challenges that still exist to doing this effectively. Most prominently, there is an implementation issue with forces in EDFT while using PAW datasets and reusing NGWFs and the Hamiltonian from a previous geometry iteration. This artificially increases the cost of geometry methods applied to systems like those studied here. While the issue has been determined to be likely relating to the non self-consistent force corrections (analogous to Pulay forces), it had not yet been identified and fixed during the time that these results were generated [1]. There are also a number of functionalities that are currently in development that would compliment these studies. In particular k-point sampling with cylindrical NGWFs could be used in studies of large surface structures such as the nanowire discussed in the next section. Theory embedding techniques [140] and linear-scaling metals methods [118] could be used to study increasingly large and complex systems, now including those with *a priori* unknown magnetic states.

6.4 Further Work

6.4.1 Larger Particles

It is possible that the effects of finite particle size can be seen in much larger particles than the ones studied here. The relationship between particle size and CO adsorption could be strengthened by examining these effects on the 147-atom FCC and 153-atom HCP 'magic number' clusters. Dissociation mechanisms at edges or corners are still relevant at quite large particle sizes and should be explored. Additionally there are a number of other reactions besides adsorbed CO dissociation that are relevant to the

[1] Note: After this thesis had been submitted, this bug is believed to have been identified and fixed by the ONETEP development team.

Fischer–Tropsch process, including side reactions that may lead to carbon deposition or deactivation in other ways.

The direct CO activation pathway explored here is one of many possible paths, and work outlined in Section 1.5 indicates that other mechanisms may cause surfaces that are inactive in the direct route, such as the FCC (111) surface, to become active. In particular, the hydrogen-assisted route and its important first step of H_2 dissociation has been experimentally identified as a potential source of lower activity in catalyst particles smaller than 10 nm [134]. A computational exploration of hydrogen adsorption and dissociation on small particles could provide support and context for the observed lower FT activity of smaller particles.

A strategy for larger particles could be explored where comparable transition states from smaller particles are approximately reproduced on larger particles, and optimized using the dimer method or similar local saddle point searching tools. This has the potential to reduce the cost of the investigation as the entire NEB path does not need to be maintained on larger systems. It should be noted that the dimer method implementation in ONETEP was completed too late to be used in this section.

6.4.2 CO Adsorption on a Cobalt Nanowire

Using free-spin EDFT and transition state tools in ONETEP, mechanisms behind the strong catalyst-support interaction discussed in literature can begin to be investigated directly using predictive simulations. Some work has been done in building one model that could be used for this purpose. Figure 6.9a depicts a cobalt nanowire adsorbed on the anatase (101) surface. The interface was constructed by positioning cobalt atoms directly above the oxygen sites, optimizing the geometry, and then repeatedly adding further layers of cobalt above each surface cobalt layer. This was done in VASP [60–63]. From this procedure a FCC structure quickly emerged, with an interface layer consisting of cobalt vacancies wherever the lattice does not contact an exposed oxygen atom in the anatase surface, resulting in a ¾ layer. A model of this interface is shown in Figure 6.9b. Based on an FCC lattice constant of 3.537 Å [141], the strain in the periodic direction is estimated to be about 3.45%. Using this model, particularly once extended NGWFs and k-point sampling are available in ONETEP, it would be possible to examine the adsorption and dissociation properties of CO as a function of distance from the support surface.

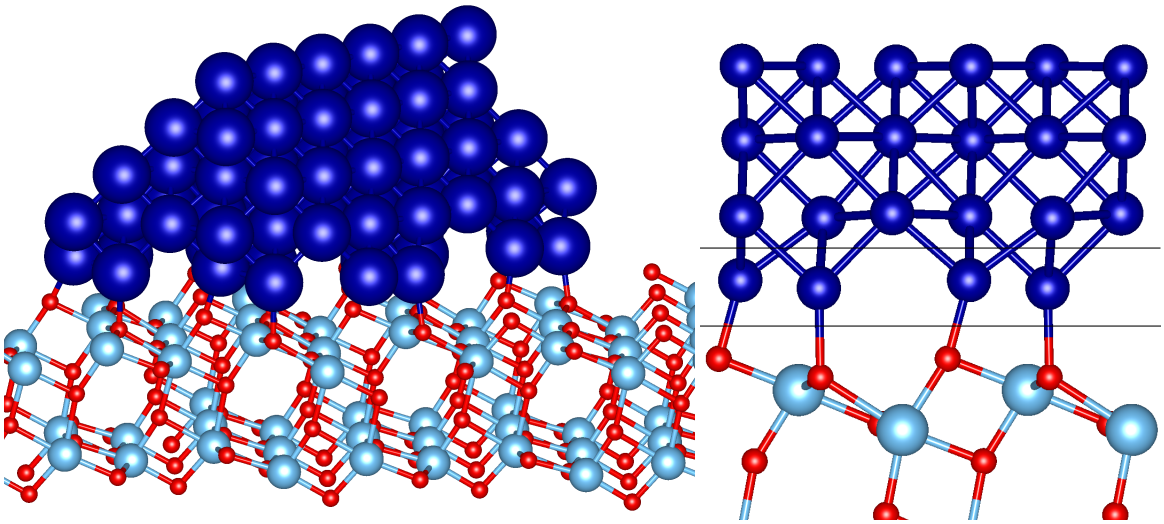

(a) Nanowire (b) Interface

Fig. 6.9 (a) Cobalt nanowire adsorbed to the anatase (101) surface studied in Chapter 5. The structure is a FCC cobalt lattice, with a (111) surface exposed, and a (100) surface facing the TiO_2 support. (b) Diagram of the interface from which the nanowire was cleaved. This shows the interface layer quickly transitioning into bulk-like FCC.

Chapter 7

Conclusion

Summary

Understanding the mechanisms behind Fischer-Tropsch catalyst activity and deactivation with predictive computational models can inform better reactor design and control, and can provide support for experimental findings. This thesis presents new tools developed for the linear-scaling DFT code ONETEP [57, 58] that makes more of these models feasible, as well as studies performed using both traditional and linear-scaling DFT into how carbon monoxide can interact with a cobalt catalyst.

Chapter 3 outlines new metals functionality added to ONETEP, namely free-spin EDFT and non-integer net spin EDFT. This allows for more accurate simulations of metallic systems in general, relieving the constraint of fixed spin on the ensemble of systems simulated and requiring less prior knowledge of new systems. It was demonstrated that using this functionality bulk properties of ferromagnetic materials can be explored predictively. Additionally, a relationship between the size of cobalt particles and their net spin was established, based on the results of calculations of the magnetic properties of clusters ranging in size from 1 to 153 atoms. This relationship was further demonstrated to be attributable to the surface area to volume ratio of the clusters, with external atoms with fewer neighbours carrying a higher individual net spin.

Transition state searching tools added to ONETEP are described in Chapter 4. These include the nudged elastic band and dimer methods. The former offers a robust sampling of the minimum energy path connecting two endpoints as well as functionality to explicitly locate the transition state. The latter makes no reference to initial or final states but freely searches for nearby saddle points, and is currently intended

to be a transition state refinement tool that is less expensive than NEB's climbing image functionality. Both of these methods also make use of new communications infrastructure for coordinated simulations in ONETEP, and use a new modern geometry optimizer with several new optimization algorithms available that may offer improved performance.

Chapter 5 explores some of the surface chemistry of support-adsorbed cobalt in a Co/TiO_2 reactor environment. This study was carried out with the plane-wave DFT code VASP [60–63]. It was established that gas-phase species present in the reactor could bind to surface-adsorbed cobalt, and that this could strongly affect its adsorption and surface mobility properties. In particular large, highly mobile cobalt carbonyls were found to form favourably under reactor conditions, including on a hydrated surface. As carbon monoxide is a reactant in the Fischer-Tropsch process this may be relevant to the lifetime of the catalyst. Experiment has also indicated that this mechanism may contribute to ripening [44, 46, 47].

Chapter 6 presents early applications work with the new functionality developed in ONETEP. The adsorption of CO to small cobalt particles was investigated, and it was generally found that adsorption on the small particles was stronger than adsorption on clean cobalt surfaces. Additionally, two CO dissociation pathways were explored, one on a surface of the particle and one over the ridge between two surfaces. The rate of dissociation on this particle surface may be modestly favourable compared to that of the clean surface, and the reactions are notably less endothermic.

Closing Remarks

Understanding the conditions that may affect the mobility of atomic cobalt on the support surface is one piece of the large puzzle of reactor design and control for the Fischer-Tropsch process. It has been demonstrated here that carbon monoxide binds highly favourably to support-adsorbed cobalt to produce weakly bound and highly mobile carbonyl species. The properties of surface-adsorbed atomic cobalt can help inform an understanding of ripening, which fits into the larger picture of catalyst deactivation.

The investigations into CO adsorption and activation on small cobalt particles presented here may be a first step in theoretical support for experimental observations that small catalyst particles favour CO adsorption. They also provide examples of the kinds of studies that can now be performed with ONETEP. Further studies like these can provide insight into Fischer-Tropsch chemistry on increasingly complex structures, including those provided by experimental imaging [59].

The new functionality described in this thesis will make ONETEP a promising candidate for studying chemistry related to catalytic reactions on large and low-periodicity systems, especially when coupled with other recent and ongoing developments in the code. Together with new linear scaling metals techniques [142, 118], predictive studies of ferromagnetic systems into the thousands and even tens of thousands of atoms become feasible. Furthermore, theory embedding methods that treat a single simulation with multiple levels of theory [143, 140] could potentially be used to treat insulating parts of the system with favourable LS-DFT methods. Finally, spin-dependent NGWFs that provide more variational freedom may improve the quality of simulations of ferromagnetic systems.

References

[1] A. Y. Khodakov, W. Chu, and P. Fongarland, "Advances in the development of novel cobalt Fischer-Tropsch catalysts for synthesis of long-chain hydrocarbons and clean fuels.," *Chemical reviews*, vol. 107, pp. 1692–744, 5 2007.

[2] M. J. Tijmensen, A. P. Faaij, C. N. Hamelinck, and M. R. van Hardeveld, "Exploration of the possibilities for production of Fischer Tropsch liquids and power via biomass gasification," *Biomass and Bioenergy*, vol. 23, pp. 129–152, aug 2002.

[3] K. Göransson, U. Söderlind, J. He, and W. Zhang, "Review of syngas production via biomass DFBGs," *Renewable and Sustainable Energy Reviews*, vol. 15, no. 1, pp. 482–492, 2011.

[4] M. McGrath, "Climate change: 'Magic bullet' carbon solution takes big step." Available at https://www.bbc.co.uk/news/science-environment-47638586.

[5] P. Sabatier and J. B. Senderens, "New methane synthesis," *C. R. Acad. Sci.*, vol. 134, p. 514, 1902.

[6] V. Navarro, M. A. Van Spronsen, and J. W. Frenken, "In situ observation of self-assembled hydrocarbon Fischer-Tropsch products on a cobalt catalyst," *Nature Chemistry*, vol. 8, no. 10, 2016.

[7] C. H. Bartholomew, "Recent technological developments in Fischer-Tropsch catalysis," *Catalysis Letters*, vol. 7, no. 1-4, pp. 303–315, 1991.

[8] A. de Klerk, "Fischer-Tropsch Process," in *Kirk-Othmer Encyclopedia of Chemical Technology*, pp. 1–20, Hoboken, NJ, USA: John Wiley & Sons, Inc., jan 2013.

[9] D. L. King, J. A. Cusumano, and R. L. Garten, "A Technological Perspective for Catalytic Processes Based on Synthesis Gas," *Catalysis Reviews*, vol. 23, pp. 233–263, jan 1981.

[10] M. Vannice, "The catalytic synthesis of hydrocarbons from H2/CO mixtures over the group VIII metals II. The kinetics of the methanation reaction over supported metals," *Journal of Catalysis*, vol. 37, pp. 462–473, 6 1975.

[11] N. Bungane, C. Welker, E. Van Steen, J. R. Moss, and M. Claeys, "Fischer-Tropsch CO-Hydrogenation on SiO2-supported Osmium Complexes," *Verlag der Zeitschrift für Naturforschung*, vol. 63b, pp. 289–292, 2008.

[12] B. C. Enger and A. Holmen, "Nickel and Fischer-Tropsch Synthesis," *Catalysis Reviews*, vol. 54, pp. 437–488, oct 2012.

[13] B. Jager and R. Espinoza, "Advances in low temperature Fischer-Tropsch synthesis," *Catalysis Today*, vol. 23, pp. 17–28, jan 1995.

[14] R. Espinoza, A. Steynberg, B. Jager, and A. Vosloo, "Low temperature Fischer–Tropsch synthesis from a Sasol perspective," *Applied Catalysis A: General*, vol. 186, pp. 13–26, oct 1999.

[15] M. E. Dry, "The Fischer–Tropsch process: 1950–2000," *Catalysis Today*, vol. 71, pp. 227–241, jan 2002.

[16] S. Bessell, "Support effects in cobalt-based fischer-tropsch catalysis," *Applied Catalysis A: General*, vol. 96, pp. 253–268, mar 1993.

[17] C. H. Bartholomew and R. C. Reuel, "Cobalt-support interactions: their effects on adsorption and carbon monoxide hydrogenation activity and selectivity properties," *Industrial & Engineering Chemistry Product Research and Development*, vol. 24, pp. 56–61, 3 1985.

[18] S. J. Tauster, S. C. Fung, and R. L. Garten, "Strong metal-support interactions. Group 8 noble metals supported on TiO2," *Journal of the American Chemical Society*, vol. 100, 1978.

[19] S. J. Tauster, S. C. Fung, R. T. K. Baker, and J. A. Horsley, "Strong Interactions in Supported-Metal Catalysts," *Science*, vol. 211, no. 4487, pp. 1121–1125, 1981.

[20] S. Storsæter, B. Tøtdal, J. C. Walmsley, B. S. Tanem, and A. Holmen, "Characterization of alumina-, silica-, and titania-supported cobalt Fischer-Tropsch catalysts," *Journal of Catalysis*, vol. 236, pp. 139–152, nov 2005.

[21] B. Jongsomjit, C. Sakdamnuson, and P. Praserthdam, "Dependence of crystalline phases in titania on catalytic properties during CO hydrogenation of Co/TiO2 catalysts," *Materials Chemistry and Physics*, vol. 89, pp. 395–401, feb 2005.

[22] M. Vannice and R. Garten, "Metal-support effects on the activity and selectivity of Ni catalysts in COH2 synthesis reactions," *Journal of Catalysis*, vol. 56, pp. 236–248, feb 1979.

[23] C. H. Bartholomew, R. B. Pannell, J. L. Butler, and D. G. Mustard, "Nickel-support interactions: their effects on particle morphology, adsorption, and activity selectivity properties," *Industrial & Engineering Chemistry Product Research and Development*, vol. 20, pp. 296–300, jun 1981.

[24] R. C. Reuel and C. H. Bartholomew, "Effects of support and dispersion on the CO hydrogenation activity/selectivity properties of cobalt," *Journal of Catalysis*, vol. 85, pp. 78–88, jan 1984.

[25] K. I. Hadjiivanov and D. G. Klissurski, "Surface chemistry of titania (anatase) and titania-supported catalysts," *Chemical Society Reviews*, vol. 25, no. 1, p. 61, 1996.

[26] M. Lazzeri, A. Vittadini, and A. Selloni, "Structure and energetics of stoichiometric TiO2 anatase surfaces," *Physical Review B*, vol. 63, p. 155409, mar 2001.

[27] Y. Li, Y. Fan, H. Yang, B. Xu, L. Feng, M. Yang, and Y. Chen, "Strong metal-support interaction and catalytic properties of anatase and rutile supported palladium catalyst Pd/TiO2," *Chemical Physics Letters*, vol. 372, pp. 160–165, apr 2003.

[28] G. Wulff, "On the question of the rate of growth and dissolution of crystal surfaces," *Z Kristallogr Miner*, vol. 34, pp. 449–530, 1901.

[29] P. J. Van Berge, J. Van De Loosdrecht, and J. L. Visagie, "Cobalt catalysts," 2004.

[30] N. E. Tsakoumis, M. Rønning, Ø. Borg, E. Rytter, and A. Holmen, "Deactivation of cobalt based Fischer–Tropsch catalysts: A review," *Catalysis Today*, vol. 154, no. 3, pp. 162–182, 2010.

[31] C. H. Bartholomew and R. M. Bowman, "Sulfur poisoning of cobalt and iron fischer-tropsch catalysts," *Applied Catalysis*, vol. 15, pp. 59–67, 3 1985.

[32] C. G. Visconti, L. Lietti, P. Forzatti, and R. Zennaro, "Fischer–Tropsch synthesis on sulphur poisoned Co/Al2O3 catalyst," *Applied Catalysis A: General*, vol. 330, pp. 49–56, 10 2007.

[33] P. Menon, "Coke on catalysts-harmful, harmless, invisible and beneficial types," *Journal of Molecular Catalysis*, vol. 59, pp. 207–220, 4 1990.

[34] J. C. W. Swart, I. M. Ciobícă, R. A. v. Santen, and E. v. Steen, "Intermediates in the Formation of Graphitic Carbon on a Flat FCC-Co(111) Surface," 2008.

[35] J. C. W. Swart, E. van Steen, I. M. Ciobícă, R. A. van Santen, P. G. Menon, C. H. Bartholomew, M. E. Dry, J. A. Moulijn, A. E. v. Diepen, and F. Kapteijn, "Interaction of graphene with FCC–Co(111)," *Phys. Chem. Chem. Phys.*, vol. 11, no. 5, pp. 803–807, 2009.

[36] O. Ducreux, J. Lynch, B. Rebours, M. Roy, and P. Chaumette, "In Situ Characterisation of Cobalt Based Fischer-Tropsch Catalysts : A New Approach to the Active Phase," in *Studies in Surface Science and Catalysis*, vol. 119, pp. 125–130, 1998.

[37] E. Van Steen, M. Claeys, M. E. Dry, J. Van De Loosdrecht, E. L. Viljoen, and J. L. Visagie, "Stability of Nanocrystals: Thermodynamic Analysis of Oxidation and Re-reduction of Cobalt in Water/Hydrogen Mixtures," *Journal of Physical Chemistry B*, vol. 109, no. 8, pp. 3575–3577, 2005.

[38] M. Rothaemel, K. F. Hanssen, E. A. Blekkan, D. Schanke, and A. Holmen, "The effect of water on cobalt Fischer-Tropsch catalysts studied by steady-state isotopic transient kinetic analysis (SSITKA)," *Catalysis Today*, vol. 38, pp. 79–84, 10 1997.

[39] A. Hilmen, D. Schanke, K. Hanssen, and A. Holmen, "Study of the effect of water on alumina supported cobalt Fischer–Tropsch catalysts," *Applied Catalysis A: General*, vol. 186, no. 1, pp. 169–188, 1999.

[40] A. Hilmen, D. Schanke, and A. Holmen, "Reoxidation of supported cobalt Fischer-Tropsch catalysts," *Studies in Surface Science and Catalysis*, vol. 107, pp. 237–242, 1997.

[41] R. Meyer, Q. Ge, J. Lockemeyer, R. Yeates, M. Lemanski, D. Reinalda, and M. Neurock, "An ab initio analysis of adsorption and diffusion of silver atoms on alumina surfaces," *Surface Science*, vol. 601, no. 1, pp. 134–145, 2007.

[42] G. B. Hoflund and D. M. Minahan, "Study of Cs-Promoted , α-Alumina-Supported Silver , Ethylene-Epoxidation Catalysts," *Journal of Catalysis*, vol. 162, pp. 48–53, 1996.

[43] E. Rytter and A. Holmen, "Deactivation and Regeneration of Commercial Type Fischer-Tropsch Co-Catalysts - A Mini-Review," *Catalysts*, vol. 5, no. 2, pp. 478–499, 2015.

[44] D. Kistamurthy, A. Saib, D. Moodley, J. Niemantsverdriet, and C. Weststrate, "Ostwald ripening on a planar Co/SiO2 catalyst exposed to model Fischer-Tropsch synthesis conditions," *J. Catal.*, vol. 328, pp. 123–129, aug 2015.

[45] C. E. Kliewer, S. L. Soled, and G. Kiss, "Morphological transformations during Fischer-Tropsch synthesis on a titania-supported cobalt catalyst," *Catalysis Today*, pp. 233–256, feb 2019.

[46] M. Claeys, M. E. Dry, E. van Steen, P. J. van Berge, S. Booyens, R. Crous, P. van Helden, J. Labuschagne, D. J. Moodley, and A. M. Saib, "Impact of Process Conditions on the Sintering Behavior of an Alumina-Supported Cobalt Fischer–Tropsch Catalyst Studied with an in Situ Magnetometer," *ACS Catalysis*, vol. 5, no. 2, pp. 841–852, 2015.

[47] J. Wilson and C. de Groot, "Atomic-Scale Restructuring in High-Pressure Catalysis," *The Journal of Physical Chemistry*, vol. 99, pp. 7860–7866, may 1995.

[48] W. Shen, J. Dumesic, and C. Hill, "Criteria for stable Ni particle size under methanation reaction conditions: Nickel transport and particle size growth via nickel carbonyl," *Journal of Catalysis*, vol. 68, pp. 152–165, mar 1981.

[49] A. Saib, D. Moodley, I. Ciobîcă, M. Hauman, B. Sigwebela, C. Weststrate, J. Niemantsverdriet, and J. van de Loosdrecht, "Fundamental understanding of deactivation and regeneration of cobalt Fischer–Tropsch synthesis catalysts," *Catalysis Today*, vol. 154, no. 3, pp. 271–282, 2010.

[50] J.-X. Liu, H.-Y. Su, D.-P. Sun, B.-Y. Zhang, and W.-X. Li, "Crystallographic Dependence of CO Activation on Cobalt Catalysts: HCP versus FCC," *Journal of the American Chemical Society*, vol. 135, pp. 16284–16287, nov 2013.

[51] Q. Ge and M. Neurock, "Adsorption and Activation of CO over Flat and Stepped Co Surfaces: A First Principles Analysis," *The Journal of Physical Chemistry B*, vol. 110, no. 31, pp. 15368–15380, 2006.

[52] C.-F. Huo, Y.-W. Li, J. Wang, and H. Jiao, "Adsorption and Dissociation of CO as Well as CHx Coupling and Hydrogenation on the Clean and Oxygen Pre-covered Co(0001) Surfaces," *The Journal of Physical Chemistry C*, vol. 112, no. 10, pp. 3840–3848, 2008.

[53] O. R. Inderwildi, S. J. Jenkins, and D. A. King, "Fischer-Tropsch Mechanism Revisited: Alternative Pathways for the Production of Higher Hydrocarbons from Synthesis Gas," *The Journal of Physical Chemistry C*, vol. 112, no. 5, pp. 1305–1307, 2008.

[54] M. Zhuo, K. F. Tan, A. Borgna, and M. Saeys, "Density Functional Theory Study of the CO Insertion Mechanism for Fischer-Tropsch Synthesis over Co Catalysts," *The Journal of Physical Chemistry C*, vol. 113, no. 19, pp. 8357–8365, 2009.

[55] L. Joos, I. A. W. Filot, S. Cottenier, E. J. M. Hensen, M. Waroquier, V. Van Speybroeck, and R. A. van Santen, "Reactivity of CO on Carbon-Covered Cobalt Surfaces in Fischer–Tropsch Synthesis," *The Journal of Physical Chemistry C*, vol. 118, pp. 5317–5327, mar 2014.

[56] A. Banerjee, A. P. van Bavel, H. P. C. E. Kuipers, and M. Saeys, "CO Activation on Realistic Cobalt Surfaces: Kinetic Role of Hydrogen," *ACS Catalysis*, vol. 7, pp. 5289–5293, aug 2017.

[57] C.-K. Skylaris, P. D. Haynes, A. a. Mostofi, and M. C. Payne, "Introducing ONETEP: Linear-scaling density functional simulations on parallel computers," *Journal of Chemical Physics*, vol. 122, no. 8, 2005.

[58] N. D. M. Hine, M. Robinson, P. D. Haynes, C.-K. Skylaris, M. C. Payne, and A. A. Mostofi, "Accurate ionic forces and geometry optimization in linear-scaling density-functional theory with local orbitals," *Physical Review B*, vol. 83, p. 195102, may 2011.

[59] J. Aarons, L. Jones, A. Varambhia, K. E. MacArthur, D. Ozkaya, M. Sarwar, C.-K. Skylaris, and P. D. Nellist, "Predicting the Oxygen-Binding Properties of Platinum Nanoparticle Ensembles by Combining High-Precision Electron Microscopy and Density Functional Theory," *Nano Letters*, vol. 17, pp. 4003–4012, jul 2017.

[60] G. Kresse and J. Hafner, "Ab initio molecular dynamics for liquid metals.," *Physical review. B, Condensed matter*, vol. 47, pp. 558–561, 1 1993.

[61] G. Kresse and J. Furthmüller, "Efficient iterative schemes for ab initio total-energy calculations using a plane-wave basis set," *Physical review. B, Condensed matter*, vol. 54, pp. 11169–11186, 10 1996.

[62] G. Kresse and J. Furthmüller, "Efficiency of Ab-Initio Total Energy Calculations for Metals and Semiconductors Using a Plane-Wave Basis Set," *Computational Materials Science*, vol. 6, pp. 15–50, jul 1996.

[63] G. Kresse and D. Joubert, "From ultrasoft pseudopotentials to the projector augmented-wave method," *Physical review. B, Condensed matter*, vol. 59, no. 3, pp. 1758–1775, 1999.

[64] R. D. King-Smith, M. C. Payne, and J. S. Lin, "Real-space implementation of nonlocal pseudopotentials for first-principles total-energy calculations," *Physical Review B*, vol. 44, pp. 13063–13066, dec 1991.

[65] R. M. Martin, *Electronic Structure*. Cambridge University Press, 2004.

[66] P. Hohenberg and W. Kohn, "Inhomogeneous Electron Gas," *Physical Review*, vol. 136, pp. B864–B871, 11 1964.

[67] J. Lehtomäki, I. Makkonen, M. A. Caro, A. Harju, and O. Lopez-Acevedo, "Orbital-free density functional theory implementation with the projector augmented-wave method," *The Journal of Chemical Physics*, vol. 141, p. 234102, dec 2014.

[68] W. Kohn and L. J. Sham, "Self-Consistent Equations Including Exchange and Correlation Effects," *Physical Review*, vol. 140, pp. A1133–A1138, 11 1965.

[69] M. C. Payne, M. P. Teter, D. C. Allan, T. A. Arias, and J. D. Joannopoulos, "Iterative minimization techniques for ab initio total-energy calculations: molecular dynamics and conjugate gradients," *Reviews of Modern Physics*, vol. 64, pp. 1045–1097, 10 1992.

[70] J. D. Pack and H. J. Monkhorst, "Special points for Brillouin-zone integrations," *Physical Review B*, vol. 16, no. 4, pp. 1748–1749, 1977.

[71] P. D. Haynes, C.-K. Skylaris, A. A. Mostofi, and M. C. Payne, "Density kernel optimization in the ONETEP code," *J. Phys.: Condens. Matter*, vol. 20, pp. 294207–7, 2008.

[72] R. Baer and M. Head-Gordon, "Sparsity of the Density Matrix in Kohn-Sham Density Functional Theory and an Assessment of Linear System-Size Scaling Methods," *Physical Review Letters*, vol. 79, pp. 3962–3965, 11 1997.

[73] L. He and D. Vanderbilt, "Exponential Decay Properties of Wannier Functions and Related Quantities," *Physical Review Letters*, vol. 86, pp. 5341–5344, 6 2001.

[74] S. Ismail-Beigi and T. A. Arias, "Locality of the Density Matrix in Metals, Semiconductors, and Insulators," *Physical Review Letters*, vol. 82, pp. 2127–2130, 3 1999.

[75] J. M. Soler, E. Artacho, J. D. Gale, A. García, J. Junquera, P. Ordejón, and D. Sánchez-Portal, "The SIESTA method for ab initio order- N materials simulation," *Journal of Physics: Condensed Matter*, vol. 14, pp. 2745–2779, 3 2002.

[76] P. D. Haynes, C.-K. Skylaris, A. A. Mostofi, and M. C. Payne, "ONETEP: linear-scaling density-functional theory with plane waves," *Psi-k Newsletter*, no. 72, pp. 78–91, 2005.

[77] C.-K. K. Skylaris, A. A. Mostofi, P. D. Haynes, O. Dieguez, M. C. Payne, O. Diéguez, and M. C. Payne, "Nonorthogonal generalized Wannier function pseudopotential plane-wave method," *Physical Review B*, vol. 66, p. 035119, 2002.

[78] "4-Methyl-1-pentene." Available at http://openmopac.net/PM7_accuracy/data_molecules/4-methyl-1-pentene_jmol.html, 2019.

[79] P. D. Haynes, C.-K. Skylaris, A. A. Mostofi, and M. C. Payne, "ONETEP: linear-scaling density-functional theory with local orbitals and plane waves," *Physica Status Solidi (B)*, vol. 243, pp. 2489–2499, sep 2006.

[80] C.-K. Skylaris, A. A. Mostofi, P. D. Haynes, C. J. Pickard, and M. C. Payne, "Accurate kinetic energy evaluation in electronic structure calculations with localized functions on real space grids," *Computer Physics Communications*, vol. 140, pp. 315–322, 11 2001.

[81] J. M. Millam and G. E. Scuseria, "Linear scaling conjugate gradient density matrix search as an alternative to diagonalization for first principles electronic structure calculations," *The Journal of Chemical Physics*, vol. 106, no. 13, p. 5569, 1997.

[82] C.-K. Skylaris and P. D. Haynes, "Achieving plane wave accuracy in linear-scaling density functional theory applied to periodic systems: a case study on crystalline silicon," 2007.

[83] P. Schwerdtfeger, "The Pseudopotential Approximation in Electronic Structure Theory," *ChemPhysChem*, vol. 12, pp. 3143–3155, dec 2011.

[84] D. R. Hamann, M. Schlüter, and C. Chiang, "Norm-Conserving Pseudopotentials," *Physical Review Letters*, vol. 43, pp. 1494–1497, nov 1979.

[85] D. Vanderbilt, "Soft self-consistent pseudopotentials in a generalized eigenvalue formalism," *Physical Review B*, vol. 41, pp. 7892–7895, apr 1990.

[86] P. E. Blöchl, "Projector augmented-wave method," *Physical Review B*, vol. 50, pp. 17953–17979, 12 1994.

[87] N. D. M. Hine, "Linear-scaling density functional theory using the projector augmented wave method," *Journal of Physics: Condensed Matter*, vol. 29, p. 024001, jan 2017.

[88] M. Torrent, F. Jollet, F. Bottin, G. Zérah, and X. Gonze, "Implementation of the projector augmented-wave method in the ABINIT code: Application to the study of iron under pressure," *Computational Materials Science*, vol. 42, pp. 337–351, apr 2008.

[89] N. D. Mermin, "Thermal Properties of the Inhomogeneous Electron Gas," *Physical Review*, vol. 137, pp. A1441–A1443, mar 1965.

[90] R. Warren and B. Dunlap, "Fractional occupation numbers and density functional energy gradients within the linear combination of Gaussian-type orbitals approach," *Chemical Physics Letters*, vol. 262, pp. 384–392, nov 1996.

[91] M. Finnis, A. Lozovoi, and A. Alavi, "The Oxidation of NiAl: What Can We Learn from Ab Initio Calculations?," *Annu. Rev. Mater. Res.*, vol. 35, pp. 167–207, aug 2005.

[92] N. D. M. Hine, K. Frensch, W. M. C. Foulkes, and M. W. Finnis, "Supercell Size Scaling of Density Functional Theory Formation Energies of Charged Defects," *Phys. Rev. B*, vol. 79, p. 024112, jan 2009.

[93] R. P. Feynman, "Forces in Molecules," *Physical Review*, vol. 56, pp. 340–343, 8 1939.

[94] W. Quapp and D. Heidrich, "Analysis of the concept of minimum energy path on the potential energy surface of chemically reacting systems," *Theoretica Chimica Acta*, vol. 66, no. 3-4, pp. 245–260, 1984.

[95] T. A. Halgren and W. N. Lipscomb, "The synchronous-transit method for determining reaction pathways and locating molecular transition states," *Chemical Physics Letters*, vol. 49, pp. 225–232, 7 1977.

[96] N. Govind, M. Petersen, G. Fitzgerald, D. King-Smith, and J. Andzelm, "A generalized synchronous transit method for transition state location," *Computational Materials Science*, vol. 28, no. 2, pp. 250–258, 2003.

[97] K. Müller and L. D. Brown, "Location of saddle points and minimum energy paths by a constrained simplex optimization procedure," *Theoretica Chimica Acta*, vol. 53, no. 1, pp. 75–93, 1979.

[98] H. Jónsson, G. Mills, and K. W. Jacobsen, "Nudged elastic band method for finding minimum energy paths of transitions," in *Classical and Quantum Dynamics in Condensed Phase Simulations*, pp. 385–404, 1997.

[99] G. Henkelman, B. P. Uberuaga, and H. Jónsson, "Climbing image nudged elastic band method for finding saddle points and minimum energy paths," *Journal of Chemical Physics*, vol. 113, no. 22, pp. 9901–9904, 2000.

[100] J. W. Moore and R. G. Pearson, "Elementary Processes: Potential Energy Surfaces and Transition-State Theory," in *Kinetics and Mechanism*, pp. 137–191, John Wiley & Sons, 3 ed., 1981.

[101] K. K. B. Duff, "Density Functional Theory Studies of Cobalt Catalyst Ripening on TiO2 Support for Fischer-Tropsch Reactions," 2015.

[102] G. Henkelman and H. Jónsson, "Improved tangent estimate in the nudged elastic band method for finding minimum energy paths and saddle points," *The Journal of Chemical Physics*, vol. 113, no. 22, p. 9978, 2000.

[103] D. Sheppard, R. Terrell, and G. Henkelman, "Optimization methods for finding minimum energy paths," *The Journal of Chemical Physics*, vol. 128, 2008.

[104] D. C. Liu and J. Nocedal, "On the limited memory BFGS method for large scale optimization," *Mathematical Programming*, vol. 45, pp. 503–528, 8 1989.

[105] H. Jónsson, G. Mills, and K. W. Jacobsen, *Classical and Quantum Dynamics in Condensed Phase Simulations*. Singapore: World Scientific, 1998.

[106] E. Bitzek, P. Koskinen, F. Gähler, M. Moseler, and P. Gumbsch, "Structural relaxation made simple," *Phys. Rev. Lett.*, vol. 97, p. 170201, Oct 2006.

[107] R. Fletcher, *Practical methods of optimization*. New York: John Wiley & Sons, 2 ed., 1987.

[108] S. A. Trygubenko and D. J. Wales, "A doubly nudged elastic band method for finding transition states," *The Journal of Chemical Physics*, vol. 120, pp. 2082–2094, feb 2004.

[109] W. E, W. Ren, and E. Vanden-Eijnden, "String method for the study of rare events," *Physical Review B*, vol. 66, p. 052301, 8 2002.

[110] R. A. Olsen, G. J. Kroes, G. Henkelman, A. Arnaldsson, and H. Jónsson, "Comparison of methods for finding saddle points without knowledge of the final states," *The Journal of Chemical Physics*, vol. 121, pp. 9776–9792, nov 2004.

[111] G. Henkelman and H. Jónsson, "A dimer method for finding saddle points on high dimensional potential surfaces using only first derivatives," *The Journal of Chemical Physics*, vol. 111, pp. 7010–7022, oct 1999.

[112] R. Malek and N. Mousseau, "Dynamics of Lennard-Jones clusters: A characterization of the activation-relaxation technique," *Physical Review E*, vol. 62, pp. 7723–7728, dec 2000.

[113] C. J. Cerjan and W. H. Miller, "On finding transition states," *The Journal of Chemical Physics*, vol. 75, pp. 2800–2806, sep 1981.

[114] J. M. Bofill, "Updated Hessian matrix and the restricted step method for locating transition structures," *Journal of Computational Chemistry*, vol. 15, pp. 1–11, jan 1994.

[115] Á. Ruiz-Serrano and C.-K. Skylaris, "A variational method for density functional theory calculations on metallic systems with thousands of atoms," *The Journal of Chemical Physics*, vol. 139, p. 054107, aug 2013.

[116] I. M. Billas, A. Châtelain, and W. A. de Heer, "Magnetism from the atom to the bulk in iron, cobalt, and nickel clusters.," *Science (New York, N.Y.)*, vol. 265, pp. 1682–4, sep 1994.

[117] D. Sanchez-Portal, E. Artacho, and J. M. Soler, "Projection of plane-wave calculations into atomic orbitals," *Solid State Communications*, vol. 95, pp. 685–690, sep 1995.

[118] J. Aarons and C.-K. Skylaris, "Electronic annealing Fermi operator expansion for DFT calculations on metallic systems," *The Journal of Chemical Physics*, vol. 148, p. 074107, feb 2018.

[119] L. E. Ratcliff, S. Mohr, G. Huhs, T. Deutsch, M. Masella, and L. Genovese, "Challenges in large scale quantum mechanical calculations," *Wiley Interdisciplinary Reviews: Computational Molecular Science*, vol. 7, p. e1290, jan 2017.

[120] A. Hjorth Larsen, J. Jørgen Mortensen, J. Blomqvist, I. E. Castelli, R. Christensen, M. Dułak, J. Friis, M. N. Groves, B. Hammer, C. Hargus, E. D. Hermes, P. C. Jennings, P. Bjerre Jensen, J. Kermode, J. R. Kitchin, E. Leonhard Kolsbjerg, J. Kubal, K. Kaasbjerg, S. Lysgaard, J. Bergmann Maronsson, T. Maxson, T. Olsen, L. Pastewka, A. Peterson, C. Rostgaard, J. Schiøtz, O. Schütt, M. Strange, K. S. Thygesen, T. Vegge, L. Vilhelmsen, M. Walter, Z. Zeng, and K. W. Jacobsen, "The atomic simulation environment—a Python library for working with atoms," *Journal of Physics: Condensed Matter*, vol. 29, p. 273002, jul 2017.

[121] J. Enkovaara, C. Rostgaard, J. J. Mortensen, J. Chen, M. Dułak, L. Ferrighi, J. Gavnholt, C. Glinsvad, V. Haikola, H. A. Hansen, H. H. Kristoffersen, M. Kuisma, A. H. Larsen, L. Lehtovaara, M. Ljungberg, O. Lopez-Acevedo, P. G. Moses, J. Ojanen, T. Olsen, V. Petzold, N. A. Romero, J. Stausholm-Møller, M. Strange, G. A. Tritsaris, M. Vanin, M. Walter, B. Hammer, H. Häkkinen, G. K. H. Madsen, R. M. Nieminen, J. K. Nørskov, M. Puska, T. T. Rantala, J. Schiøtz, K. S. Thygesen, and K. W. Jacobsen, "Electronic structure calculations with GPAW: a real-space implementation of the projector augmented-wave method," *Journal of Physics: Condensed Matter*, vol. 22, p. 253202, jun 2010.

[122] D. S. Wishart, Y. D. Feunang, A. C. Guo, E. J. Lo, A. Marcu, J. R. Grant, T. Sajed, D. Johnson, C. Li, Z. Sayeeda, N. Assempour, I. Iynkkaran, Y. Liu, A. Maciejewski, N. Gale, A. Wilson, L. Chin, R. Cummings, D. Le, A. Pon, C. Knox, and M. Wilson, "DrugBank 5.0: a major update to the DrugBank database for 2018," *Nucleic Acids Research*, vol. 46, pp. D1074–D1082, jan 2018.

[123] F. A. Voter, "Hyperdynamics: Accelerated molecular dynamics of infrequent events," *Chemical Engineering Journal*, vol. 78, no. 20, pp. 77–83, 1997.

[124] D. Packwood, J. Kermode, L. Mones, N. Bernstein, J. Woolley, N. Gould, C. Ortner, and G. Csányi, "A universal preconditioner for simulating condensed phase materials," *The Journal of Chemical Physics*, vol. 144, p. 164109, apr 2016.

[125] S. Makri, C. Ortner, and J. R. Kermode, "A preconditioning scheme for minimum energy path finding methods," *The Journal of Chemical Physics*, vol. 150, p. 094109, mar 2019.

[126] T. Morita, "Solution of the Bloch Equation for Many-Particle Systems in Terms of the Path Integral," *J. Phys. Soc. Jpn.*, 2013.

[127] E. L. Kolsbjerg, M. N. Groves, and B. Hammer, "An automated nudged elastic band method," *The Journal of Chemical Physics*, vol. 145, p. 094107, sep 2016.

[128] K. K. B. Duff, L. Spanu, and N. D. M. Hine, "Impact of Carbonyl Formation on Cobalt Ripening over Titania Surface," *J. Phys. Chem. C*, vol. 121, pp. 15880–15887, 7 2017.

[129] J. P. Perdew, K. Burke, M. Ernzerhof, D. of Physics, and N. O. L. . J. Quantum Theory Group Tulane University, "Generalized Gradient Approximation Made Simple," *Physical Review Letters*, vol. 77, no. 18, pp. 3865–3868, 1996.

[130] J. P. Perdew, K. Burke, and M. Ernzerhof, "Errata: Generalized Gradient Approximation Made Simple," *Physical Review Letters*, vol. 78, no. 7, p. 1396, 1997.

[131] G. Henkelman, B. P. Uberuaga, and H. Jónsson, "Climbing image nudged elastic band method for finding saddle points and minimum energy paths," *Journal of Chemical Physics*, vol. 113, no. 22, pp. 9901–9904, 2000.

[132] A. Vittadini, A. Selloni, F. P. Rotzinger, and M. Grätzel, "Structure and Energetics of Water Adsorbed at TiO2 Anatase (101) and (001) Surfaces," *Physical Review Letters*, vol. 81, no. 14, pp. 2954–2957, 1998.

[133] F. Jollet, M. Torrent, and N. Holzwarth, "Generation of Projector Augmented-Wave atomic data: A 71 element validated table in the XML format," *Computer Physics Communications*, vol. 185, pp. 1246–1254, apr 2014.

[134] A. Tuxen, S. Carenco, M. Chintapalli, C.-H. Chuang, C. Escudero, E. Pach, P. Jiang, F. Borondics, B. Beberwyck, A. P. Alivisatos, G. Thornton, W.-F. Pong, J. Guo, R. Perez, F. Besenbacher, and M. Salmeron, "Size-Dependent Dissociation of Carbon Monoxide on Cobalt Nanoparticles," *J. Am. Chem. Soc.*, vol. 135, pp. 2273–2278, feb 2013.

[135] P. J. Feibelman, B. Hammer, J. K. Nørskov, F. Wagner, M. Scheffler, R. Stumpf, R. Watwe, and J. Dumesic, "The CO/Pt(111) Puzzle," *J. Phys. Chem. B*, vol. 105, no. 18, pp. 4018–4025, 2001.

[136] S. Luo, Y. Zhao, and D. G. Truhlar, "Improved CO Adsorption Energies, Site Preferences, and Surface Formation Energies from a Meta-Generalized Gradient Approximation Exchange–Correlation Functional, M06-L," *The Journal of Physical Chemistry B*, vol. 105, pp. 2975–2979, oct 2001.

[137] Y. Zhao and D. G. Truhlar, "A new local density functional for main-group thermochemistry, transition metal bonding, thermochemical kinetics, and noncovalent interactions," *The Journal of Chemical Physics*, vol. 125, p. 194101, nov 2006.

[138] J. P. Perdew, A. Ruzsinszky, G. I. Csonka, L. A. Constantin, and J. Sun, "Workhorse Semilocal Density Functional for Condensed Matter Physics and Quantum Chemistry," *Physical Review Letters*, vol. 103, p. 026403, jul 2009.

[139] B. Hammer, L. B. Hansen, and J. K. Nørskov, "Improved adsorption energetics within density-functional theory using revised Perdew-Burke-Ernzerhof functionals," *Physical Review B*, vol. 59, pp. 7413–7421, mar 1999.

[140] F. R. Manby, M. Stella, J. D. Goodpaster, and T. F. Miller, "A Simple, Exact Density-Functional-Theory Embedding Scheme," *Journal of Chemical Theory and Computation*, vol. 8, pp. 2564–2568, aug 2012.

[141] E. A. Owen and D. M. Jones, "Effect of Grain Size on the Crystal Structure of Cobalt," *Proceedings of the Physical Society. Section B*, vol. 67, pp. 456–466, jun 1954.

[142] J. Aarons, M. Sarwar, D. Thompsett, and C.-K. Skylaris, "Perspective: Methods for large-scale density functional calculations on metallic systems," vol. 145, dec 2016.

[143] A. S. P. Gomes and C. R. Jacob, "Quantum-chemical embedding methods for treating local electronic excitations in complex chemical systems," *Annual Reports Section "C" (Physical Chemistry)*, vol. 108, p. 222, may 2012.

Appendix A

Geometry Information for Carbonyl Species Adsorbed to Anatase (101)

A.1 Geometry Information

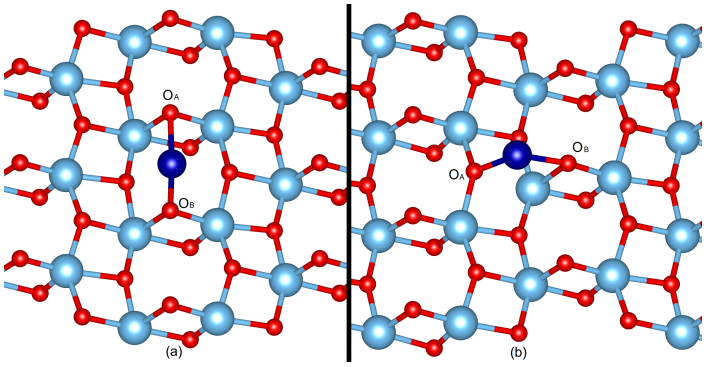

Fig. A.1 Adsorption configurations of cobalt at sites A and B on the anatase (101) surface. Oxygens have been labeled as the $O_A - Co - O_B$ angle is recorded in Tables A.1 and A.2.

	Site A				Site B			
Species	Length	c.n.	Δz	Angle	Length	c.n.	Δz	Angle
Co	–	4	0.00	170	–	2	0.00	125
CoO	1.87	3	0.61	123	1.63	2	0.50	91
CoOH	1.93	3	0.58	126	1.88	2	0.122	107
CoCO	1.76	3	0.69	119	1.76	2	0.25	103
$Co(CO)_2$	1.80	2	1.14	115	1.72	2	0.46	91
$Co(CO)_3$	1.79	1	1.88	–	1.79	1	1.22	–

Table A.1 Geometry information for each adsorbate on the dry surface. The geometry information contains the bond length in Å between Co and its bound group (or the average where appropriate), the coordination number of Co with the surface oxygen atoms, the distance out of the surface plane the Co atom is relative to the Co adsorption site Δz in Å, and the Co-surface angle as defined in Figure A.1.

	Site A				Site B			
Species	Length	c.n.	Δz	Angle	Length	c.n.	Δz	Angle
Co	–	4	0.00	168	–	2	0.00	108
CoO	1.94	3	0.72	122	1.77	1	0.84	–
CoOH	2.06	4	0.23	171	2.10	3	-0.15	101
CoCO	1.74	3	0.78	134	1.75	2	0.40	92
$Co(CO)_2$	1.76	2	1.49	102	1.72	2	0.31	90

Table A.2 Geometry information for each adsorbate on the 1ML hydrated surface. The geometry information contains the bond length in Å between Co and its bound group (or the average where appropriate), the coordination number of Co with the surface oxygen atoms, and the Co-surface angle as defined in Figure A.1.

Appendix B

Bader Charges of Cobalt in Species Adsorbed to Anatase (101)

B.1 Bader Charges

DFT calculation on of bulk rock-salt CoO, which contains Co in the +2 oxidation state, resulted in a Bader charge on the Co atoms of 7.70 e, compared to the 9 e expected for an isolated Cobalt atom. This can be compared to the Bader charges of the adsorbed cobalt atoms in each adsorbate in Table B.1 to see that the cobalt atom exists largely in the +2 state on the surface with some reduction, usually when under-coordinated. The direct comparison of Bader charges is less applicable when the Co is coordinated to carbon atoms due to Co−C bonds having a different characteristic partial ionicity to Co−O bonds (C has a different electronegativity to O). An additional calculation of a +2 charged system with Co at site A of the dry surface showed that the Co remained in the +2 state with a Bader charge of 7.80 e.

	Dry Surface		Hydrated Surface	
System	Site A	Site B	Site A	Site B
Co	8.03	8.29	8.16	8.11
CoO	7.70	7.89	7.66	7.88
CoOH	7.71	8.04	7.87	7.88
CoCO	8.04	8.23	8.15	7.96
Co(CO)2	7.92	8.11	8.04	8.10
Co(CO)3	8.19	8.11		

Table B.1 Bader charge of the Co atom in several adsorbates on the dry and hydrated anatase (101) surfaces.